B CELL EPITOPE MAPPING OF RIVAX, A CANDIDATE RICIN VACCINE ANTIGEN

By

SIVA KRISHNA ANGALAKURTHI

Submitted to the graduate degree program in Pharmaceutical Chemistry and the Graduate Faculty of the University of Kansas in partial fulfillment of the requirements for the degree of Doctor of Philosophy.

_____

Chairperson C. Russell Middaugh, Ph.D.

_____

William Picking, Ph.D.

_____

Teruna J. Siahaan, Ph.D.

_____

Thomas Tolbert, Ph.D.

_____

Prajnaparamita Dhar, Ph.D.

Date Defended: September 18, 2018

The Dissertation Committee for SIVA KRISHNA ANGALAKURTHI

certifies that this is the approved version of the following dissertation:

B CELL EPITOPE MAPPING OF RIVAX, A CANDIDATE RICIN VACCINE ANTIGEN

_____

Chairperson Dr. C. Russell Middaugh

Date approved: September 18, 2018

Abstract

Ricin toxin's enzymatic A subunit (RTA) is a 267 amino acid RNA N-glycosidase that depurinates a conserved adenine residue of 28S rRNA, resulting in ribosome arrest and apoptosis. One of the leading subunit vaccine candidates for ricin is RiVax, a two point mutant (V76M, Y80A) of RTA. RiVax has proven to be safe in humans, however, it could not elicit a robust toxin-neutralizing antibody response. In order to redesign a potent ricin subunit vaccine candidate based on RTA, an immunological rationale has to be implemented. Protection against ricin is antibody mediated and hence generating a comprehensive B cell epitope map of ricin toxin would not only help in evaluating future ricin vaccine candidates in humans but also provides an immunological rationale for designing new vaccine candidates. Previous studies have shown that toxin neutralizing antibodies recognized four immunodominant regions on RTA i.e. four epitope clusters (namely cluster I to IV). RTA's active site is surrounded by cluster III. Surprisingly, mAb IB2, which defines cluster III is the only antibody that recognized this immunodominant region. We previously showed that IB2 binds to helices C and G on the surface of RiVax. In this study, we sought to gain a better understanding of cluster III using a collection (21) of single domain antibodies (V_HHs) that are derived from ricin immunized alpacas. To this end, I first produced and characterized RiVax (a safer version which is structurally identical to RTA) for its structural integrity since our main emphasis lies in identifying discontinuous/ conformational epitopes. Based on hydrogen exchange mass spectrometry (HX-MS) studies, V_HHS recognized overlapping epitopes with four spatially distinct contact regions i.e. they were grouped into four subclusters (namely 3.1 to 3.4) within cluster III region. Subcluster 3.1 includes helices C and G. Subcluster 3.2 encompasses additionally helix B along with helices C and G. While subcluster 3.3 consists of

helices B and G, subcluster 3.4 includes helices C, E and strand h. Of the 21 antibodies that we analyzed, only two, namely V1D3 and V6D4 have shown toxin neutralizing activity (TNA). Both neutralizing antibodies have strong binding affinity (sub nanomolar range) to the toxin and engaged a common secondary structural element, namely helix G as part of their epitope.

The second part of my dissertation focusses on fibroblast growth factor-1 (FGF-1), a member of β-trefoil family of proteins. FGFs regulate a number of developmental process including mitogenesis, angiogenesis and homeostasis etc. Due to their wide range of biological activities, FGFs has been of interest in several clinical applications. In particular, wound healing has generated considerable interest. Studies have shown that several polyanions (sulfated and phosphorylated) have increased the thermal stability of FGF-1 by 15-30^{o}C. In this study, we sought to identify the binding sites of the polyanions. In particular, we studied two sulfated (heparin, low MW heparin) and two phosphorylated (phytic acid and ATP) polyanions. Using HX-MS, we examined the local dynamics as well as binding sites of the polyanions. For local dynamics, we identified strand 4 and 5 and the turn connecting them to be most flexible which agrees with previous NMR studies. On the other hand, strands 8, 9 and 10 appear to be more rigid which is consistent with crystallographic B factors as well as local dynamic studies conducted by NMR. Crystal studies have shown that heparin binds to N-terminal Asn18 and to C-terminal Lys105, Tryp107, Lys112, Lys113, Arg119, Pro121, Arg122, Gln127 and Lys128 indicating electrostatic forces as the dominant interactions. Heparin binding as determined by HX-MS is consistent with the crystallography data. We find other polyanions tested bind in a similar manner to heparin, primarily targeting the turns in the lysine rich C-terminal region of FGF-1 along with two distinct N-terminal regions that contains lysines and arginines/ histidines. This confirms the interactions between FGF-1 and polyanions are primary directed by electrostatics.

Dedicated to my parents, Nagamani and Narasimham, and my sister HimaBindu

Acknowledgements

First and foremost I would like to express my utmost gratitude to Dr. Russ Middaugh for believing in me and giving me the opportunity to work in his laboratory. It has been quite an honor and experience being a member of your lab. Your wisdom and enthusiasm to teach and share your knowledge of science has helped me grow to the educated scientist I am today. I will forever appreciate your unconditional support when I actually needed help. I would also like to thank Drs. David Volkin and David Weis for their scientific guidance and suggestions during my research. I truly appreciate all of their inputs and help provided over the years. My sincere thanks to Drs. Nick Mantis and David Vance without whom this work would not have been possible.

I would like to thank Dr. Sangeeta Joshi for her scientific guidance in the early stages of my work as well as her friendship throughout the years. To the Middaugh and Volkin lab past and present, each and every one of you has helped me reach this point in my career. In particular, I would like to thank Ron Toth, Ph.D. who trained me in conducting mass spectrometry experiments. I would also like to acknowledge Dr. Weis's lab members, in particular, Tyler Hageman and Dr. Farai Rusinga for playing a major role in increasing my understanding of mass spectrometry.

I would like to thank our collaborators including Nick Mantis, Ph.D.; David Vance, Ph.D.; Michael Rudolph, Ph.D.; John karanicolas, Ph.D.; Charles Shoemaker, Ph.D. and Greta Van Slyke for sharing their vast knowledge of ricin during monthly teleconferences throughout the years.

I would like to thank my committee members: Drs. Bill Picking, Teruna Siahaan, Thomas Tolbert and Prajnaparamita Dhar for taking their time to serve on my dissertation defense committee.

Finally, I would like to thank my family. To my mom and sister: There are no words to express my thankfulness about your roles in shaping up my life. You always believed in me more than anyone else. Dad, I am so grateful to you for being a good friend as well as for reminding me constantly that life isn't meant to be so serious. Last, but not least, I would like to thank my friends who I made at KU, in particular, Sahishna Phaniraj and Rupesh Bommana. Sahishna, you have been an amazing friend to me and I will always cherish our long drives with Prajwal and Swathi. Rupesh, thanks so much for being a good friend and a wonderful guide.

Table of Contents

CHAPTER 1: INTRODUCTION

Ricin: Recent incidents in the United States and abroad have increased concerns about the use of ricin toxin as a bioterrorism agent. Ricin is a member of the type II ribosome-inactivating protein (RIP) family of toxins found in plant and microbes. Ricin is found in the seeds of the castor oil plant, *Ricinus communis* which is ubiquitous in tropical environments. In its mature form, ricin is a 64 kDa glycoprotein composed of a 32 kDa enzymatic ricin A (RTA) subunit which is joined by a disulfide bond to a 32 kDa ricin B (RTB) subunit (1-4). RTA, which is 267 amino acids in length is an RNA N-glycosidase that inactivates eukaryotic ribosomes by selectively cleaving the conserved adenine residue (A_{2662}) within the sarcin-ricin loop (5-7). RTA's catalytic activity is essentially performed by five residues: Tyr80, Tyr123, Arg180, Glu177 and Trp211 (8, 9). Ricin is internalized into cells through its binding subunit RTB which binds to α (1-3)-linked galactose and N-actetylgalactosamine residues on the surface of almost all cell types (10-12). Once attached, ricin is internalized into endosomes by mechanisms that are clatherin-dependent and independent and then into the trans-Golgi network (TGN) by a process known as retrograde transport and eventually into the endoplasmic reticulum. In the endoplasmic reticulum, the two subunits of ricin, RTA and RTB, that are joined by disulfide bond separate in the presence of protein disulfide isomerase and endoplasmic reticulum degradation- enhancing α-mannosidase I-like protein 1(13-15). RTA is then transported across the endoplasmic reticulum membrane and into the cytoplasm, a process known as retro-translocation, where RTA refolding is facilitated by cytoplasmic chaperons and possibly by ribosomes as well (16-19). The refolded RTA in the cytoplasm then cleaves the N- glycosidic bond of a conserved adenosine residue within the sarcin-ricin loop of 28S RNA leading to an immediate arrest in ribosome progression and inhibition in translation (6, 20). Damaging ribosomal RNA activates the ribotoxic stress response involving stress-activated

protein kinases, leading to production of pro-inflammatory cytokines and eventually apoptosis mediated cell death (21, 22).

Structure of ricin: Ricin holotoxin is composed of two subunits RTA and RTB joined by a disulfide bond. RTA is 267 amino acids in length and is structurally divided into three distinct folding domains (2, 3). Folding domain I (1-117) is dominated by a six stranded β-sheet that terminates in a solvent exposed loop-helix-loop (23). The solvent exposed α-helix, known as helix B is conserved among all other structurally similar ribosome inactivating proteins and is a target of three toxin neutralizing murine monoclonal antibodies including PB10, R70 and 6C2 (23-27). Previous studies suggested that the loop-helix-loop motif may influence the orientation of the glutamic acid 177 (E177) side chain, which is critical for RTA's catalytic activity i.e. depurination (24). Folding domain II (118-210) is dominated by five α-helices (C-G). Helix E which runs through the center of RTA terminates with two residues (E177 and R180) that are involved in its catalytic activity. An arginine rich sequence spanning from residues 187-198 (EMRTRIRYNRRS) forms a positively charged patch and is speculated to be responsible for RTA's initial contact with rRNA (3). Folding domain III (211-267) forms a protruding element that slides into the cleft between RTB's two domains (2). The nature of interaction between folding domain III of RTA and RTB is hydrophobic and is further fortified by a disulfide bond between Cysteine 259 of RTA and Cysteine 20 of RTB. The C-terminus of RTA which is relatively disordered (intrinsically thermally unstable) compared to folding domain I and II may drive the unfolding of RTA and thereby facilitate translocation from the endoplasmic reticulum into the cytosol. RTA's enzymatic activity involves five residues that include Tyr80, Tyr123, Glu177, Arg180 and Trp211 that are situated within or near the active site (3, 9).

Ricin's binding subunit, RTB, is 262 amino acids in length that consists of two globular domains which are involved in RTB's ability to attach to the cell surfaces (2, 12). The two domains which have similar folding topologies are further divided into three homologous sub-domains (α, β, γ). Subdomains 1α and 2γ have functional carbohydrate recognition activity. While the subdomain 1α binds Gal with low affinity, subdomain 2γ binds both Gal and GalNAc and is considered a high affinity carbohydrate recognition domain (28-30).

Ricin vaccine development: Over the past several decades, a number of candidate ricin vaccines have been explored. Ricin toxoid is capable of stimulating systemic and mucosal immunity in rodent models (31-33). Deglycosylated RTA has been tested as well in rodents (34). However, due to the residual toxicity associated with ricin toxoid as well as the deglycosylated RTA not eliciting RTA specific titers that are significant enough to protect made the development of both types of vaccines to be abandoned. The ongoing efforts are focused on the development of recombinant, attenuated and stable derivatives of RTA (35, 36). The two most promising subunit vaccines are devoid of enzymatic activity, yet retain the tertiary structure of ricin and are designated RiVax and RV*E*c. Both are non-toxic derivatives of ricin's enzymatic subunit, RTA. RiVax, a full length variant (267 amino acids) of RTA was developed by Dr. Ellen Vitetta at the University of Texas Southwestern (37). Two site specific mutations were engineered in RiVax at positions 76 (V76A) and 80 (Y80A). The mutation at the key active site residue at position 80 (Y80A) eliminates the enzymatic activity (> 1000 fold). The second mutation at position 76 eliminates RTA's induced vascular leak syndrome (37, 38). The resulting recombinant protein, RiVax is virtually identical to RTA i.e. the two mutations have minimal effect on the tertiary structure of the protein (39).

The second RTA derivative being pursued as a vaccine is RV*E*c, developed by investigators at the U.S. Army, is a truncated version of RTA that lacks the C-terminal residues,

199-267 as well as a small hydrophobic loop (residues 34-43) in the N-terminus (40-42). These deletions/ truncations are engineered to reduce the RTA's intrinsic propensity to aggregate and precipitate from solution, i.e. to enhance the stability. The crystal structure of RVEc (PDB: 3LC9) reveals the atomic structure is essentially superimposable onto RTA (43). Despite lacking folding domain 3, RVEc still assumes RTA's normal tertiary structure across folding domains 1 and 2 which is certainly integral to the success of the vaccine. A number of potent toxin- neutralizing antibodies are known to bind in a conformationally dependent manner within folding domains 1 and 2 (25).

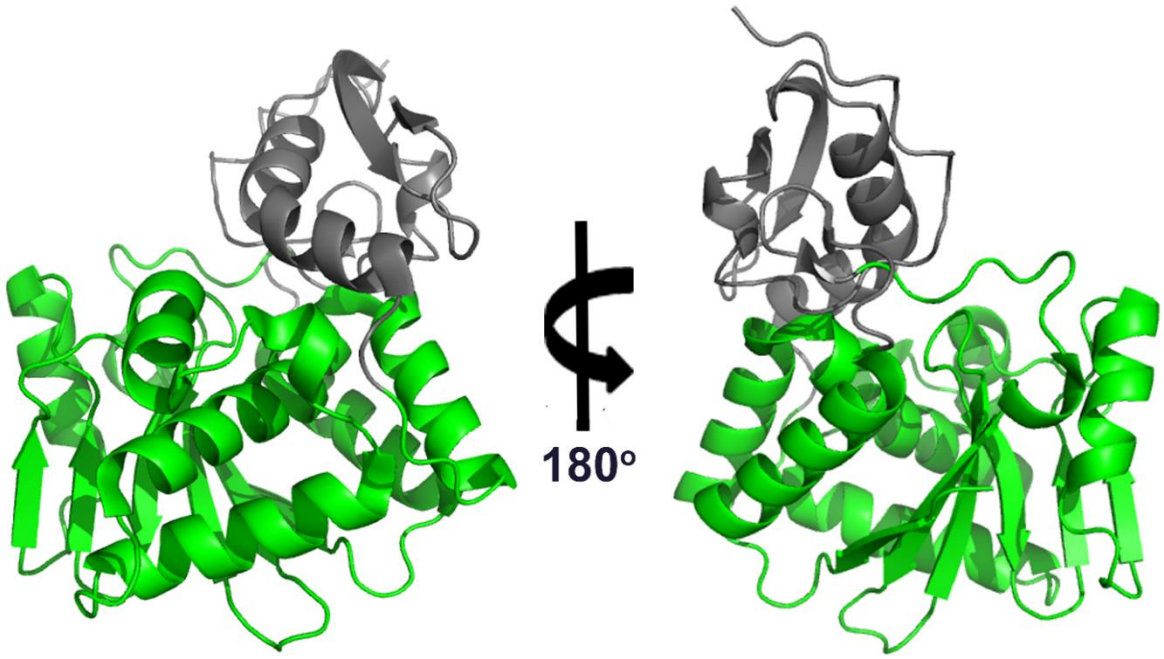

Figure 1: Ribbon diagram of RiVax (PDB: 3SRP): Gray represents the deleted regions in RVEc.

Both RiVax and RVEc have been subjected to extensive preclinical testing in mice and rabbits. RiVax, when administered to mice by the subcutaneous, intradermal and intramuscular routes has shown to elicit protective immunity against systemic and mucosal challenges (36, 37, 44-46).

RVEc, when given parenterally, protected mice and rabbits from both systemic and mucosal ricin challenge (40, 41, 47, 48). Recently, the two vaccines (RiVax and RVEc) have been compared side by side in mice (49). Both RiVax and RVEc are found to be identical although RVEc was slightly more effective than RiVax at eliciting toxin specific IgG titers and toxin neutralizing activity (TNA) when administered subcutaneously to mice.

Phase I clinical trials with RiVax and RVEc: Two pilot I clinical trials were recently completed in which RiVax and RVEc, each adsorbed to Alhydrogel, were administered to healthy individuals. Both vaccines performed similarly to each other (50, 51). Immunogenicity was based on ricin specific serum IgG levels as determined by ELISA, while toxin-neutralizing activity (TNA) was measured using mammalian cell based cytotoxicity assays. Direct comparisons between RiVax and RVEc were slightly complicated in that different methods were used to assess the endpoint titers and TNA in each case. Despite these differences there are obvious comparisons that can be made. In terms of safety, both RiVax and RVEc are similar to each other in that the vast majority (80-100%) of human volunteers reported a mild (grade I) systemic adverse events following vaccination. TNA is the indicator that is most closely associated with immunity to ricin and therefore a critical measure of vaccine efficacy. Unfortunately, neither RiVax nor RVEc were effective at eliciting TNA in human participants. In the case of RVEc, only 40-50% of the vaccinated individuals showed detectable TNA in their sera after a third vaccination. This is slightly better than the case of RiVax in that all of the vaccinated individuals produced detectable TNA, although their actual titers were very low. In summary, both vaccines were deemed to be comparatively safe and immunogenic in humans. But, neither RiVax nor RVEc proved particularly effective at eliciting toxin-neutralizing activity. While this issue could potentially be addressed with more potent adjuvant(s), the ultimate success of the ricin vaccine program requires more

established surrogate/correlate markers of protection that can be used to assess the efficacy of the vaccine on humans as reported in (52).

RiVax-induced immunity to ricin toxin challenge in non-human primates: Recent RiVax vaccination/aerosol challenge studies in rhesus macaques have provided a key step in the development of a ricin toxin subunit vaccine (53). Following aerosolized toxin challenge, the RiVax- vaccinated animals all survived while the control animals expired. This is the first study demonstrating that parenteral vaccination of non-human primates with a recombinant RTA-based subunit vaccine is sufficient to confer protective immunity to an aerosolized challenge. This type of study (vaccination/aerosolized challenge) were conducted previously in only mice, rats and rabbits (44, 45, 48). The demonstration of rhesus macaques being rendered immune to inhaled ricin toxin supports the continued development of RiVax (and/ or RVEc) for use in humans. Comparisons were made regarding the relative magnitudes of toxin specific responses between rhesus macaques and human studies that received RiVax. It should be noted that the RiVax vaccine antigen used in both the studies differ in that the human studies used a freshly prepared RiVax adsorbed to Alhydrogel while in the case of non-human primates (Rhesus macaques) a lyophilized formulation of RiVax adsorbed to Alhydrogel was used. It was seen that following RiVax vaccination in Rhesus macaques, they had peak toxic- specific serum IgG levels that were 10 times greater than those observed in human volunteers. At the time of challenge, however, toxin specific serum IgG levels declined to just 2-3 times over the levels achieved in humans that received three vaccinations with RiVax. In monkeys, TNA was reported as endpoint titers, while in human samples they were reported as µg/ mL and hence it is not possible to directly compare the two species in terms of toxin-neutralizing antibodies. This implies that there is a need to establish

standardized and universally accepted assays so that critical parameters like toxin neutralization can be compared across different clinical trials and species.

Challenges in ricin toxin vaccine development: Despite its initial success, RiVax and /or RVEc developmental progress has been hindered by additional challenges including stability, adjuvanticity and assessing RiVax and RVEc's efficacy in humans in the absence of challenge studies in humans, especially considering the fact that the exact correlates of immunity to ricin are poorly understood.

RiVax is relatively unstable in solution and has a tendency to unfold and aggregate. This would limit the shelf life of a candidate ricin vaccine (40, 41). RiVax's stability issue has been addressed by both liquid formulation and lyophilization technology where RiVax adsorbed to alum in histidine and ammonium acetate buffers were lyophilized with trehalose as a stabilizing excipient (54). In the case of RVEc, the issue of stability is addressed by deleting the relatively disordered C-terminal region and loops involved in unfolding (41) as well as by a rational engineering of disulfide bonds (55).

Phase I clinical trials have shown that both RiVax and RVEc that are adsorbed to aluminum hydroxide didn't produce robust responses in humans. The serum IgG titers were slow to peak and even after a prime and two boosts, toxin neutralizing antibodies are barely detectable or just above the baseline (50, 51). Hence, there is a need to develop different next generation adjuvants and investigate their effects on RiVax and RVEc.

One of the main obstacles to developing a ricin toxin subunit vaccine is evaluating or assessing RiVax's or RVEc's efficacy in humans in the absence of human challenge studies (which are obviously unethical) especially when the exact correlates of immunity to ricin are poorly

understood. Studies in mice have shown that toxin neutralizing antibodies are important in protection against systemic and mucosal ricin exposure. There has been many reports in the literature towards this end demonstrating that passive administration of a toxin neutralizing monoclonal antibody (mAb), Fab fragments or polyclonal antibody (pAb) mixture is sufficient to render mice impervious to a lethal dose of ricin administered by inhalation, ingestion or injection (56-61). While on the other hand, studies have also shown that toxin–specific serum IgG levels, at least in mice, are not good indicators of immunity. It was reported that mice with similar endpoint titers experience different fates upon ricin challenge: some survive while others succumb to death only marginally better than unvaccinated control animals implying that the quality rather than quantity of the antibodies is the important factor in determining protection. At present, *In vitro* neutralizing activity using mammalian cell-based cytotoxicity assays has been the sole measure of the "quality" of an anti-ricin antibody response. Over the past few years of RiVax and RVEc studies in mice, it was found that animals with detectable serum toxin neutralizing activity have survived a lethal dose ricin challenge (49, 62, 63). Hence, toxin neutralizing activity can be considered an absolute correlate of protection. However, TNA itself may be too strict a threshold by which to judge protection since it has been reported in mice that even in the absence of detectable TNA, survival was achieved following a lethal dose ricin challenge (49, 62, 63). One of the studies conducted by O'Hara and colleagues have shown all mice that are vaccinated (RiVax and RVEc adsorbed on alhydrogel) survive 10xLD50 ricin toxin challenge even though none of them had any detectable TNA in their sera. It was speculated that the circulating toxin-neutralizing antibody levels are below the limit of detection of the cell- based assays that are used (26). Another possibility is that a polyclonal mixture of non–neutralizing antibodies (as determined using *in vitro* assays) may have the ability to inactivate ricin *in vivo* through some mechanism that have not been

identified yet. Indeed, little is known about the exact mechanisms by which ricin is neutralized in vivo.

Epitope specific serum antibody profiling in assessing vaccine efficacy

Immune signature analysis or serum antibody profiling is an emerging application in vaccinology and could be well suited for use by the ricin toxin vaccine community (64, 65). Our collaborators have shown that in the case of ricin, toxin-neutralizing antibodies constitute only a minor portion (10%) of the antibody response elicited by RiVax and RVEc. It was also reported that neutralizing antibodies recognize a very limited number of critical/hot spots on the surface of RTA (25, 26). These hot spots are referred to as epitope clusters I-IV.

An epitope is the part of the antigen/toxin to which an antibody binds. An antibody can recognize either linear or conformational epitopes on the surface of an antigen/toxin. Linear epitopes consist of small stretches of contiguous amino acids within the primary structure of a protein antigen. Linear epitopes can be identified using peptide based approaches like peptide array analysis. On the other hand, conformational epitopes consist of amino acids that are apart from one another in the primary structure although, they are brought near one another in folded state of the protein antigen. Conformational epitopes can be identified by X-ray crystallography, nuclear magnetic resonance (NMR) or hydrogen deuterium exchange mass spectrometry (HX-MS).

Two potent ricin-neutralizing murine mAbs, UNIVAX 70 and PB10, target the cluster I region on RTA. UNIVAX 70 was identified by Lemley and colleagues (66), while, PB10 was reported by O'Hara and colleagues (26). Using peptide array analysis, both mAbs have been shown to recognize a "linear epitope" in helix B (residues 97-107) of RTA. Recently, Zhu and colleagues have solved the crystal structure of a toxin-antibody complex which enabled atomic level

resolution of epitopes in cluster I (67). The Fab Fragment of 6C2 (a PB10-like mAb) was co-crystallized with RTA which revealed antibody primarily in contact with helix B (residues 97-107). The other three epitope clusters (II-IV) were defined by mAbs SyH7, IB2 and GD12 (25, 26). Cluster II is defined by SyH7 which recognizes a conformational epitope in helix F (residues 187-198). IB2, defines cluster III and recognizes helix C (residues 123-130) and cluster IV by GD12 which recognizes a linear epitope in helix E (residues 163-174).

To assess the utility of immune profiling analysis for a ricin vaccine, sera from Phase I clinical trial volunteers and RiVax vaccinated macaques were subjected to direct competition ELISA with toxin neutralizing murine mAbs directed against cluster I (PB10, UNIVAX 70) and cluster II (SyH7). It was reasoned by our collaborators that the degree to which an antiserum reduced binding of cluster I and II specific mAbs would serve as indirect indicator of epitope utilization. Towards this end, they observed the antisera from both RiVax vaccinated humans and macaques reduced binding of cluster I and II specific mAbs ranging from 10-80% depending on the specific mAb. It was found both monkeys and humans have similar inhibitory profiles which suggests that the antibody response is conserved between the species. This data suggests the possibility that serum antibody profiling can be useful in assessing vaccine efficacy. The inter relationship, however, between mAb competition, toxin-neutralizing activity and protection has yet to be made.

Comprehensive B-cell epitope mapping: It was initially reported that RTA has four immune dominant regions which are referred to as epitope clusters I-IV. However, these conclusions are based on mAbs that recognize linear epitopes. O'Hara et al. reported that most of the toxin neutralizing mAbs bind RTA in a conformationally dependent manner i.e. they recognize conformational epitopes. Recently, we have reported epitopes of nine toxin- neutralizing mAbs and one non-neutralizing mAb on RTA* (two point mutated version of RTA) using HX-MS (68).

These antibodies were categorized into clusters I-IV based on contacts with RTA secondary structural elements. All antibodies except GD12 have recognized primarily the same secondary structural elements as is seen in peptide array analysis. Epitope analysis of GD12 using hydrogen deuterium exchange mass spectrometry contradicts GD12 epitope determined by peptide array analysis in which it recognized strands b and c and the two interconnecting β-turns. By all accounts, Clusters I–IV represent the most immunodominant regions on the surface of RTA. To investigate these clusters in more detail, our collaborators have screened a large library of single domain camelid antibodies (V_HHs) from RiVax and ricin toxoid vaccinated alpacas (69).

V_HH: In certain mammals belonging to the *camelidae* family (camels, Ilamas, and alpacas) as well as cartilaginous fishes, along with conventional antibodies in their sera, they possess about 45-75% of heavy chain only antibodies (70). Heavy chain antibodies are homodimers of disulfide linked heavy chains and are completely devoid of light chains. These antibodies are fully capable of antigen binding i.e. the antigen binding site of heavy chain antibodies is formed by only three complementary determining regions (CDRs) compared to the usual six CDRs which include three each from heavy and light chain in conventional antibodies. Of the three CDRs in the heavy chain antibodies, CDR3 which usually plays the dominate role in antigen binding is a long finger- like poly peptide loop. Hence, the antigen binding site of heavy chain antibodies forms a convex protruding shape and differs from that of the antigen binding site of conventional antibodies which form a concave shape (groove like). This convex shaped antigen binding site creates heavy chain antibodies which recognize cryptic (buried in the cleft) epitopes on protein surfaces as reported in (71). The fact that just an N–terminal single domain (variable domain, VH) that contains the three CDRs retains their functional activity makes them attractive for use as a second generation of therapeutic agents and immunoreagents. This single domain antibody which represents just a

variable domain is termed a V_HH rather than VH as in conventional antibodies. The insertion of another H in V_HH is to just distinguish them as having originated from a heavy chain antibody rather than from a conventional antibody. V_HHs, which are of 15 kDa and non-glycosylated are reported to be well expressed in *E. coli* (72). The unique characteristics of V_HHs such as low molecular weight, good water solubility (73), high physical-chemical stability (74), ability to fold after heating to attain their original native structure (75, 76) and the ability to bind buried epitopes on an antigen that are inaccessible to conventional antibodies (71) can potentially make them a substitute for conventional therapeutic drugs in the treatment of serious human diseases. They could also be broadly used in diagnostics.

Earlier, cluster I was interrogated in more detail using alpaca derived V_HHs based on competition ELISAs with PB10 (the cluster I defining mAb) as well as solving V_HH-RTA crystal structures (69, 77, 78). To date, seven crystal structures of cluster I V_HHs in complex with RTA were solved (78, 79). These seven V_HHs differ in the degree to which they make contact with helices B (residues 97-107), D (residues 150-157) and strand h (residues 113-117). Previously, cluster II was studied using four murine mAbs that includes SyH7, PA1, TB12 and PH12 where it was identified that cluster II possess two subclusters based on the binding sites of the four mAbs (68). Alpaca derived V_HHs were also used to study cluster II (77). Recently, we tried to further our understanding of cluster II by studying additional cluster II specific murine mAbs (Greta van slyke et.al. 2018, manuscript submitted).

The first part of my dissertation focuses on interrogating cluster III with RTA specific V_HHs. It should be noted that due to safety issues, we worked on RTA^* rather than the toxic version of RTA. RTA^* is a two point mutated (V76M, Y80A) version of RTA that eliminates the enzymatic activity. Both, RTA and RTA^* are essentially structurally identical and hence the safer version,

RTA*, was used to map structural epitopes. More emphasis is placed on conformational epitopes since most of the ricin specific antibodies bind to RTA in a conformationally dependent manner i.e. they have conformational epitopes. A variety of methods are commonly used to map the fine details of interaction between antigen and an antibody. X-ray crystallography is by far the best in that it provides detail at the level of individual amino acids and atoms. The feasibility of performing crystal studies has increased over the years with automation, miniaturization and high through put processes. Our collaborators were successful in solving the co-crystals of RTA with V_HHs (78, 79). However, it still requires a high level of sophistication and is particularly challenging to crystallize an antigen with its cognate monoclonal antibody. Nuclear magnetic resonance spectroscopy (NMR) also offers individual amino acid level resolution similar to crystallography but the technical hurdles are even higher when the size of the protein of interest increases above a certain limit (typically 30kDa) (80). Peptide based approaches coupled with ELISA-based approaches can be used to map information over a peptide region i.e. linear epitopes can be identified. However, this method is of limited use in identifying conformational epitopes. Hydrogen-deuterium exchange coupled with mass spectrometry can be used to identify both linear and conformational epitopes albeit at a peptide level resolution. In this dissertation, we have chosen HX-MS as a method of choice to identify epitopes on RTA* based on its recent success in a wide variety of pathogens (81-84).

HX-MS:

Hydrogen/ deuterium exchange (HX) was first described by Hvidt and Linderstorm-Lang in 1954 (85). Initially, HX has been detected using various spectroscopic techniques including FTIR, NMR as well as size exclusion chromatography using tritium to study protein structure and dynamics (86, 87). The coupling of mass spectrometry (MS) to study HX was first described in 1991 (88). Further improvements in HX-MS was accomplished by pairing the experiment with proteolytic digestion (89). This enabled the study of structural changes to be resolved at the peptide level (typically 5-10 amino acids). HX is sensitive to changes in protein conformation and has gained popularity within the bio-pharmaceutical industry (90-92).

When a protein is in solution, certain hydrogens are in continuous exchange with the hydrogens in solution. If an aqueous solvent is replaced with deuterated or (heavy) water (D_2O), then one can follow this exchange process. The exchange of hydrogen (more accurately protium, ^1H) with deuterium (^2H) induces an increase in 1 Da which permits one to track HX events using MS. In proteins, three types of hydrogens are present. i) hydrogens that are bonded to carbon. ii) hydrogens that are bonded to side chain atoms iii) and hydrogens that are bonded to backbone amide nitrogen. Hydrogens bonded to carbon barely exchange. While, the hydrogens that are bonded to side chain sites (O-H, N-H, and S-H) undergo exchange, however, the rate of exchange is very fast such that any deuterium incorporated will undergo rapid back exchange during LC processes. Most importantly, the hydrogens that are bound to the backbone amide nitrogens exchange at intermediate rates. Using HX-MS methods one can follow back bone amide hydrogen exchange processes i.e. the backbone dynamics of the protein can be followed. Except proline, every amino acid has a backbone amide hydrogen i.e. there is a sensor at every amino acid along the length of the protein chain. There are various factors that influence the HX process in proteins, of which the

primary factors are temperature, pH, hydrogen bonding and solvent accessibility. Of the above four factors, temperature and pH can be controlled experimentally leaving the structurally related parameters of hydrogen bonding and solvent accessibility as the governing factors in deuteration. In other words, the rate and location of exchange becomes a function of hydrogen bonding and solvent accessibility. Regions that are highly dynamic and solvent exposed (like the loops that connect α-helices) exchange fast. In contrast, the regions that are rigid (less dynamic) and involved in hydrogen bonding networks or buried within the interior of a protein such as β-sheets and α-helices exchange slowly. In folded proteins, the exchange of these backbone amide hydrogens vary from seconds to days depending on their location (93, 94).

The mechanism of backbone amide HX for native proteins under continuous labelling conditions can be expressed in equation 1:

$$\text{N-H}_{\text{closed}} \underset{k\text{cl}}{\overset{k\text{op}}{\rightleftharpoons}} \text{N-H}_{\text{open}} \xrightarrow[D_2O]{k\text{ch}} \text{N-D}_{\text{open}} \underset{k\text{op}}{\overset{k\text{cl}}{\rightleftharpoons}} \text{N-D}_{\text{closed}} \qquad (1)$$

Where, *k*cl and *k*op are rate constants for opening and closing events, respectively, while *k*ch is the chemical rate constant for an amide hydrogen to deuterium (N-H to N-D) conversion. Every N-H group may exhibit a unique combination of *k*cl, *k*op and *k*ch.

The equation suggests that the exchangeable backbone sites fluctuate between closed (exchange incompetent) and open (exchange competent) sites. Breathing motion in proteins can transiently break amide hydrogen bonds in the folded state (N-H closed) which allows access to the OD^- (catalyst under physiological condition). Equation 1 is typically considered for two limiting regimes that are generally referred to as EX1 and EX2. EX1 kinetics are characterized by kch>>

kcl, implying that the backbone amide hydrogen labelling occurs once the protein unfolds (during the very first opening event) such that

$$k\text{HX} = k\text{op} \qquad (2)$$

EX1 kinetics are seen as evidence that HX proceeds *via* global or subglobal unfolding of a protein. Therefore many proteins can be induced to undergo HX by the EX1 mechanism by subjecting the proteins to denaturants (95). While it has been noted that only a few proteins exchange by the EX1 mechanism under native conditions (96) it is the EX2 mechanism that predominates in most folded proteins. EX2 is characterized by $k\text{cl} >> k\text{ch}$ leading equation 1 to the expression

$$k\text{HX} = K\text{op}k\text{ch} \qquad (3)$$

Where, $K\text{op} = (k\text{op}/k\text{cl})$ is the equilibrium constant of the opening reaction. Under EX2 conditions the possibility of HX occurring during a single opening event is small and numerous opening/closing transitions may occur before an isotope exchange event occurs in a given amide.

Most HX-MS studies use a continuous labelling strategy where the native protein is placed in D_2O solvent for a certain period of time (usually minutes to hours) such that the deuterium incorporation can be monitored as a function of exposure time. According to equation 1, continuous labelling HX primarily monitors protein structural dynamics rather than structure per se. Nevertheless, there is a strong connection between the two aspects since disordered regions are more dynamic than tightly folded structures.

HX-MS in epitope mapping: HX-MS has substantial advantages over other foot-printing methods since it can probe the entire protein amide backbone (except proline). HX-MS provides information on the conformational dynamics of a protein when exchange kinetics are monitored. The extent of exchange reflects changes in protein solvent accessibilities as well as changes in the

stability of protein secondary structures (hydrogen bonds). This unique approach has recently been used in the biopharmaceutical industry in discovery and development of therapeutic proteins including protein conformational changes upon chemical modification, protein aggregation, and protein-ligand/ protein-protein interactions in epitope mapping (84, 97-100). The concept of applying HX-MS in epitope mapping studies is based on monitoring the changes in hydrogen exchange rates in the protein backbone amide hydrogens as a result of formation of antigen-antibody complex.

HX-MS experimental design:

HX experiments are typically performed to compare two states of a protein: a protein free state and a protein bound state (protein with antibody). For the protein bound state, both pair of proteins including antigen and antibody are mixed and incubated for certain time at a 1:2 molar ratio, respectively to ensure proper formation of an antigen-antibody complex. HX is then initiated by diluting the stock protein solution (both free and bound state stock solutions) with a large excess of D2O buffer and incubated over a period of time at room temperature (25^{o}C). The labeling time window usually ranges from seconds to hours. After a predefined period of exchange, the HX is quenched using a quench solution. The quench solution is usually maintained at ~ 0^{o}C as well as at pH 2.5 where the intrinsic exchange rate is minimal. The quench solution also usually contains guanidine hydrochloride, a denaturant, so the protein is unfolded. This unfolding helps in efficient subsequent cleavage by pepsin. After quenching the samples, the deuterated samples are then passed through an immobilized pepsin column where pepsin cleaves the protein with low degree of specificity giving rise to a mixture of redundant or overlapping peptides. This is followed by LC separation of the peptides and finally MS analysis to determine the deuterium incorporation into the peptides. This approach helps in following, with sufficient spatial resolution (peptide level

resolution), changes in solvent accessibility and hydrogen bonding of the antigen due to the various perturbations caused by antibody binding. Thus, comparing the exchange kinetics in all of the overlapping peptides that span the entire antigen between two states i.e. free and bound, could provide information regarding potential epitopes. The binding regions are assigned by identifying regions of antigen that becomes protected from HX when an antibody binds to it. For example, shown below (figure 2) are representative uptake curves of RTA* (antigen) in presence of an antibody, V6B4; on the right, distinct differences in the HX rates are seen in the peptide that spans residues 206-218 while no change in deuterium uptake rate is seen in the peptide spanning residues 56-59. The slow exchange in the peptide spanning 205-217 can be attributed to an increase in protection caused by direct protein-protein interactions indicating that this region is a part of the epitope.

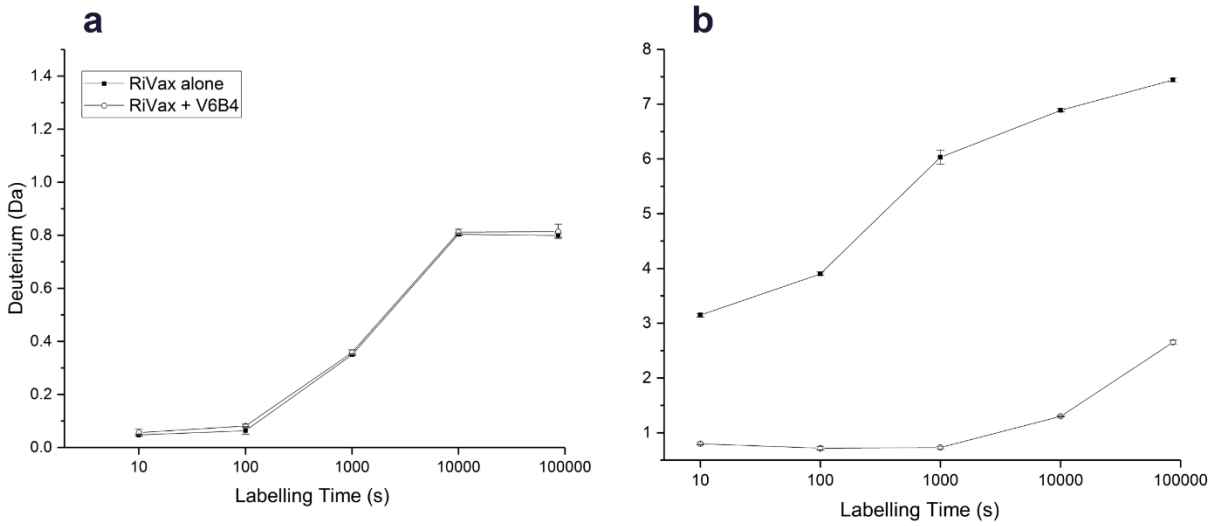

Figure 2: HX kinetics of two representative RTA* peptides in the presence of an antibody, V6B4. Panel (a) contains a peptide spanning residues 56-59, where no differences in HX rate upon V6B4

binding. Panel (b) describes the peptide spanning residues 205-217 where the rate of HX was substantially lowered.

One important consideration that impacts the sensitivity of the HX-MS methodology is the need to control the extent of back exchange. A good deal of effort has been made to minimize the loss of deuterium through back exchange by optimizing solvent pH (101), maintaining the column temperatures near 0^{o}C (102), and adding polar aprotic modifiers into the LC eluent (103). Under these optimal conditions one can minimize the extent of back exchange to less than 5%. It should be noted that obtaining an exact deuterium uptake value is not necessary in the case of epitope mapping which involves differential HX measurements since both the experiments (free and bound state) are conducted under the same conditions and at the same time.

It is quite common to use more than one method in epitope mapping. In Chapter 2 along with HX-MS we used competition ELISAs as an orthogonal method to identify the binding sites of V_HHs that are specific to RTA*. In our other papers we have used HX-MS to support crystal structures of RTA* in complex with antibodies. (Rudolph et.al; Protein engineering, Design and Selection, 2018 submitted). Recent advancements in HX-MS hardware (enabling high throughput) and software has enabled the use of HX-MS as a robust tool in charactering therapeutic proteins including epitope mapping. Several other technological developments in HX-MS can be done to further improve its performance and benefit epitope mapping experiments. For instance, coupling HX-MS with the electron-transfer dissociation (ETD) technique can help in attaining high resolution epitope mapping at a single residue level. Minimizing deuterium back exchange to negligible level could enhance the sensitivity of the method. Improved sequence coverage especially in the case of large proteins (>150 kDa) could help in characterization of potential epitopes. Nevertheless, among various orthogonal approaches, HX-MS has become one of the

most efficient methodologies for studying protein non-covalent interactions including protein-protein (epitope mapping) and protein–small molecule interactions.

Using HX-MS we have extensively conducted epitope mapping studies of RTA* using a large collection of ricin specific monoclonal antibodies and V_HHs (68, 77, 104). To date, we have mapped nearly ~70 antibodies including V_HHs and monoclonals as shown in the table below. Antibodies are classified into their respective clusters using orthogonal approaches including crystallography, competition ELISA and HX-MS.

Cluster	mAb	VHH	2º structure
I	PB10, R70, WECB2	JIV-F5*, JIV-G12* (and its variants S1,T1,F2), JIY-A7*, JIY-E3, JIY-E5*, JIY-G11*, JNM-B5, JNM-E4, JNM-F8*, JNM-G4, JPF-E8, V6F6, V7F8, V7H10, V8D5	helix B, strand h
I-II		JIY-D9, JIY-D10*, V2B8, V6A2	helix D, strand h
I-III		JNM-A11, V1B11, JPF-A9*, V6D8, V6F12, V6H6	helix C, strand h
I-III-IV		V7H7	helix B, C, G
I-IV		JNM-C12, V7D12	
II	SyH7, PA1, TB12, PH12, WECH1, LE4, CH1, SW1, 6C4	JIY-E1*, V1C7*, V1C7_G29R, V2B9, V2E8, V5C1, V5C1_R29G, V5E1*, JPD-H11, JPF-H2	helix A, C-G, strand d-e
II-III		JNM-D1	helix C, G
III	IB2	JIV-F6, V1B10, V1D3*, V1G6, V2A11*, V2G10*, V5A2, V6A6, V6A7*, V6B4 , V6C4, V6D4*, V6G10, V6G12, V6H8*, V7C8, V8C7, V8E6	helix C, G, strand i-j
IV	GD12, JD4, UN12		helix B, strand b-d

TBA		V6C2, V6H9, V6H4, V8B6, V7A3, V8D2, V9E1, V9F6	

Underline indicates the mAb &VHH epitopes that have been resolved by HDX; * indicates the VHH – RTA* structures that have been solved by X-ray crystallography; Red are strongly neutralizing antibodies.

In this dissertation, the work focusses mainly on cluster III VHHs and any other VHHs that are related to cluster III including VHHs that are classified as cluster I-III, I-III-IV and II-III.

In chapter 2, we have used HX-MS to study protein-protein interactions while in chapter 3 we used it for studying protein-small molecule interactions i.e. interaction of polyanions with fibroblast growth factor-1 (FGF-1).

FGFs: The mammalian fibroblast growth factors (FGFs) are a family of twenty three secreted proteins that interact with four signaling tyrosine kinase FGF receptors (FGFRs). These FGFs, FGF1-FGF10 and FGF16-FGF23 are grouped into six subfamilies based on differences in sequence homology and phylogeny (105). The unassigned FGFs, FGF11-FGF14, share a high sequence identity with the FGF family but do not activate FGFRs and hence are not considered actual members of the FGF family (106). FGFs are mitogenic and play a primary role in the regulation of angiogenesis. They are involved in a variety of physiological events including wound healing, organogenesis, tissue maturation, brain patterning etc. Most FGFs are specifically distinguished by their ability to bind heparin and hence are designated as heparin-binding growth factors. In fact, signal transduction requires association of FGF with FGFRs and heparin sulfate (HS) proteoglycan in a specific manner on the cell surface. FGF-1, also known as acidic fibroblast growth factor, is unique in that it activates/stimulates all FGFRs. Thus, FGF-1 is considered to be a “pan-FGFR activator” and as a result a broad specificity human mitogen (107, 108).

It is well established that HS involvement is required for FGF receptor signaling (109-111). Numerous studies have reported the crystal structures including binary complexes of FGF-heparin (112, 113), FGF-FGFR (114, 115). However, solving the crystal structure of FGF1-FGFR-HS ternary complex has provided the structural basis for the role of HS in FGF signalling (116). Crystal structure of the ternary complex revealed that one heparin (decasaccharide) molecule links two FGF-1 molecules in which each of them binds to a single receptor, thus making it a heteropentameric assembly. In other words, the complex is considered as two 1:1 FGF1-FGFR complexes associated through interaction with heparin. The role of HS is not just limited to FGF-1 signalling but also plays a key determinant in the pharmacokinetic properties of FGF-1 (117, 118). For instance, increased tissue levels of HS restrict the distribution of signalling molecules such as FGF-1, and may play a role in pattern formation in embryogenesis. On the other hand, decreased levels of HS in the vasculature aid in long range transport of such signalling molecules (119).

Crystal structure of FGF-1: FGF-1 is one of the better characterized members of the FGF family. FGF-1 adopts a β-trefoil fold, exhibiting a pseudo-three-fold (i.e. C_3) cyclic symmetry at the tertiary structure level (120-122). It is composed of three repeating trefoil-fold subdomains which are of approximately 40-50 amino acids in length. Each subdomain is composed of a pair of antiparallel β-hairpin like structure. Therefore, FGF-1 has a total of 12 β-strands (numbered# 1-12) and 11 reverse turns (numbered# 1-11) (figure 3). Turns are the principal structural elements that allow 180^o changes in the polypeptide chain direction and are responsible for adoption of a globular protein architecture. FGF-1 contains a cluster of basic residues in the last two-thirds of the third trefoil-fold subdomain forming a dense positively charged patch as shown in Figure 3. Although, the higher order (tertiary structure) symmetry of FGF-1 consists of three repeating

subdomains, the primary structure of FGF-1 is highly asymmetric i.e. only one amino acid is conserved among the three repeating subdomains. This asymmetrical sequence may reflect not only genetic drift but also explains the distribution of folding and functional regions asymmetrically distributed in the primary structure.

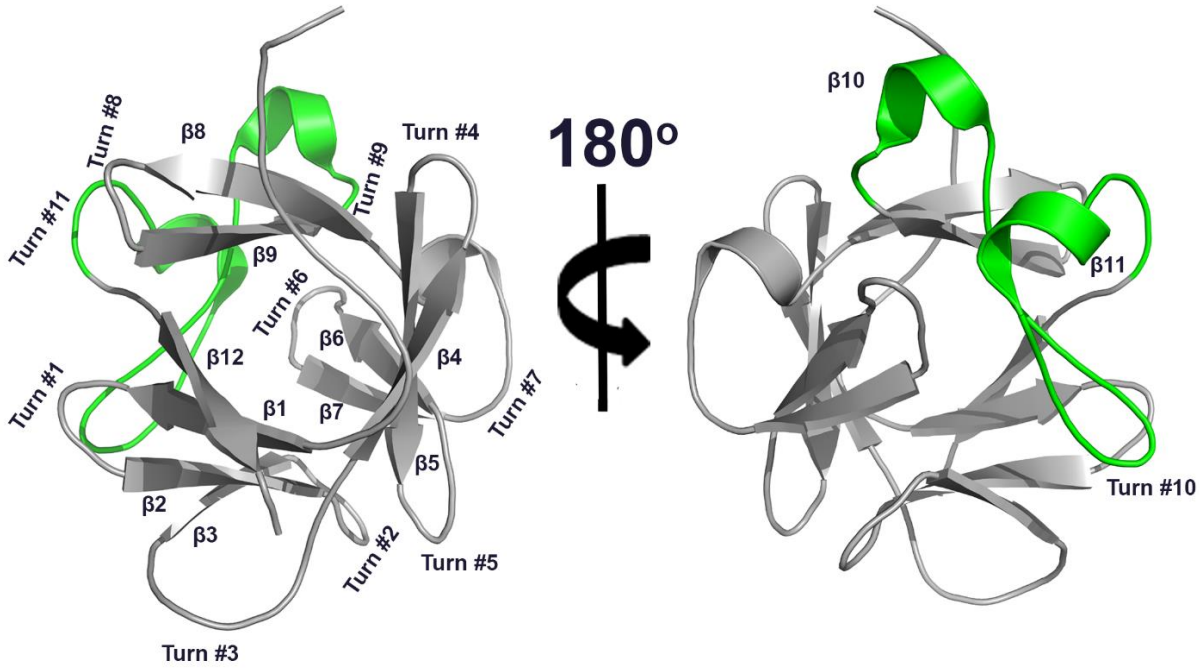

Figure 3: Left panel: Ribbon diagram of FGF-1 (PDB: 1JQZ) oriented along the C_3 (three fold) axis of rotational symmetry. β-strands (#1-12) and turns (#1-11) in the three subdomains are labelled. The C-terminus region that is rich in positively charged amino acids is shaded green. Right panel: FGF-1 is rotated 180^o to indicate the positive charge rich C-terminus subdomain.

Heparin and membrane bound heparin sulfate proteoglycan (HSPG) which consist of large negative charge density are known to bind to specific cluster of positively charged amino acids in both the C–terminus as well the N–terminus region. Numerous investigators employing a wide range of methods have identified the regions that are associated with HS binding and receptor

binding functionality in FGF-1. Several molecular structures, including seven x-ray and two NMR (PDB accession 1E0O, 1DJS, 1RY7, 2ERM, 1HKN, 1RML, 1AFC, 1EVT and 1AXM) of FGF-1 are solved in complex with receptor and/or heparin analogues and have been used to identify the structural details of the regions of FGF-1 associated with heparin and receptor binding. The above structural data has been validated using a large number of functional studies (including point mutations, deletions, chemical modifications and peptide binding competition studies) in combination with affinity chromatography, surface plasmon resonance and analytical ultracentrifugation (123-126). X-ray crystallography studies have revealed the core HS-binding region on FGF-1, in which HS interacts with amino acid residue 18 (Asn18) as well as the C-terminus region spanning residues from 112-128 of FGF-1 (116, 127).

FGF-1 stability:

While HS binding is critical for the proper biological functioning of FGF-1, addition of HS to FGF-1 also confers stability against thermal and chemical denaturation as well as proteolysis (128-130). Thus, heparin inclusion in the formulation of FGF-1 improves its potency, stability, and storage (128). Many potential clinical applications of FGFs have been suggested due to their wide range of receptor- mediated biological activities. In particular, their effect on the process of wound healing has generated significant interest (131, 132). For an efficacious formulation of FGF-1, one of the important aspects to be considered is its conformational stability against thermal unfolding since it is known that FGF-1 unfolds at physiological temperature in the absence of a stabilizing polyanion (133) . In addition to the well-known protection of FGF-1 by HS, a surprising number of polyanions, including sulfated and phosphorylated compounds, have also been shown to induce physical stability (134). Subsequently, it was found that the structural specificity of the ligand required to stabilize FGF-1 against heat induced aggregation was weak. A vast variety of

negatively charged bio-polymers (nucleic acids, phosphorylated proteins, and homopolymers of acidic amino acids), sulfated polymers (heparins, chondroitins, dextran etc.) and even smaller sulfated and phosphorylated organic molecules are also able to inhibit thermal induced aggregation of FGF-1. The common feature among these agents is the presence of at least one or more highly negative charge density regions. It was also found that the level of ligand sulfation/phosphorylation is critical for inducing FGF-1 stability. Increasing the sulfation/phosphorylation level dramatically enhances the thermal stability of FGF-1(134).

How do polyanions stabilize FGF-1? What are the binding sites of these polyanions?

The above questions have been addressed previously using crystal structures and NMR using heparin and its analogues. While crystallography is the mother of all techniques for identifying the binding sites, it cannot follow the conformational dynamics of the protein. To this end, NMR has been used and was successful in identifying the binding sites of heparin and heparin analogues. Herein, we used HX-MS to address the above two questions. We focused on four polyanions including two sulfated and two phosphorylated molecules. In particular, we have studied two sulfated molecules including heparin and low MW heparin since sulfation levels are critical for enhancing the protein's thermal stability as well as two phosphorylated molecules including phytic acid and ATP (small organic phosphorylated molecules).

Briefly, our study has revealed all the polyanions invariably have the same binding sites on FGF-1. As expected, heparin (carries high negative charge density compared to other three tested molecules) has shown strong protection i.e. stronger interaction compared to the others. Also, the entire FGF-1 has shown slow HX in the presence of all polyanions implying the conformational dynamics of FGF-1 has decreased or an increase in rigidity is induced.

REFERENCES:

1. Katzin BJ, Collins EJ, Robertus JD. Structure of ricin A-chain at 2.5 A. Proteins. 1991;10(3):251-9.
2. Montfort W, Villafranca JE, Monzingo AF, Ernst SR, Katzin B, Rutenber E, et al. The three-dimensional structure of ricin at 2.8 A. The Journal of biological chemistry. 1987;262(11):5398-403.
3. Rutenber E, Katzin BJ, Ernst S, Collins EJ, Mlsna D, Ready MP, et al. Crystallographic refinement of ricin to 2.5 A. Proteins. 1991;10(3):240-50.
4. Robertus JD, Piatak M, Ferris R, Houston LL. Crystallization of ricin A chain obtained from a cloned gene expressed in Escherichia coli. The Journal of biological chemistry. 1987;262(1):19-20.
5. Olsnes S, Fernandez-Puentes C, Carrasco L, Vazquez D. Ribosome inactivation by the toxic lectins abrin and ricin. Kinetics of the enzymic activity of the toxin A-chains. European journal of biochemistry. 1975;60(1):281-8.
6. Endo Y, Mitsui K, Motizuki M, Tsurugi K. The mechanism of action of ricin and related toxic lectins on eukaryotic ribosomes. The site and the characteristics of the modification in 28 S ribosomal RNA caused by the toxins. The Journal of biological chemistry. 1987;262(12):5908-12.
7. Endo Y, Tsurugi K. RNA N-glycosidase activity of ricin A-chain. Mechanism of action of the toxic lectin ricin on eukaryotic ribosomes. The Journal of biological chemistry. 1987;262(17):8128-30.
8. Weston SA, Tucker AD, Thatcher DR, Derbyshire DJ, Pauptit RA. X-ray structure of recombinant ricin A-chain at 1.8 A resolution. Journal of molecular biology. 1994;244(4):410-22.
9. Monzingo AF, Robertus JD. X-ray analysis of substrate analogs in the ricin A-chain active site. Journal of molecular biology. 1992;227(4):1136-45.
10. Rutenber E, Ready M, Robertus JD. Structure and evolution of ricin B chain. Nature. 1987;326(6113):624-6.
11. Swimmer C, Lehar SM, McCafferty J, Chiswell DJ, Blattler WA, Guild BC. Phage display of ricin B chain and its single binding domains: system for screening galactose-binding mutants. Proceedings of the National Academy of Sciences of the United States of America. 1992;89(9):3756-60.
12. Sphyris N, Lord JM, Wales R, Roberts LM. Mutational analysis of the Ricinus lectin B-chains. Galactose-binding ability of the 2 gamma subdomain of Ricinus communis agglutinin B-chain. The Journal of biological chemistry. 1995;270(35):20292-7.
13. Slominska-Wojewodzka M, Gregers TF, Walchli S, Sandvig K. EDEM is involved in retrotranslocation of ricin from the endoplasmic reticulum to the cytosol. Molecular biology of the cell. 2006;17(4):1664-75.
14. Spooner RA, Watson PD, Marsden CJ, Smith DC, Moore KA, Cook JP, et al. Protein disulphide-isomerase reduces ricin to its A and B chains in the endoplasmic reticulum. The Biochemical journal. 2004;383(Pt 2):285-93.
15. Sokolowska I, Walchli S, Wegrzyn G, Sandvig K, Slominska-Wojewodzka M. A single point mutation in ricin A-chain increases toxin degradation and inhibits EDEM1-dependent ER retrotranslocation. The Biochemical journal. 2011;436(2):371-85.

16. Spooner RA, Lord JM. How ricin and Shiga toxin reach the cytosol of target cells: retrotranslocation from the endoplasmic reticulum. Current topics in microbiology and immunology. 2012;357:19-40.
17. Argent RH, Parrott AM, Day PJ, Roberts LM, Stockley PG, Lord JM, et al. Ribosome-mediated folding of partially unfolded ricin A-chain. The Journal of biological chemistry. 2000;275(13):9263-9.
18. Li S, Spooner RA, Allen SC, Guise CP, Ladds G, Schnoder T, et al. Folding-competent and folding-defective forms of ricin A chain have different fates after retrotranslocation from the endoplasmic reticulum. Molecular biology of the cell. 2010;21(15):2543-54.
19. Spooner RA, Hart PJ, Cook JP, Pietroni P, Rogon C, Hohfeld J, et al. Cytosolic chaperones influence the fate of a toxin dislocated from the endoplasmic reticulum. Proceedings of the National Academy of Sciences of the United States of America. 2008;105(45):17408-13.
20. Gluck A, Endo Y, Wool IG. The ribosomal RNA identity elements for ricin and for alpha-sarcin: mutations in the putative CG pair that closes a GAGA tetraloop. Nucleic acids research. 1994;22(3):321-4.
21. Jandhyala DM, Thorpe CM, Magun B. Ricin and Shiga toxins: effects on host cell signal transduction. Current topics in microbiology and immunology. 2012;357:41-65.
22. Iordanov MS, Pribnow D, Magun JL, Dinh TH, Pearson JA, Chen SL, et al. Ribotoxic stress response: activation of the stress-activated protein kinase JNK1 by inhibitors of the peptidyl transferase reaction and by sequence-specific RNA damage to the alpha-sarcin/ricin loop in the 28S rRNA. Molecular and cellular biology. 1997;17(6):3373-81.
23. Lebeda FJ, Olson MA. Prediction of a conserved, neutralizing epitope in ribosome-inactivating proteins. International journal of biological macromolecules. 1999;24(1):19-26.
24. Dai J, Zhao L, Yang H, Guo H, Fan K, Wang H, et al. Identification of a novel functional domain of ricin responsible for its potent toxicity. The Journal of biological chemistry. 2011;286(14):12166-71.
25. O'Hara JM, Kasten-Jolly JC, Reynolds CE, Mantis NJ. Localization of non-linear neutralizing B cell epitopes on ricin toxin's enzymatic subunit (RTA). Immunology letters. 2014;158(1-2):7-13.
26. O'Hara JM, Neal LM, McCarthy EA, Kasten-Jolly JA, Brey RN, 3rd, Mantis NJ. Folding domains within the ricin toxin A subunit as targets of protective antibodies. Vaccine. 2010;28(43):7035-46.
27. Vance DJ, Mantis NJ. Resolution of two overlapping neutralizing B cell epitopes within a solvent exposed, immunodominant alpha-helix in ricin toxin's enzymatic subunit. Toxicon : official journal of the International Society on Toxinology. 2012;60(5):874-7.
28. Baenziger JU, Fiete D. Structural determinants of Ricinus communis agglutinin and toxin specificity for oligosaccharides. The Journal of biological chemistry. 1979;254(19):9795-9.
29. Newton DL, Wales R, Richardson PT, Walbridge S, Saxena SK, Ackerman EJ, et al. Cell surface and intracellular functions for ricin galactose binding. The Journal of biological chemistry. 1992;267(17):11917-22.
30. Zentz C, Frenoy JP, Bourrillon R. Binding of galactose and lactose to ricin. Equilibrium studies. Biochimica et biophysica acta. 1978;536(1):18-26.
31. Kende M, Yan C, Hewetson J, Frick MA, Rill WL, Tammariello R. Oral immunization of mice with ricin toxoid vaccine encapsulated in polymeric microspheres against aerosol challenge. Vaccine. 2002;20(11-12):1681-91.
32. Yan C, Rill WL, Malli R, Hewetson J, Tammariello R, Kende M. Dependence of ricin toxoid vaccine efficacy on the structure of poly(lactide-co-glycolide) microparticle carriers. Vaccine. 1995;13(7):645-51.
33. Griffiths GD, Bailey SC, Hambrook JL, Keyte M, Jayasekera P, Miles J, et al. Liposomally-encapsulated ricin toxoid vaccine delivered intratracheally elicits a good immune response and protects against a lethal pulmonary dose of ricin toxin. Vaccine. 1997;15(17-18):1933-9.
34. Kende M, Del Giudice G, Rivera N, Hewetson J. Enhancement of intranasal vaccination in mice with deglycosylated chain A ricin by LTR72, a novel mucosal adjuvant. Vaccine. 2006;24(12):2213-21.

35. Reisler RB, Smith LA. The need for continued development of ricin countermeasures. Advances in preventive medicine. 2012;2012:149737.
36. Smallshaw JE, Vitetta ES. Ricin vaccine development. Current topics in microbiology and immunology. 2012;357:259-72.
37. Smallshaw JE, Firan A, Fulmer JR, Ruback SL, Ghetie V, Vitetta ES. A novel recombinant vaccine which protects mice against ricin intoxication. Vaccine. 2002;20(27-28):3422-7.
38. Smallshaw JE, Ghetie V, Rizo J, Fulmer JR, Trahan LL, Ghetie MA, et al. Genetic engineering of an immunotoxin to eliminate pulmonary vascular leak in mice. Nature biotechnology. 2003;21(4):387-91.
39. Legler PM, Brey RN, Smallshaw JE, Vitetta ES, Millard CB. Structure of RiVax: a recombinant ricin vaccine. Acta crystallographica Section D, Biological crystallography. 2011;67(Pt 9):826-30.
40. McHugh CA, Tammariello RF, Millard CB, Carra JH. Improved stability of a protein vaccine through elimination of a partially unfolded state. Protein Sci. 2004;13(10):2736-43.
41. Olson MA, Carra JH, Roxas-Duncan V, Wannemacher RW, Smith LA, Millard CB. Finding a new vaccine in the ricin protein fold. Protein Eng Des Sel. 2004;17(4):391-7.
42. Carra JH, Wannemacher RW, Tammariello RF, Lindsey CY, Dinterman RE, Schokman RD, et al. Improved formulation of a recombinant ricin A-chain vaccine increases its stability and effective antigenicity. Vaccine. 2007;25(21):4149-58.
43. Compton JR, Legler PM, Clingan BV, Olson MA, Millard CB. Introduction of a disulfide bond leads to stabilization and crystallization of a ricin immunogen. Proteins. 2011;79(4):1048-60.
44. Smallshaw JE, Richardson JA, Vitetta ES. RiVax, a recombinant ricin subunit vaccine, protects mice against ricin delivered by gavage or aerosol. Vaccine. 2007;25(42):7459-69.
45. Marconescu PS, Smallshaw JE, Pop LM, Ruback SL, Vitetta ES. Intradermal administration of RiVax protects mice from mucosal and systemic ricin intoxication. Vaccine. 2010;28(32):5315-22.
46. Smallshaw JE, Richardson JA, Pincus S, Schindler J, Vitetta ES. Preclinical toxicity and efficacy testing of RiVax, a recombinant protein vaccine against ricin. Vaccine. 2005;23(39):4775-84.
47. McLain DE, Horn TL, Detrisac CJ, Lindsey CY, Smith LA. Progress in biological threat agent vaccine development: a repeat-dose toxicity study of a recombinant ricin toxin A-chain (rRTA) 1-33/44-198 vaccine (RVEc) in male and female New Zealand white rabbits. International journal of toxicology. 2011;30(2):143-52.
48. McLain DE, Lewis BS, Chapman JL, Wannemacher RW, Lindsey CY, Smith LA. Protective effect of two recombinant ricin subunit vaccines in the New Zealand white rabbit subjected to a lethal aerosolized ricin challenge: survival, immunological response, and histopathological findings. Toxicological sciences : an official journal of the Society of Toxicology. 2012;126(1):72-83.
49. O'Hara JM, Brey RN, 3rd, Mantis NJ. Comparative efficacy of two leading candidate ricin toxin a subunit vaccines in mice. Clinical and vaccine immunology : CVI. 2013;20(6):789-94.
50. Pittman PR, Reisler RB, Lindsey CY, Guerena F, Rivard R, Clizbe DP, et al. Safety and immunogenicity of ricin vaccine, RVEc, in a Phase 1 clinical trial. Vaccine. 2015;33(51):7299-306.
51. Vitetta ES, Smallshaw JE, Schindler J. Pilot phase IB clinical trial of an alhydrogel-adsorbed recombinant ricin vaccine. Clinical and vaccine immunology : CVI. 2012;19(10):1697-9.
52. Vance DJ, Mantis NJ. Progress and challenges associated with the development of ricin toxin subunit vaccines. Expert review of vaccines. 2016;15(9):1213-22.
53. Roy CJ, Brey RN, Mantis NJ, Mapes K, Pop IV, Pop LM, et al. Thermostable ricin vaccine protects rhesus macaques against aerosolized ricin: Epitope-specific neutralizing antibodies correlate with protection. Proceedings of the National Academy of Sciences of the United States of America. 2015;112(12):3782-7.
54. Hassett KJ, Cousins MC, Rabia LA, Chadwick CM, O'Hara JM, Nandi P, et al. Stabilization of a recombinant ricin toxin A subunit vaccine through lyophilization. European journal of pharmaceutics and

biopharmaceutics : official journal of Arbeitsgemeinschaft fur Pharmazeutische Verfahrenstechnik eV. 2013;85(2):279-86.
55. Janosi L, Compton JR, Legler PM, Steele KE, Davis JM, Matyas GR, et al. Disruption of the putative vascular leak peptide sequence in the stabilized ricin vaccine candidate RTA1-33/44-198. Toxins. 2013;5(2):224-48.
56. Neal LM, O'Hara J, Brey RN, 3rd, Mantis NJ. A monoclonal immunoglobulin G antibody directed against an immunodominant linear epitope on the ricin A chain confers systemic and mucosal immunity to ricin. Infection and immunity. 2010;78(1):552-61.
57. Sully EK, Whaley KJ, Bohorova N, Bohorov O, Goodman C, Kim DH, et al. Chimeric plantibody passively protects mice against aerosolized ricin challenge. Clinical and vaccine immunology : CVI. 2014;21(5):777-82.
58. Pincus SH, Das A, Song K, Maresh GA, Corti M, Berry J. Role of Fc in antibody-mediated protection from ricin toxin. Toxins. 2014;6(5):1512-25.
59. Prigent J, Panigai L, Lamourette P, Sauvaire D, Devilliers K, Plaisance M, et al. Neutralising antibodies against ricin toxin. PloS one. 2011;6(5):e20166.
60. Yermakova A, Mantis NJ. Protective immunity to ricin toxin conferred by antibodies against the toxin's binding subunit (RTB). Vaccine. 2011;29(45):7925-35.
61. Yermakova A, Mantis NJ. Neutralizing activity and protective immunity to ricin toxin conferred by B subunit (RTB)-specific Fab fragments. Toxicon : official journal of the International Society on Toxinology. 2013;72:29-34.
62. Vance DJ, Greene CJ, Rong Y, Mandell LM, Connell TD, Mantis NJ. Comparative Adjuvant Effects of Type II Heat-Labile Enterotoxins in Combination with Two Different Candidate Ricin Toxin Vaccine Antigens. Clinical and vaccine immunology : CVI. 2015;22(12):1285-93.
63. Vance DJ, Rong Y, Brey RN, 3rd, Mantis NJ. Combination of two candidate subunit vaccine antigens elicits protective immunity to ricin and anthrax toxin in mice. Vaccine. 2015;33(3):417-21.
64. Burbelo PD, Ching KH, Bush ER, Han BL, Iadarola MJ. Antibody-profiling technologies for studying humoral responses to infectious agents. Expert review of vaccines. 2010;9(6):567-78.
65. Furman D, Davis MM. New approaches to understanding the immune response to vaccination and infection. Vaccine. 2015;33(40):5271-81.
66. Lemley PV, Amanatides P, Wright DC. Identification and characterization of a monoclonal antibody that neutralizes ricin toxicity in vitro and in vivo. Hybridoma. 1994;13(5):417-21.
67. Zhu Y, Dai J, Zhang T, Li X, Fang P, Wang H, et al. Structural insights into the neutralization mechanism of monoclonal antibody 6C2 against ricin. The Journal of biological chemistry. 2013;288(35):25165-72.
68. Toth Rt, Angalakurthi SK, Van Slyke G, Vance DJ, Hickey JM, Joshi SB, et al. High-Definition Mapping of Four Spatially Distinct Neutralizing Epitope Clusters on RiVax, a Candidate Ricin Toxin Subunit Vaccine. Clinical and vaccine immunology : CVI. 2017.
69. Vance DJ, Tremblay JM, Mantis NJ, Shoemaker CB. Stepwise engineering of heterodimeric single domain camelid VHH antibodies that passively protect mice from ricin toxin. The Journal of biological chemistry. 2013;288(51):36538-47.
70. Hamers-Casterman C, Atarhouch T, Muyldermans S, Robinson G, Hamers C, Songa EB, et al. Naturally occurring antibodies devoid of light chains. Nature. 1993;363(6428):446-8.
71. De Genst E, Silence K, Decanniere K, Conrath K, Loris R, Kinne J, et al. Molecular basis for the preferential cleft recognition by dromedary heavy-chain antibodies. Proceedings of the National Academy of Sciences of the United States of America. 2006;103(12):4586-91.
72. Arbabi Ghahroudi M, Desmyter A, Wyns L, Hamers R, Muyldermans S. Selection and identification of single domain antibody fragments from camel heavy-chain antibodies. FEBS letters. 1997;414(3):521-6.

73. Conrath K, Vincke C, Stijlemans B, Schymkowitz J, Decanniere K, Wyns L, et al. Antigen binding and solubility effects upon the veneering of a camel VHH in framework-2 to mimic a VH. Journal of molecular biology. 2005;350(1):112-25.
74. Dumoulin M, Conrath K, Van Meirhaeghe A, Meersman F, Heremans K, Frenken LG, et al. Single-domain antibody fragments with high conformational stability. Protein science : a publication of the Protein Society. 2002;11(3):500-15.
75. Dolk E, van Vliet C, Perez JM, Vriend G, Darbon H, Ferrat G, et al. Induced refolding of a temperature denatured llama heavy-chain antibody fragment by its antigen. Proteins. 2005;59(3):555-64.
76. Walper SA, Anderson GP, Brozozog Lee PA, Glaven RH, Liu JL, Bernstein RD, et al. Rugged single domain antibody detection elements for Bacillus anthracis spores and vegetative cells. PloS one. 2012;7(3):e32801.
77. Vance DJ, Tremblay JM, Rong Y, Angalakurthi SK, Volkin DB, Middaugh CR, et al. High-Resolution Epitope Positioning of a Large Collection of Neutralizing and Non-Neutralizing Single Domain Antibodies on Ricin Toxin's Enzymatic and Binding Subunits. Clinical and vaccine immunology : CVI. 2017.
78. Rudolph MJ, Vance DJ, Cheung J, Franklin MC, Burshteyn F, Cassidy MS, et al. Crystal structures of ricin toxin's enzymatic subunit (RTA) in complex with neutralizing and non-neutralizing single-chain antibodies. Journal of molecular biology. 2014;426(17):3057-68.
79. Rudolph MJ, Vance DJ, Cassidy MS, Rong Y, Shoemaker CB, Mantis NJ. Structural analysis of nested neutralizing and non-neutralizing B cell epitopes on ricin toxin's enzymatic subunit. Proteins. 2016;84(8):1162-72.
80. Angulo J, Nieto PM. STD-NMR: application to transient interactions between biomolecules-a quantitative approach. European biophysics journal : EBJ. 2011;40(12):1357-69.
81. Chen E, Salinas ND, Huang Y, Ntumngia F, Plasencia MD, Gross ML, et al. Broadly neutralizing epitopes in the Plasmodium vivax vaccine candidate Duffy Binding Protein. Proceedings of the National Academy of Sciences of the United States of America. 2016;113(22):6277-82.
82. Gribenko AV, Parris K, Mosyak L, Li S, Handke L, Hawkins JC, et al. High Resolution Mapping of Bactericidal Monoclonal Antibody Binding Epitopes on Staphylococcus aureus Antigen MntC. PLoS pathogens. 2016;12(9):e1005908.
83. Lim XX, Chandramohan A, Lim XE, Crowe JE, Jr., Lok SM, Anand GS. Epitope and Paratope Mapping Reveals Temperature-Dependent Alterations in the Dengue-Antibody Interface. Structure (London, England : 1993). 2017;25(9):1391-402.e3.
84. Malito E, Faleri A, Lo Surdo P, Veggi D, Maruggi G, Grassi E, et al. Defining a protective epitope on factor H binding protein, a key meningococcal virulence factor and vaccine antigen. Proceedings of the National Academy of Sciences of the United States of America. 2013;110(9):3304-9.
85. Hvidt A, Linderstrom-Lang K. Exchange of hydrogen atoms in insulin with deuterium atoms in aqueous solutions. Biochimica et biophysica acta. 1954;14(4):574-5.
86. Englander SW, Mayne L. Protein folding studied using hydrogen-exchange labeling and two-dimensional NMR. Annual review of biophysics and biomolecular structure. 1992;21:243-65.
87. Haris PI, Chapman D. The conformational analysis of peptides using Fourier transform IR spectroscopy. Biopolymers. 1995;37(4):251-63.
88. Katta V, Chait BT. Conformational changes in proteins probed by hydrogen-exchange electrospray-ionization mass spectrometry. Rapid communications in mass spectrometry : RCM. 1991;5(4):214-7.
89. Zhang Z, Smith DL. Determination of amide hydrogen exchange by mass spectrometry: a new tool for protein structure elucidation. Protein science : a publication of the Protein Society. 1993;2(4):522-31.

90. Houde D, Arndt J, Domeier W, Berkowitz S, Engen JR. Characterization of IgG1 Conformation and Conformational Dynamics by Hydrogen/Deuterium Exchange Mass Spectrometry. Analytical chemistry. 2009;81(14):5966.
91. Houde D, Peng Y, Berkowitz SA, Engen JR. Post-translational modifications differentially affect IgG1 conformation and receptor binding. Molecular & cellular proteomics : MCP. 2010;9(8):1716-28.
92. Burkitt W, Domann P, O'Connor G. Conformational changes in oxidatively stressed monoclonal antibodies studied by hydrogen exchange mass spectrometry. Protein science : a publication of the Protein Society. 2010;19(4):826-35.
93. Englander SW, Kallenbach NR. Hydrogen exchange and structural dynamics of proteins and nucleic acids. Quarterly reviews of biophysics. 1983;16(4):521-655.
94. Smith DL, Deng Y, Zhang Z. Probing the non-covalent structure of proteins by amide hydrogen exchange and mass spectrometry. Journal of mass spectrometry : JMS. 1997;32(2):135-46.
95. Deng Y, Smith DL. Identification of unfolding domains in large proteins by their unfolding rates. Biochemistry. 1998;37(18):6256-62.
96. Engen JR, Wales TE, Chen S, Marzluff EM, Hassell KM, Weis DD, et al. Partial cooperative unfolding in proteins as observed by hydrogen exchange mass spectrometry. International reviews in physical chemistry. 2013;32(1):96-127.
97. Pandit D, Tuske SJ, Coales SJ, E SY, Liu A, Lee JE, et al. Mapping of discontinuous conformational epitopes by amide hydrogen/deuterium exchange mass spectrometry and computational docking. Journal of molecular recognition : JMR. 2012;25(3):114-24.
98. Wei H, Mo J, Tao L, Russell RJ, Tymiak AA, Chen G, et al. Hydrogen/deuterium exchange mass spectrometry for probing higher order structure of protein therapeutics: methodology and applications. Drug discovery today. 2014;19(1):95-102.
99. Angalakurthi SK, Tenorio CA, Blaber M, Middaugh CR. Investigating the dynamics and polyanion binding sites of fibroblast growth factor-1 using hydrogen-deuterium exchange mass spectrometry. Protein science : a publication of the Protein Society. 2018;27(6):1068-82.
100. Zhang Q, Willison LN, Tripathi P, Sathe SK, Roux KH, Emmett MR, et al. Epitope mapping of a 95 kDa antigen in complex with antibody by solution-phase amide backbone hydrogen/deuterium exchange monitored by Fourier transform ion cyclotron resonance mass spectrometry. Analytical chemistry. 2011;83(18):7129-36.
101. Walters BT, Ricciuti A, Mayne L, Englander SW. Minimizing back exchange in the hydrogen exchange-mass spectrometry experiment. Journal of the American Society for Mass Spectrometry. 2012;23(12):2132-9.
102. Venable JD, Okach L, Agarwalla S, Brock A. Subzero temperature chromatography for reduced back-exchange and improved dynamic range in amide hydrogen/deuterium exchange mass spectrometry. Analytical chemistry. 2012;84(21):9601-8.
103. Valeja SG, Emmett MR, Marshall AG. Polar aprotic modifiers for chromatographic separation and back-exchange reduction for protein hydrogen/deuterium exchange monitored by Fourier transform ion cyclotron resonance mass spectrometry. Journal of the American Society for Mass Spectrometry. 2012;23(4):699-707.
104. Bazzoli A, Vance DJ, Rudolph MJ, Rong Y, Angalakurthi SK, Toth RTt, et al. Using homology modeling to interrogate binding affinity in neutralization of ricin toxin by a family of single domain antibodies. Proteins. 2017.
105. Itoh N, Ornitz DM. Evolution of the Fgf and Fgfr gene families. Trends in genetics : TIG. 2004;20(11):563-9.
106. Olsen SK, Garbi M, Zampieri N, Eliseenkova AV, Ornitz DM, Goldfarb M, et al. Fibroblast growth factor (FGF) homologous factors share structural but not functional homology with FGFs. The Journal of biological chemistry. 2003;278(36):34226-36.

107. Ornitz DM, Xu J, Colvin JS, McEwen DG, MacArthur CA, Coulier F, et al. Receptor specificity of the fibroblast growth factor family. The Journal of biological chemistry. 1996;271(25):15292-7.
108. Zhang X, Ibrahimi OA, Olsen SK, Umemori H, Mohammadi M, Ornitz DM. Receptor specificity of the fibroblast growth factor family. The complete mammalian FGF family. The Journal of biological chemistry. 2006;281(23):15694-700.
109. Spivak-Kroizman T, Lemmon MA, Dikic I, Ladbury JE, Pinchasi D, Huang J, et al. Heparin-induced oligomerization of FGF molecules is responsible for FGF receptor dimerization, activation, and cell proliferation. Cell. 1994;79(6):1015-24.
110. Lin X, Buff EM, Perrimon N, Michelson AM. Heparan sulfate proteoglycans are essential for FGF receptor signaling during Drosophila embryonic development. Development (Cambridge, England). 1999;126(17):3715-23.
111. Rapraeger AC, Krufka A, Olwin BB. Requirement of heparan sulfate for bFGF-mediated fibroblast growth and myoblast differentiation. Science (New York, NY). 1991;252(5013):1705-8.
112. DiGabriele AD, Lax I, Chen DI, Svahn CM, Jaye M, Schlessinger J, et al. Structure of a heparin-linked biologically active dimer of fibroblast growth factor. Nature. 1998;393(6687):812-7.
113. Faham S, Hileman RE, Fromm JR, Linhardt RJ, Rees DC. Heparin structure and interactions with basic fibroblast growth factor. Science (New York, NY). 1996;271(5252):1116-20.
114. Plotnikov AN, Hubbard SR, Schlessinger J, Mohammadi M. Crystal structures of two FGF-FGFR complexes reveal the determinants of ligand-receptor specificity. Cell. 2000;101(4):413-24.
115. Stauber DJ, DiGabriele AD, Hendrickson WA. Structural interactions of fibroblast growth factor receptor with its ligands. Proceedings of the National Academy of Sciences of the United States of America. 2000;97(1):49-54.
116. Pellegrini L, Burke DF, von Delft F, Mulloy B, Blundell TL. Crystal structure of fibroblast growth factor receptor ectodomain bound to ligand and heparin. Nature. 2000;407(6807):1029-34.
117. Rosengart TK, Kuperschmid JP, Maciag T, Clark RE. Pharmacokinetics and distribution of heparin-binding growth factor I (endothelial cell growth factor) in the rat. Circulation research. 1989;64(2):227-34.
118. Hondermarck H, Courty J, Boilly B, Thomas D. Distribution of intravenously administered acidic and basic fibroblast growth factors in the mouse. Experientia. 1990;46(9):973-4.
119. Hacker U, Nybakken K, Perrimon N. Heparan sulphate proteoglycans: the sweet side of development. Nature reviews Molecular cell biology. 2005;6(7):530-41.
120. Blaber M, DiSalvo J, Thomas KA. X-ray crystal structure of human acidic fibroblast growth factor. Biochemistry. 1996;35(7):2086-94.
121. Zhu X, Komiya H, Chirino A, Faham S, Fox GM, Arakawa T, et al. Three-dimensional structures of acidic and basic fibroblast growth factors. Science (New York, NY). 1991;251(4989):90-3.
122. Murzin AG, Lesk AM, Chothia C. beta-Trefoil fold. Patterns of structure and sequence in the Kunitz inhibitors interleukins-1 beta and 1 alpha and fibroblast growth factors. Journal of molecular biology. 1992;223(2):531-43.
123. Xu R, Ori A, Rudd TR, Uniewicz KA, Ahmed YA, Guimond SE, et al. Diversification of the structural determinants of fibroblast growth factor-heparin interactions: implications for binding specificity. The Journal of biological chemistry. 2012;287(47):40061-73.
124. Harper JW, Lobb RR. Reductive methylation of lysine residues in acidic fibroblast growth factor: effect on mitogenic activity and heparin affinity. Biochemistry. 1988;27(2):671-8.
125. Seddon AP, Aviezer D, Li LY, Bohlen P, Yayon A. Engineering of fibroblast growth factor: alteration of receptor binding specificity. Biochemistry. 1995;34(3):731-6.
126. Patrie KM, Botelho MJ, Franklin K, Chiu IM. Site-directed mutagenesis and molecular modeling identify a crucial amino acid in specifying the heparin affinity of FGF-1. Biochemistry. 1999;38(29):9264-72.

127. Beenken A, Eliseenkova AV, Ibrahimi OA, Olsen SK, Mohammadi M. Plasticity in interactions of fibroblast growth factor 1 (FGF1) N terminus with FGF receptors underlies promiscuity of FGF1. The Journal of biological chemistry. 2012;287(5):3067-78.
128. Copeland RA, Ji H, Halfpenny AJ, Williams RW, Thompson KC, Herber WK, et al. The structure of human acidic fibroblast growth factor and its interaction with heparin. Archives of biochemistry and biophysics. 1991;289(1):53-61.
129. Gospodarowicz D, Cheng J. Heparin protects basic and acidic FGF from inactivation. Journal of cellular physiology. 1986;128(3):475-84.
130. Rosengart TK, Johnson WV, Friesel R, Clark R, Maciag T. Heparin protects heparin-binding growth factor-I from proteolytic inactivation in vitro. Biochemical and biophysical research communications. 1988;152(1):432-40.
131. ten Dijke P, Iwata KK. Growth Factors For Wound Healing. Bio/Technology. 1989;7:793.
132. Steed DL. THE ROLE OF GROWTH FACTORS IN WOUND HEALING. Surgical Clinics of North America. 1997;77(3):575-86.
133. Dabora JM, Sanyal G, Middaugh CR. Effect of polyanions on the refolding of human acidic fibroblast growth factor. The Journal of biological chemistry. 1991;266(35):23637-40.
134. Volkin DB, Tsai PK, Dabora JM, Gress JO, Burke CJ, Linhardt RJ, et al. Physical stabilization of acidic fibroblast growth factor by polyanions. Archives of biochemistry and biophysics. 1993;300(1):30-41.

CHAPTER 2

B cell Epitope Mapping by Hydrogen Exchange Mass Spectrometry of an Immunodominant Region Surrounding Ricin Toxin's Active Site

Introduction

Ricin toxin is a member of the ribosome-inactivating protein family that includes Shiga, verotoxin and abrin (1). Ricin toxin is a 65 kDa glycoprotein that is comprised of two subunits, RTA and RTB, joined by a single disulfide bond (2, 3). RTA, which possesses the enzymatic site, inactivates eukaryotic ribosomes by cleaving the highly conserved adenine residue (A_{4324}) within the sarcin-ricin loop of 28S ribosomal RNA (4, 5). RTB, ricin's binding subunit, is a Gal- and GalNAc-specific lectin which mediates toxin entry into the mammalian host cell (6). Ricin can effectively intoxicate all known eukaryotic cell types.

Five residues (Tyr80, Tyr123, Glu177, Arg180, Trp211) play critical roles in RTA's enzymatic activity (7). The active site in RTA consist of residues located in various secondary structure elements including helices C, E and G. At the tertiary structural level, RTA assumes a globular fold that can be divided into three distinct folding domains (2, 3). Folding domain I (residues 1-117), conserved among other ribosome inactivating protein toxins, consists of eight β-strands (a-h) and two α-helices (A and B). Folding domain II (residues 118-210) is dominated by five α-helices (C-G). Folding domain 3 (residues 211-267), which has two β-strands (i and j), interacts with RTB through hydrophobic interactions as well as a disulfide bond (2, 3). Structurally, most of the active site falls within folding domains 1 and 2. Residue Y80 is located in the turn connecting strands e and f. Residue Y123 is located in the N–terminus of helix C. Residues Glu177 and Arg180 are located in the C-terminus of helix E. Finally residue Trp211 is located in the center of helix G. In the folded RTA, all the above mentioned residues are placed close to each other forming a shallow pocket like structure (Figure 1a).

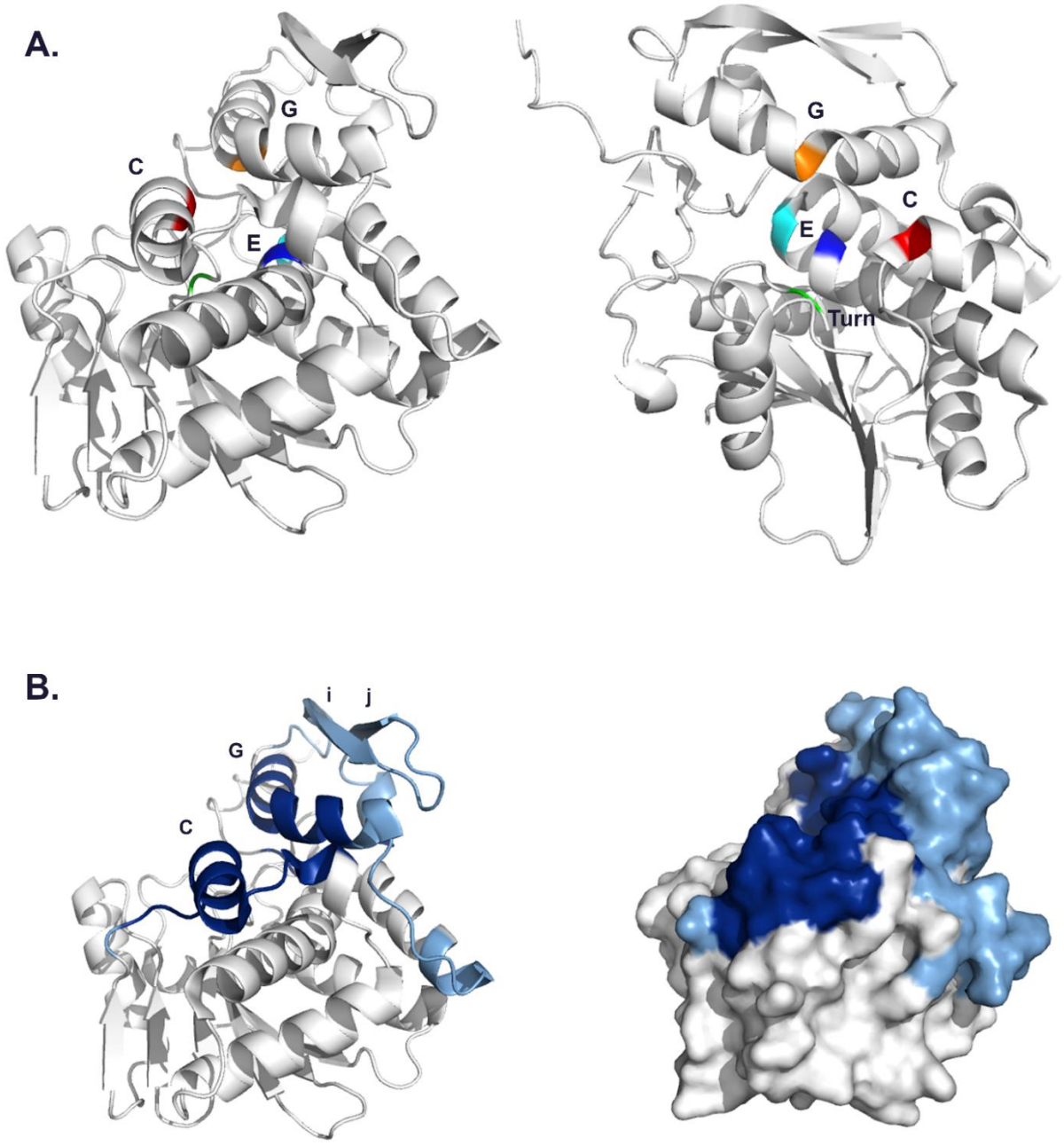

Figure 1. Crystal structure of RiVax a) left panel shows the residues that constitute active site located in various α-helices including C, G and E; right panel shows the top view of toxin's active site that form a shallow pocket like structure. The colored residues correspond to the following: green, Tyr80; red, Tyr123; blue, Glu 177; cyan, Arg 180; orange, Trp 211. (b) Location of the epitope of IB2 on RiVax (PDB ID: 3SRP). The color shading corresponds to the following; deep blue, strong protection; light blue, intermediate protection; grey, non–significant. The data are taken from our previous work (24).

Despite a good understanding of the toxin's structure and function, there is no approved vaccine for ricin toxin. A leading vaccine candidate is RiVax. RiVax is a full-length derivative of RTA that has two point mutations aimed at eliminating enzymatic activity (Y80A) as well as vascular leak syndrome (V76M) associated with ricin toxicity. X-ray crystallography has shown that RiVax is very similar to RTA, indicating that the substitutions do not alter the tertiary structure of RTA (7). Toxin-neutralizing antibodies target limited "hot spots" on RTA's surface that we have designated epitope clusters I-IV (8-10). Cluster I, defined by mAbs PB10, R70 and WECB2, encompasses α-helix B and β-strand h. Cluster II is recognized by nine mAbs, most notably SyH7, that target two distinct sub-clusters on the backside of the toxin: one sub-cluster defined by the loop connecting α-helices F and G, the other encompassing two loops, bridging β-strands d and e and α-helices D and E. Cluster IV is defined by GD12 and JD4, which bind to β-strands b-d [(11), G Van Slyke et al, *manuscript submitted*].

The mAb IB2 defines Cluster 3. IB2 was first reported by O'Hara et al (8) where we relied on competitive binding assays to identify its epitope location. We found its epitope to be distinct from that of known toxin neutralizing antibody epitopes that fall in cluster I and II, however, we could not determine the exact epitope site of IB2 in that report. IB2 was later studied in other papers (12) where we show that it interferes with retrograde transport and protein disulfide isomerase (PDI) interactions with ricin (13). IB2 doesn't bind to RTA on microtiter plate presumably due to local conformational changes. In other words, the cluster is highly conformationally specific.

To localize IB2's epitope, we performed hydrogen-exchange mass spectrometry (HX-MS). Of late, HX-MS has been increasingly used in epitope mapping studies (14-16). RiVax in the presence of its cognate antibody shows a decrease in deuterium uptake in the regions where antibody binds

to. In other words, protection (from deuterium uptake) is observed in the regions where antibody makes contact. More details in identifying an epitope region using HX-MS method is described in the result section. Analysis revealed that IB2 strongly protects α-helices C (residues 119-135) and G (residues 205-217), as well as a short region (residues 249-255) in RTA's C-terminus (Figure 1b) (11). Beyond IB2, very little is known about so-called cluster 3, even though it is clearly a target of toxin-neutralizing antibodies.

To better understand cluster 3, we recently screened camelid antibody library for V_HHs that competed with IB2 (17). We identified nine. In a separate screen we identified an additional unique V_HHs that competes (D. Vance. C. Shoemaker, N. Mantis, manuscript in preparation). Therefore, we have a collection of 21 V_HHs that are operationally defined as being with Cluster 3. In this study, we localized by HX-MS the epitopes of all 21 of these V_HHs. We found that the 21 V_HHs fall within one of four distinct but overlapping subclusters (3.1-3.4) that share at least one secondary element contacted by IB2. Only two of the 21 V_HHs, V6D4 and V1D3, have appreciable toxin-neutralizing activity (TNA), which we speculate is due to their epitope specificity along with strong binding affinity to toxin. Evidence points to helix G being important in neutralizing activity. This work furthers our overall goal of constructing a complete epitope map of ricin toxin.

Results and Discussion

Identification and characterization of Cluster 3 V_HHs. We identified a total of 21 V_HHs that were partially or completely unable to bind to ricin that had been captured by IB2 (Figure 2). The predicted amino acid sequences of the 21 V_HHs suggested that they represent eleven B cell lineages based on CDR3 similarity: five unique V_HHs and 16 that fell into one of six sequence families (Table 1, Figure S1). The binding kinetics of each V_HH for ricin was determined by surface plasmon resonance (SPR). Twelve of the 21 V_HHs had dissociation constants (K_d) of greater than 1 nM, while nine had dissociation constants ranging from 200-996 pM (Table 2). When tested in a ricin cytotoxicity assay, only V6D4 (IC_{50}, 200 nM) and V1D3 (IC_{50}, 80 nM) had demonstrable toxin-neutralizing activity (TNA). Seven other V_HHs had K_ds comparable to V6D4 and V1D3 but did not have TNA, indicating that occupancy (not just binding affinity) on RTA impacts ricin toxicity. For that reason, we sought to localize the epitopes on RTA recognized by each of the 21 V_HHs. The epitopes recognized by JNM-D1 and V1B11 were previously been defined by hydrogen-exchange mass spectrometry (HX-MS) analysis (17). We therefore examined the remaining 19 V_HHs.

Table 1. V_HH Families based on CDR3 similarity

Family	Members
V1D3[a]	JIV-F6, V1B10
V2A11	V6H8
V2G10	V1G6
V6D8	V6F12
V6A6	V6A7, V6G10, V8C7, V8E6
V6D4	V6B4
Unique	JNM-A11, JNM-D1, V1B11, V5A2, V7H7

[a], underline indicates V_HHs with toxin-neutralizing activity

Table 2. V_HH Binding Affinities and TNA

V_HH	IC_{50}[a]	K_D[a]	k_{on}[b]	k_{off}[c]
JIV-F6	-	1.860	1.94E+05	3.61E-04
JNM-A11	-	0.200	4.45E+05	8.92E-05
JNM-D1	-	1.190	1.80E+05	2.15E-04
V1B10	-	0.917	8.29E+04	7.60E-05
V1B11	-	8.840	2.76E+04	2.44E-04
V1D3	80	0.460	3.15E+05	1.45E-04
V1G6	-	5.340	3.05E+04	1.63E-04
V2A11	-	1.820	2.97E+04	5.41E-05
V2G10	-	1.160	8.48E+04	9.84E-05
V5A2	-	1.460	2.15E+05	3.14E-04
V6A6	-	0.996	5.06E+05	5.04E-04
V6A7	-	1.760	7.70E+04	1.36E-04
V6B4	-	0.652	1.70E+05	1.11E-04
V6D4	200	0.224	1.44E+05	3.22E-05
V6D8	-	1.130	2.14E+05	2.41E-04
V6F12	-	1.210	1.80E+05	2.17E-04
V6G10	-	1.270	1.77E+05	2.24E-04
V6H8	-	1.150	6.63E+04	7.66E-05
V7H7	-	0.507	1.65E+05	8.36E-05
V8C7	-	0.597	1.58E+05	9.40E-05
V8E6	-	0.830	1.26E+05	1.04E-04

[a], nM; [b], $M^{-1}s^{-1}$; [c], M^{-1};

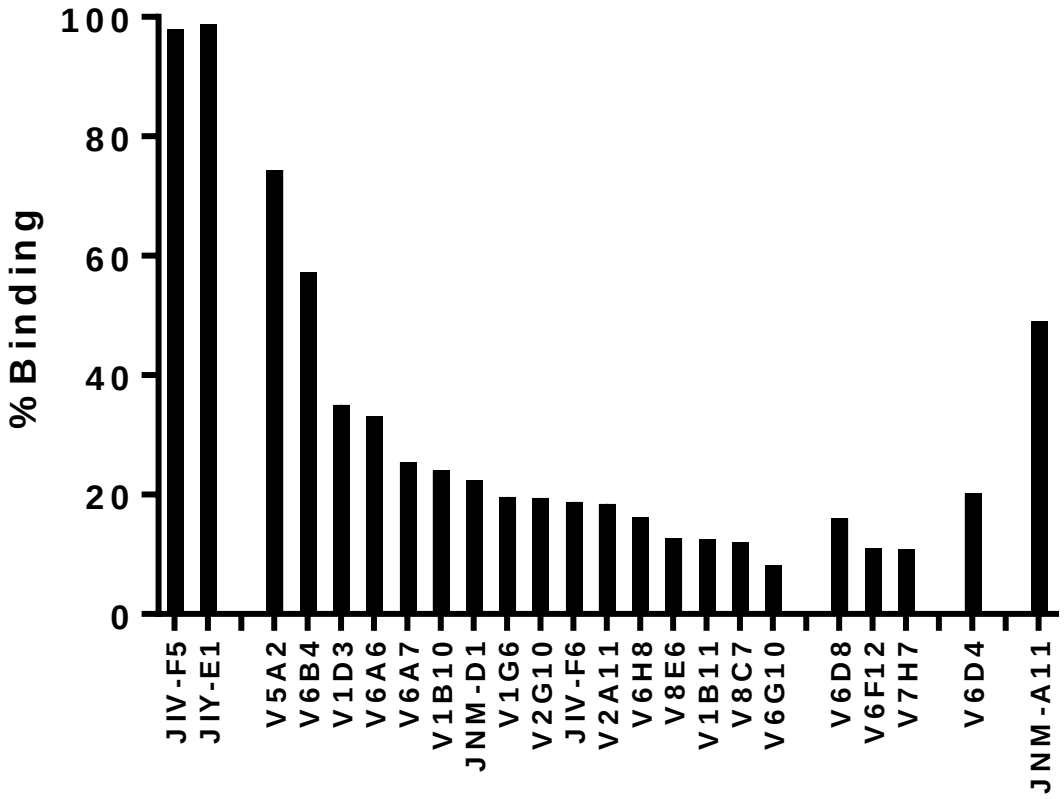

Figure 2. Competition assay to assign V_HHs to Cluster 3. Ricin was captured on immunoplates either by mAb IB2 or the anti-RTB mAb SylH3. V_HHs were then bound to ricin and detected. Normalized % binding was calculated as $100*(A_{IB2\text{-}Ricin}/A_{SylH3\text{-}Ricin})$. V_HHs along the x-axis are representative of Cluster I (JIV-F5), Cluster II (JIY-E1), Cluster 3 Sub-cluster 1 (V5A2-V6G10), Cluster 3 Sub-cluster 2 (V6D8-V7H7), Cluster 3 Sub-cluster 3 (V6D4), and Cluster 3 Sub-cluster 4 (JNM-A11).

Epitope mapping by HX-MS. We performed HX-MS analysis on RiVax in complex with each of the V_HHs at five exchange times between 13 s and 24 h, using previously established protocols (Toth 2017). For the labeling studies, V_HHs were present at a 2-fold molar excess to favor complex formation. V_HH contact points on RiVax were assigned based on reduced (slower) HX exchange for peptides in the presence of V_HH compared to with RiVax, as described in detail in Toth et al. (2017). For example, in the presence of V6B4 the HX rate in the peptide corresponding to RiVax residues 56-59 was unaltered, whereas there was much slower exchange observed for peptide

corresponding to residues 205-217 (Figure 3). Slower exchange is attributed to direct protein-protein interactions, which in the case of antibodies reveals epitopes. We have observed elsewhere that increased protection can also result from allosteric effects (11, 17).

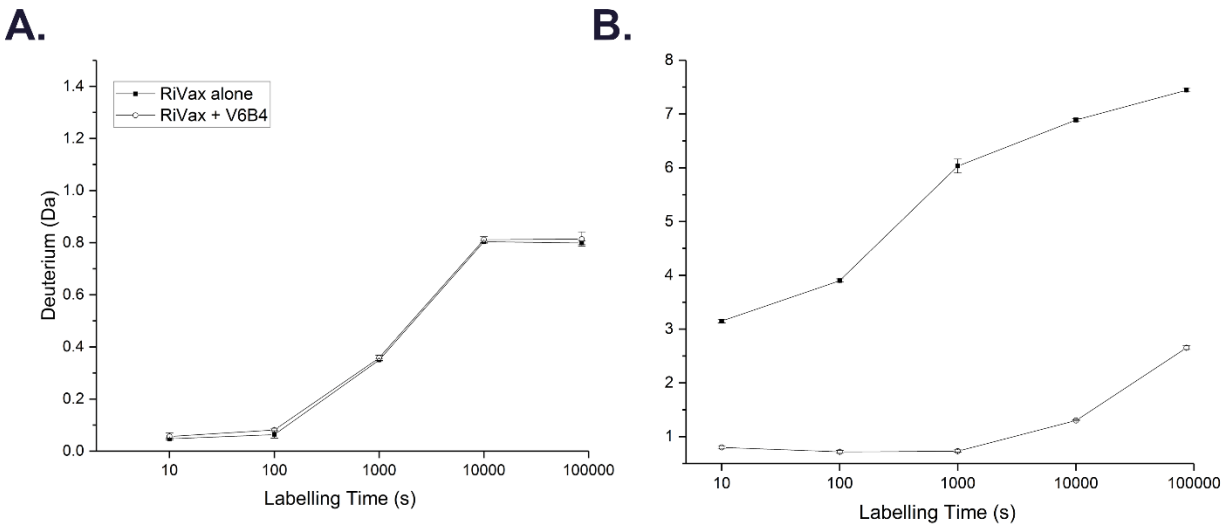

Figure 3. Hydrogen deuterium exchange kinetics of two representative RiVax peptides in presence of V6B4. A) Peptide 14 (56-59), where the HX rate was not affected by association with V6B4. B) Peptide 94 (205-217) where the rate of HX was substantially slowed by V6B4.

Upon completion of HX-MS analysis of all 21 V_HHs, we found that Cluster 3 V_HHs grouped within four sub-clusters (3.1-3.4) (Table 3, Table S1; Figure 10). Subcluster 3.1 involves contact with α-helices C and G, a profile very similar to IB2 (the mAb that defines cluster 3). Subcluster 3.2 encompasses α-helices B, C and G, while subcluster 3.3 covers α-helices B and G, but not α-helix C. Finally, sub-cluster 3.4 encompasses α-helices C and E, but not G. Each of these sub-clusters is described in more detail below and depicted in cartoon form in Figure 10.

Table 3. RiVax peptides, residues, and secondary structures protected by Cluster 3 V_HHs.				
		Strong and Intermediate Protected Elements [a]		
V_HH	**Subcluster**	**Peptides**	**Residues**	**Secondary Structure(s)**
V6B4	3.1	48-51	119-133	α-helix C
		91-102	205-217	α-helix G
		132-134	249-255	
V1D3		54,55	127-135	α-helix C
		91	205-210	α-helix G
		112-116	226-243	β-strands i, j
		132-134	249-255	
V6D8	3.2	35-39	92-107	α-helix B
		49-54	123-135	α-helix C
		102	211-217	α-helix G
		129-134	247-255	
V6F12		35-40	92-107	α-helix B
		47,49	118-126	α-helix C
		94,97,100,102-103	205-217	α-helix G
		132-134	249-255	
V7H7		35-39	92-107	α-helix B
		49	123-126	α-helix C
		94-95,97-98,100,102	205-217	α-helix G
		129-131	249-255	
V6D4	3.3	35-37,39	92-107	α-helix B
		102	211-217	α-helix G
		132-134	249-255	
JNM-A11	3.4	45,46	108-122	β-strand h
		49-51	124-133	α-helix C
		70,71	162-168	α-helix E
[a] Peptides and corresponding residues on RiVax are indicated in supplementary Table S2				

Subcluster 3.1: Sixteen of the twenty one V_HHs shared an HX-MS profile involving contact with α-helices C and G, which we refer to as subcluster 3.1 (**Table 3**; **Figures 4-5**; **Table S1**; **Figures S2, S3**). While the HX-MS profiles of the V_HHs within 3.1 were qualitatively similar, there were quantitative differences that may be significant in terms of neutralizing activity. For example, V1D3, one of the two V_HHs with TNA, had a binding pattern virtually identical to IB2 in that it strongly protected α-helix C (peptides 54-55, residues 127-135) and the C-terminus region (peptides 132-134, residues 249-255). Moreover, V1D3 demonstrated intermediate protection of α-helix G (peptide 91, residues 205-210), as well as strands i and j (peptides 112-116, residues 226-243).

In contrast, V6B4 strongly protected RiVax residues 119 to 133 (peptides 48-51), corresponding to α-helix C, and residues 205-217 (peptides 91 to 102), corresponding to α-helix G (Figure 4a, 5a) but differed from V1D3 in three respects. First, V6B4 had stronger protection of α-helix G than C, as compared to V1D3. Second, V1D3 interacted with β-strands i and j, while V6B4 does not, possibility indicating that V1D3 overall contact interface with RiVax is larger than V6B4's. Finally, the patterns of protection in α-helix C are distinct. In case of V6B4, the entirety of α-helix C is strongly protected, while in the case of V1D3 it is only the C-terminal end that is strongly protected (Figure 4a and 4b). V1D3 also caused intermediate protection in the N-terminal end of helix G while V6B4 has protected all of helix G. These differences in helix C and G protection could very well account for differences in toxin-neutralizing activity. Indeed, given the large number of V_HHs that fall into this sub-cluster, it is possible that there are several different orientations of V_HH binding that would only be resolved through V_HH-RTA co-crystal structures as done previously by our group (10, 18, 19).

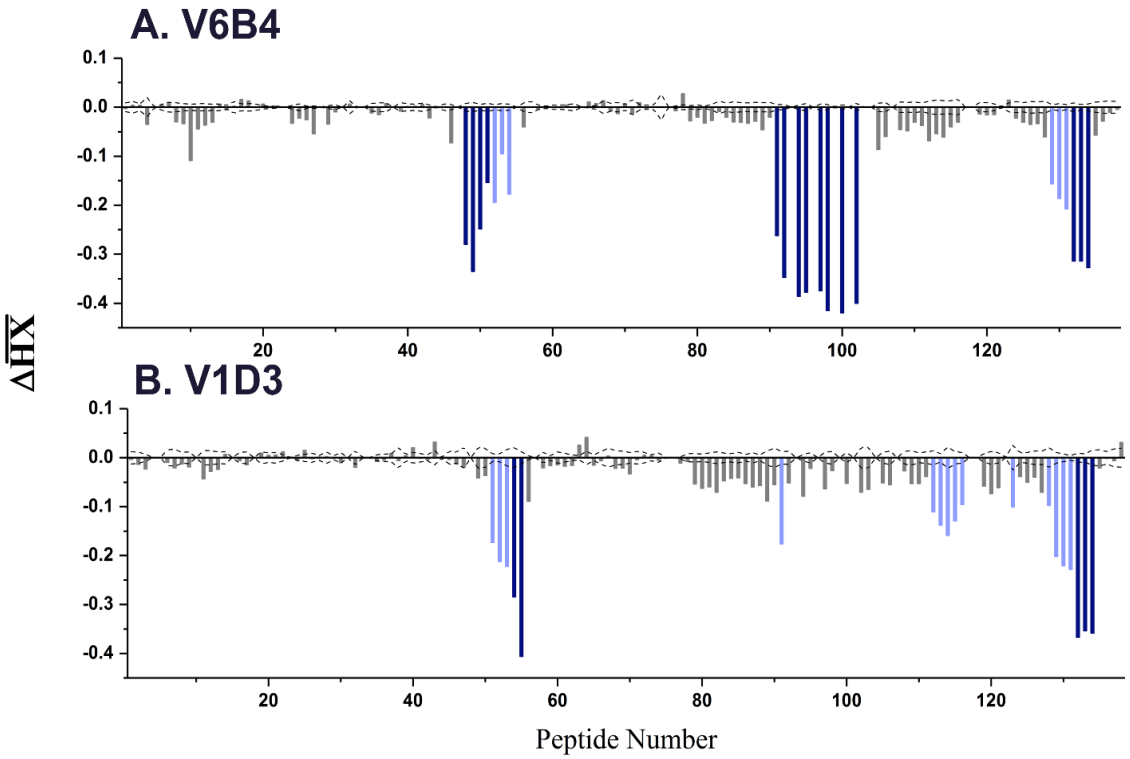

Figure 4. Relative levels of protection of RiVax peptides by V_HHs in 3.1. The $\Delta\overline{HX}$ values for each RiVax peptide are shown for V_HHs (a) V6B4 and (b) V1D3. The $\Delta\overline{HX}$ values are clustered using k-means clustering into three categories as follow: deep blue, strong protection; light blue; intermediate protection, and gray, insignificant. The dotted lines represent "3σ" confidence intervals for statistically significant changes in hydrogen exchange.

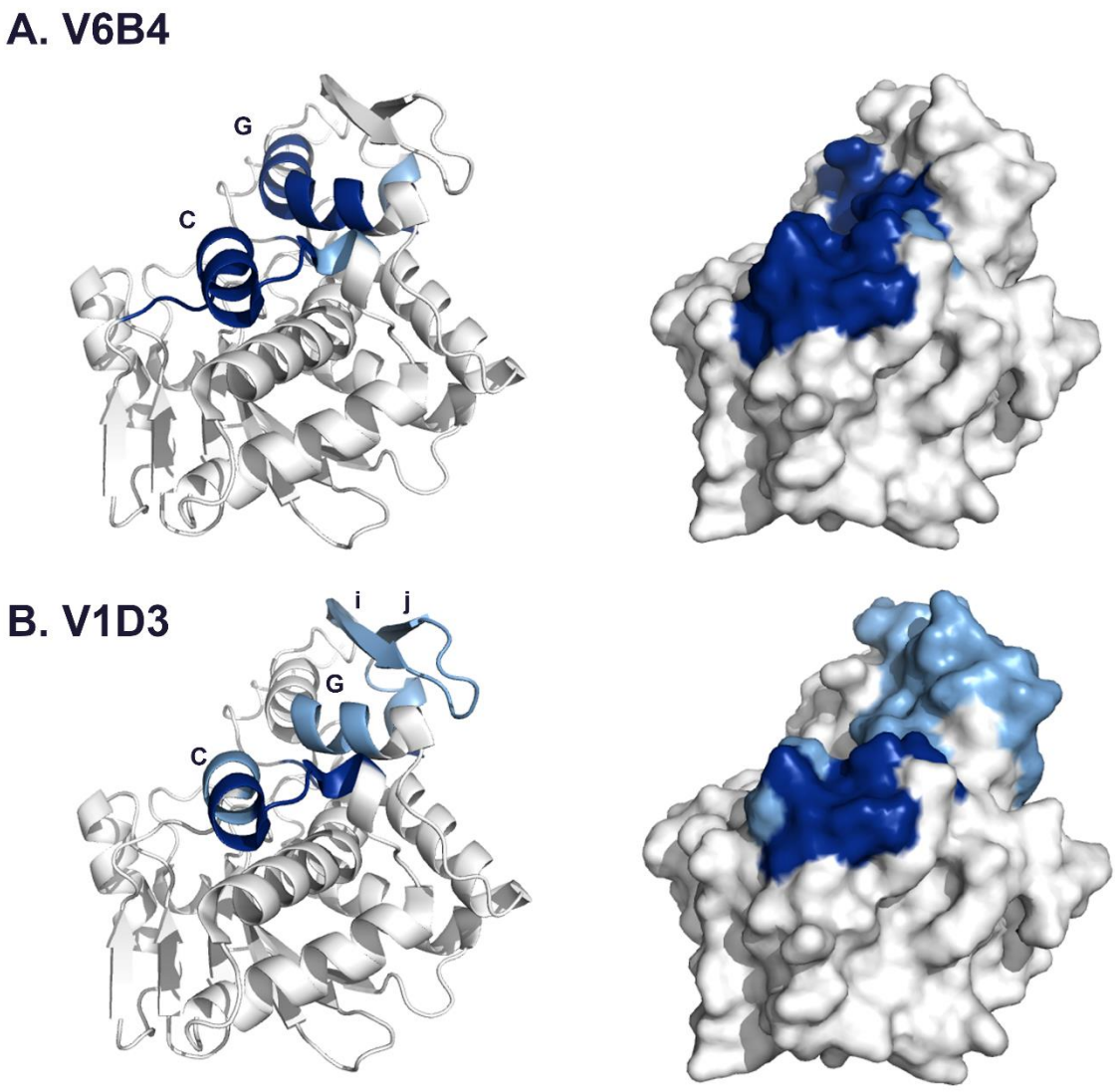

Figure 5. Epitope regions as identified by HX-MS are mapped onto the structure of RiVax. HX protection categories in figure 4 are shown mapped onto the crystal structure of RiVax for (a) V6B4 and (b) V1D3. The most relevant secondary structure elements helices C and G and C-terminus regions are labelled. Color coded as in Figure 1b.

Subcluster 3.2: A total of three V_HHs were grouped within sub-cluster 3.2 based on common HX-MS profile encompassing α-helices B, C and G **(Figures 6-7)**. For example, V6D8 strongly protected α-helices B (residues 92-107, peptides 35-39), C (residues 123-135, peptides 49-54), and G (residues 211-217, peptides 102), plus a short region near the C-terminus (residues 247-255, peptides 129-134). V6F12 likely derived from the same B-cell lineage as V6D8 (Table 1, Figure S1). Although the protection profiles of V6D8, V6F12, and V7H7 are similar, the magnitudes of protection in the three secondary structural features are distinct. V6D8 and V6F12 interacted primarily with α-helices B and C, and secondarily with α-helix G. V7H7, by contrast, primarily protects several overlapping peptides in α-helix G, and secondarily protects α-helices B and C (with the exception of one peptide in α-helix C). In all three cases (V6D8, V6F12, and V7H7), contact with α-helix B was corroborated by competitive binding assay with Cluster 1 mAbs PB10 and WECB2 (DJ Vance, J Tremblay, CB Shoemaker, NJ Mantis, *manuscript in preparation*). Given that α-helix B is a neutralizing "hotspot" on RTA (9, 10, 18, 20, 21), it is a little surprising that none of the V_HHs in this sub-cluster have any detectable TNA, especially in the case of V7H7, which has relatively strong affinity (K_d = 507 pM) for ricin.

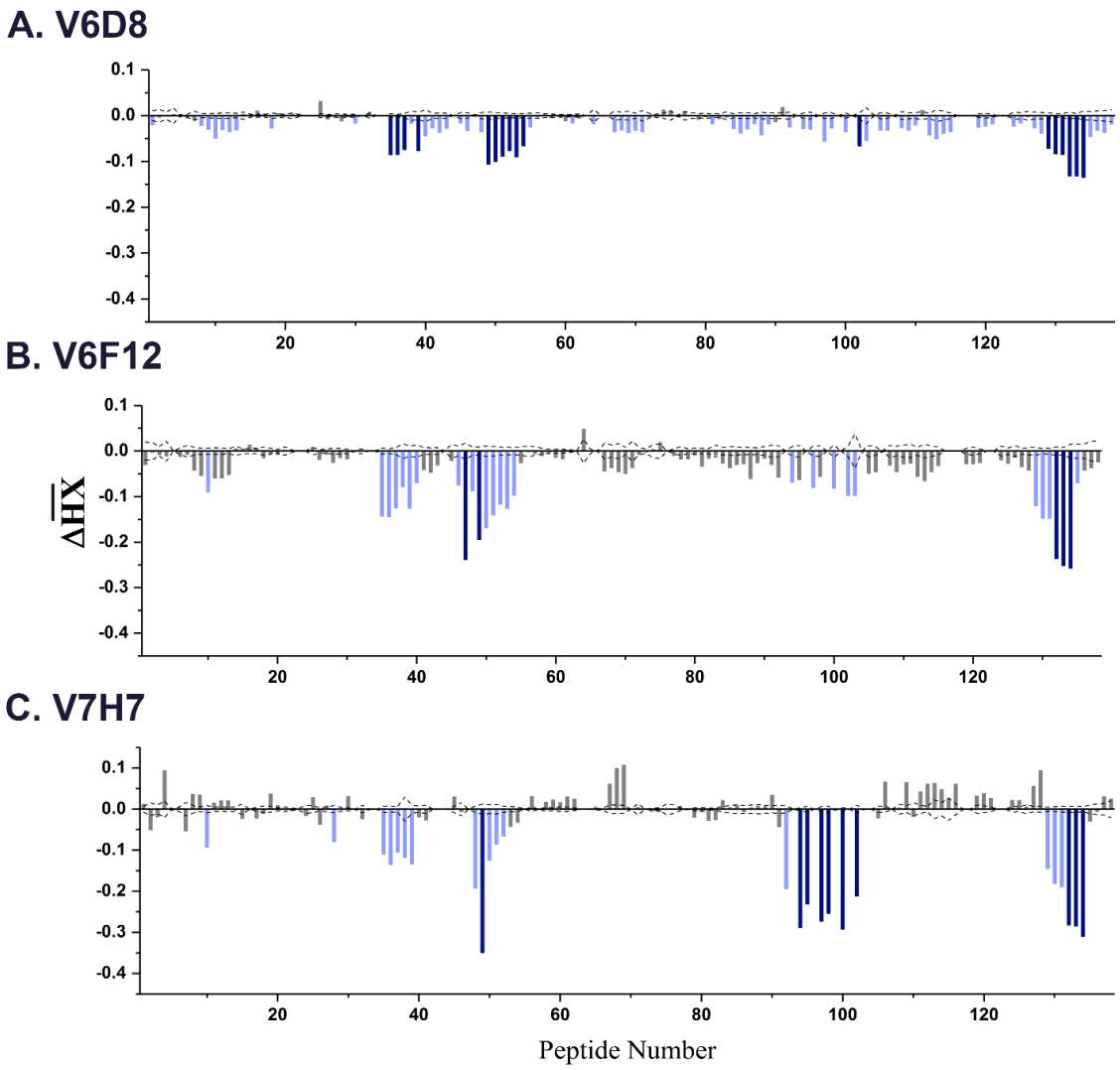

Figure 6. Relative levels of protection of RiVax peptides by VHHs that are classified into subcluster 2 within cluster 3 as defined by HX-MS. The $\Delta\overline{HX}$ values for each RiVax peptide are shown for VHHs (a) V6D8 (b) V6F12 and (c) V7H7. Color coded according to Figure 4.

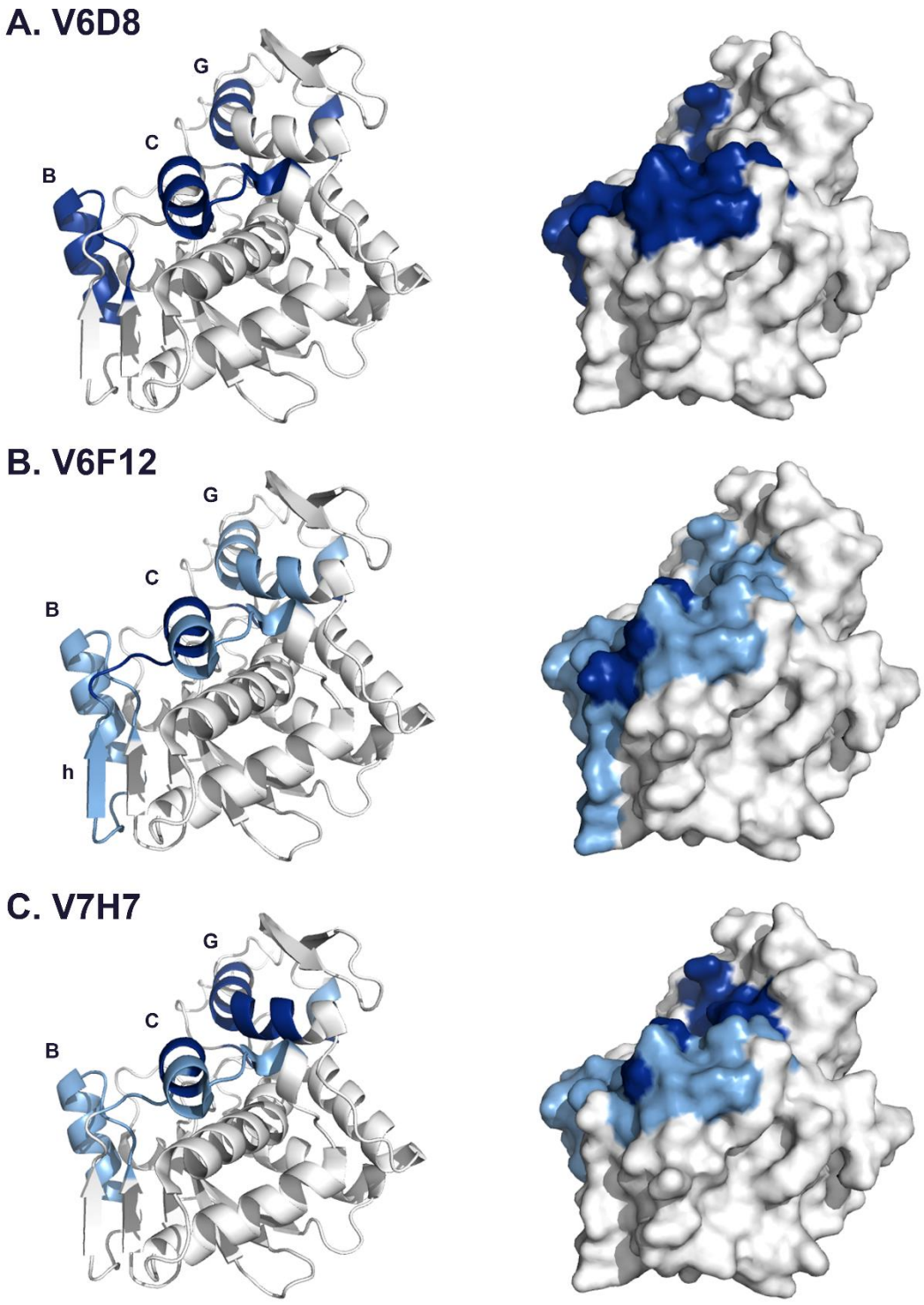

Figure 7. Visual presentation of epitope regions of V6D8, V6F12 and V7H7 on RTA*. HX protection categories in figure 6 are shown mapped onto the structure of RiVax for (a) V6D8 (b) V6F12 and (c) V7H7. Secondary structure elements including helices C and B as well as strand h and c-terminus regions are labelled. Intermediate protection by V6D8 is spread over much of RiVax's surface and the magnitudes of protection are low. Therefore, only strongly protected elements are mapped onto the crystal structure of RiVax.

Subcluster 3.3: The third sub-cluster is populated only by V6D4, which has weak toxin-neutralizing activity (IC_{50} ~200 nM). Interestingly, V6D4 appears to have arisen from the same B-cell lineage as V6B4 in subcluster 3.1(Table 1, Figure S1). HX-MS analysis demonstrated strong protection of α-helix G (peptide 102, residues 211-217) and intermediate protection of α-helix B (peptides 35-39, residues 92-107). V6D4 also protected short region in the C-terminus of RiVax **(Figure 8a and 8b)**. V6D4 did not protect α-helix C, which differentiates it from subclusters 3.1 and 3.2. We can only speculate that contact with α-helix B coupled with a higher affinity for ricin (K_d = 224 pM) is what accounts for V6D4's neutralizing activity.

Subcluster 3.4: The fourth sub-cluster is populated by JNM-A11. JNM-A11 strongly protects residues in α-helix C (peptides 49-51, residues 124-133), and also intermediately protects residues in the N-terminal region of α-helix E (peptides 70 and 71, residues 162-168) and β-strand h (peptides 45 and 46, residues 108-122) (**Figure 9a and 9b**). JNM-A11 is unique among the cluster 3 V_HHs in that it does not protect α-helix G, possibly because of a different angle of approach compared to the other V_HHs. The HX-MS protection profile is consistent with competition data: JNM-A11 is competed by Cluster I mAbs PB10 and WECB2 and also by the Cluster I-II overlap mAb SWB1 (17). JNM-A11 does not neutralize ricin, despite a very strong binding affinity (K_d = 200 pM). Since JNM-A11 appears to almost exclusively target α-helix C, we would infer that contact with α-helix C alone is not sufficient to affect ricin function. By extension, neutralization of ricin by the sub-cluster 1 V_HH V1D3, which targets α-helices C and G, is therefore likely mediated via contact with α-helix G.

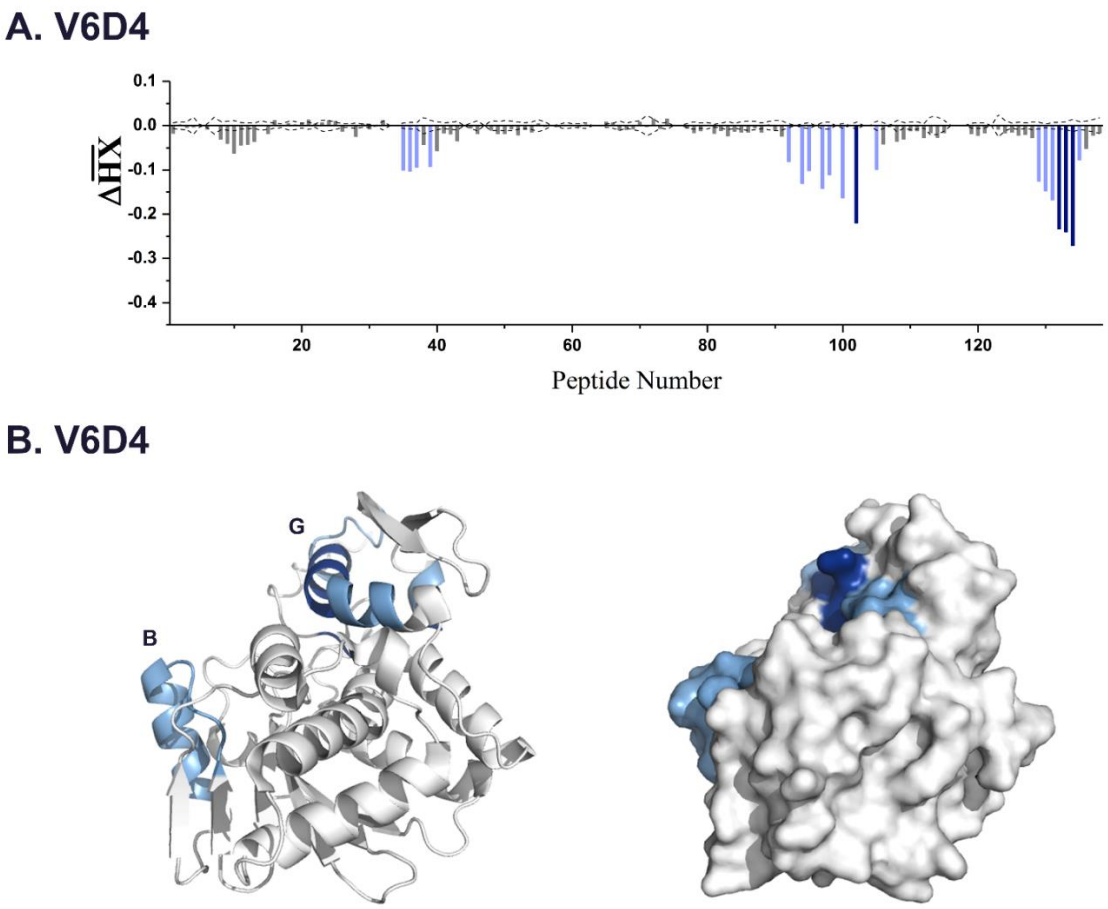

Figure 8. Location of the epitope of V6D4 on RiVax. (a) Relative levels of protection of RiVax peptides by V6D4 as defined by HX-MS. The image is color coded according to figure 1b. (b) The HX protection categories, as shown in panel b, are mapped onto the crystal structure of RiVax Secondary structures including helices B and G are labelled.

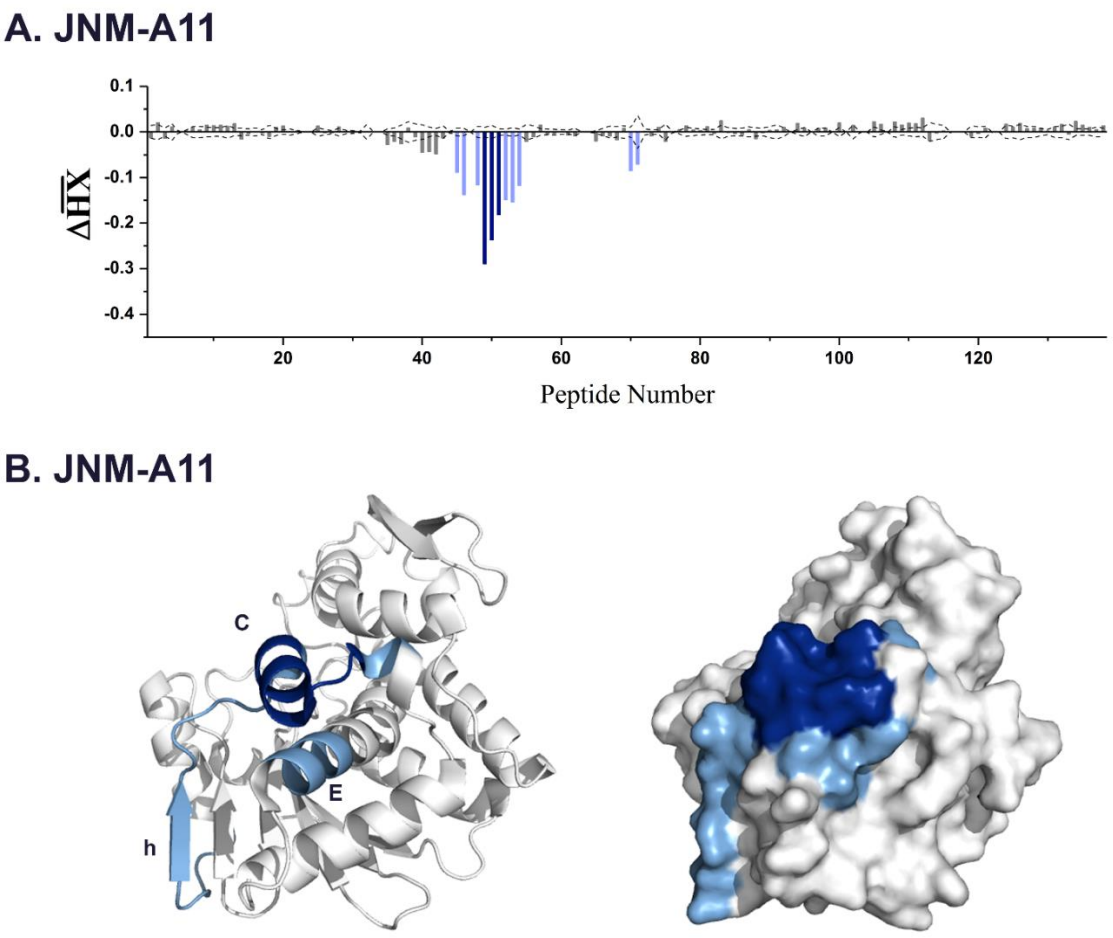

Figure 9. Relative levels of protection of RiVax peptides by JNM-A11 that is categorized into subcluster 4 within cluster 3 as defined by HX-MS. (a) $\Delta\overline{HX}$ values for each RiVax peptide are shown for VHH, JNM-A11. The delta HX values are color coded as in Figure 4. (b) The HX protection categories are mapped onto the crystal structure of RiVax

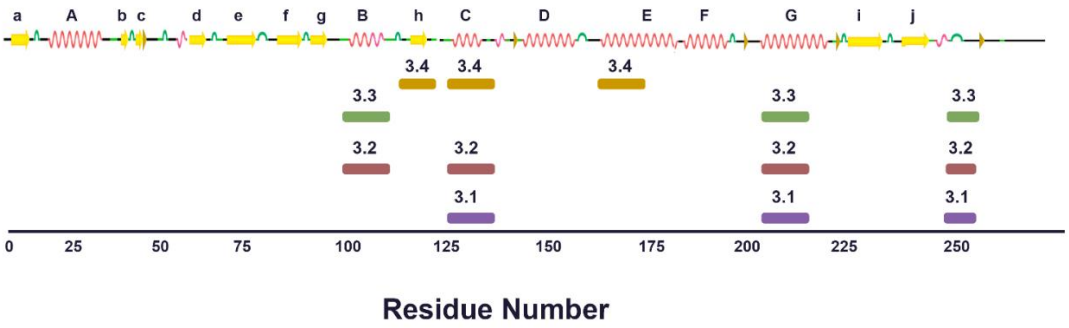

Figure 10. Summary of epitopes within cluster III as identified by HX-MS. The colored rectangle bars denote epitopes for subclusters 3.1-3.4. Regions protected by V_HHs in various subclusters are shown in linear representation of the primary sequence of RiVax, aligned with a cartoon secondary structure. Arrows denote β secondary structure and coils indicate helices.

Conclusions and perspectives

Our analysis concludes that helix G is critical in TNA as both toxin neutralizing V_HHs, V1D3 and V6D4 epitopes constitute helix G. At this point we are not entirely sure about the roles of helices C and G in toxin neutralizing capacity. For example, mAb IB2, a strong neutralizer makes strong contact with helix C than G. Similarly one of the two neutralizing VHHs, V1D3 (subcluster 3.1), also showed strong binding in helix C than G. In contrast, V6D4 (subcluster 3.3), does not make any contact with helix C yet it shows neutralizing capacity. Also, a lot of VHHs we analyzed in this report fell in subcluster 3.1, involving interaction with C and G. The fact that all these VHHs being as non-neutralizers didn't help in understanding what role helix C plays. We believe that helix C acts as a docking station while interaction with neighboring helix G being critical. Ultimately, it could probably be the differences in the angle of contact with the helices C and G that could explain the TNA. Also, there could be single amino acid residue contacts that could be critical for TNA. Unfortunately, HX-MS would not be able to pick these single residue contacts as the deuterium uptake differences in those regions would be minimal such that it is tough to

predict whether those differences are a result of allosteric effects or real effects (due to binding). We believe solving crystal structures would give deeper insights including understanding the roles of helices C and G in TNA, critical single amino acid residue contacts and the angle of contact. Towards this end, we started to crystallize antibody-antigen complexes to better understand the cluster 3 region on the surface of RTA. For example, we successfully co-crystallized V1D3 with toxin and it binds to cluster 3 as revealed by X-ray crystallography (*manuscript in prep*).

While subcluster 3.3, which includes neutralizing antibody, V6D4, involves interaction with helix B in addition to helix G and could explain for its TNA as helix B is recognized by a number of neutralizing antibodies which are characterized in our previous reports. The subcluster 3.4, JNM-A11 involves interaction with helix C but has no contact with helix G. JNM-A11, the strongest binder (K_d = 200 pM) of all cluster III V_HHs we have studied in this report happens to be a non-neutralizer implying that helix G is important in TNA. In fact, JNM-A11 binds to helix C and N-terminus helix E and strand h implies its binding orientation is unique from the rest of the subclusters. To further substantiate that, it is the only antibody in our collection that doesn't shown any protection in the C–terminus region of RiVax. In the case of JNM-A11, the binding region and C–terminus residues are located exactly on the opposite sides of RiVax.

It should be mentioned that all the V_HHs reported here (with an exception of subcluster 3.4, JNM-a11) have shown strong protection in C–terminal residues (249-255) of RiVax. This region is located in the bottom side of RTA which associates with RTB in the context of the holotoxin and hence is not surface exposed. Thus, the strong protection seen in this region is probably due to allosteric effect.

Another noteworthy feature to mention is that none of the subcluster 3.2 antibodies which recognize helix B has TNA. While the binding affinities of V6D8 and V6F12 are in the nanomolar

range, on the other hand, V7H7 showed a sub nanomolar binding affinity value (K_d =507pM) comparable to the 460 pM dissociation constant of the neutralizing sub-cluster 1 V_HH, V1D3. That said, other neutralizing V_HHs that target α-helix B, such as F5 and E5 have even higher affinities of 19 and 190 pM, respectively (10, 18, 22), so perhaps higher affinity than even 507 pM is required to neutralize via α-helix B. The differential protection profiles could be a consequence of different angles of approach such that V6D8/V6F12 anchor themselves on α-helices B and C, while V7H7 targets α-helix G.

Materials and methods:

RTA^* purification: RTA^* was expressed and purified as described in (23). Briefly, the gene encoding RTA^* was cloned into the pTBSG expression vector which has an N-terminal 6-His affinity tag. Plasmid DNA was transformed into the chemically competent *E. coli* cells BL21 (DE3)-pRARE. Protein expression was induced by addition of isopropyl B-D-1-thiogalactopyranoside (IPTG). The His-tag RTA^* was then purified using a His-select high flow Ni^{+2} affinity gel, followed by overnight digestion with a His-tagged TEV protease to cleave the N-terminal His-tag of RTA^*. The His–tag cleaved RTA^* was then purified from the flow-through of a second round of immobilized Ni^{+2} ion chromatography.

HX-MS: HX-MS experiments for epitope mapping were conducted as described previously (24). Briefly, a LEAP H/DX PAL robotic system was used for sample preparation, mixing and injection. For the free RTA^*, 4 µl of 20 µM RTA^* stock solution was incubated with 36 µl of deuterated buffer (10 mM sodium phosphate, 150 mM sodium chloride, pD 7.4). For the bound states, the stock solution had a final concentration of 20 µM RTA^* and 40 µM V_HH resulting in 1:2 molar ratio of RTA^*:V_HH. Four µl of the stock was incubated with 36 µl of deuterated buffer. Samples were incubated at 25^oC for five HX times between 13 s and 24 h and subsequently quenched using

200 mM phosphate-4 M guanidine hydrochloride solution (pH 2.5) held at 0°C. The quenched samples were then injected onto an immobilized pepsin column where proteolysis occurs overlapping peptides from RTA*. The peptides were desalted using a C18 trap and are separated using a segmented gradient with water/acetonitrile/0.1% formic acid on a C18 column (Zorbax 300SB-C18 2.1 × 50 mm, 1.8 μm particle diameter, Agilent, Santa Clara, CA). The entire LC system (immobilized pepsin column, C18 trap and a C18 RP-UHPLC column) was kept in a refrigerated cabinet that is maintained at 0°C to minimize back exchange. Nevertheless, the first two residues in a peptide generally undergo rapid back exchange (25). RTA* peptides are analyzed by an Agilent 6530 series QTOF mass analyzer for their increase in mass i.e. for deuterium uptake.

Data Analysis

The HX-MS data processing was carried out using HDExaminer (Sierra Analytics, CA). A total of 138 peptides (see supplementary table 2) that cover the entire sequence of RTA* were analyzed. For each peptide, the magnitude of protection from each HX time was averaged and normalized to its peptide length to obtain a ΔHX value, $\Delta HX = HX_{bound} - HX_{bound}$, as described previously (26). The propagated standard error in delta HX was estimated as described in (26). The magnitudes of delta HX values of overlapping peptides that span the entire RiVax are then classified using K-means clustering into three categories and were colored as follows: strong protection, intermediate protection, no significant protection. For visualization, the HX-MS results were mapped onto the crystal structure of RTA*(PDB: 3SRP) (7) using PyMoL (The PyMOL Molecular Graphics System; Schrodinger LLC, San Diego, CA). For better visualization purpose, only overlapping peptides that fall in strong and intermediate protection category are colored.

References:

1. Stirpe F. Ribosome-inactivating proteins. Toxicon. 2004;44(4):371-83.
2. Montfort W, Villafranca JE, Monzingo AF, Ernst SR, Katzin B, Rutenber E, et al. The three-dimensional structure of ricin at 2.8 A. The Journal of biological chemistry. 1987;262(11):5398-403.
3. Rutenber E, Katzin BJ, Ernst S, Collins EJ, Mlsna D, Ready MP, et al. Crystallographic refinement of ricin to 2.5 A. Proteins. 1991;10(3):240-50.
4. Endo Y, Mitsui K, Motizuki M, Tsurugi K. The mechanism of action of ricin and related toxic lectins on eukaryotic ribosomes. The site and the characteristics of the modification in 28 S ribosomal RNA caused by the toxins. The Journal of biological chemistry. 1987;262(12):5908-12.
5. Endo Y, Tsurugi K. RNA N-glycosidase activity of ricin A-chain. Mechanism of action of the toxic lectin ricin on eukaryotic ribosomes. The Journal of biological chemistry. 1987;262(17):8128-30.
6. Rutenber E, Ready M, Robertus JD. Structure and evolution of ricin B chain. Nature. 1987;326(6113):624-6.
7. Legler PM, Brey RN, Smallshaw JE, Vitetta ES, Millard CB. Structure of RiVax: a recombinant ricin vaccine. Acta crystallographica Section D, Biological crystallography. 2011;67(Pt 9):826-30.
8. O'Hara JM, Kasten-Jolly JC, Reynolds CE, Mantis NJ. Localization of non-linear neutralizing B cell epitopes on ricin toxin's enzymatic subunit (RTA). Immunology letters. 2014;158(1-2):7-13.
9. O'Hara JM, Neal LM, McCarthy EA, Kasten-Jolly JA, Brey RN, 3rd, Mantis NJ. Folding domains within the ricin toxin A subunit as targets of protective antibodies. Vaccine. 2010;28(43):7035-46.
10. Rudolph MJ, Vance DJ, Cheung J, Franklin MC, Burshteyn F, Cassidy MS, et al. Crystal structures of ricin toxin's enzymatic subunit (RTA) in complex with neutralizing and non-neutralizing single-chain antibodies. Journal of molecular biology. 2014;426(17):3057-68.
11. Toth Rt, Angalakurthi SK, Van Slyke G, Vance DJ, Hickey JM, Joshi SB, et al. High-Definition Mapping of Four Spatially Distinct Neutralizing Epitope Clusters on RiVax, a Candidate Ricin Toxin Subunit Vaccine. Clinical and vaccine immunology : CVI. 2017.
12. Yermakova A, Klokk TI, O'Hara JM, Cole R, Sandvig K, Mantis NJ. Neutralizing Monoclonal Antibodies against Disparate Epitopes on Ricin Toxin's Enzymatic Subunit Interfere with Intracellular Toxin Transport. Scientific reports. 2016;6:22721.
13. O'Hara JM, Mantis NJ. Neutralizing monoclonal antibodies against ricin's enzymatic subunit interfere with protein disulfide isomerase-mediated reduction of ricin holotoxin in vitro. Journal of immunological methods. 2013;395(1-2):71-8.
14. Chen E, Salinas ND, Huang Y, Ntumngia F, Plasencia MD, Gross ML, et al. Broadly neutralizing epitopes in the Plasmodium vivax vaccine candidate Duffy Binding Protein. Proceedings of the National Academy of Sciences of the United States of America. 2016;113(22):6277-82.
15. Gribenko AV, Parris K, Mosyak L, Li S, Handke L, Hawkins JC, et al. High Resolution Mapping of Bactericidal Monoclonal Antibody Binding Epitopes on Staphylococcus aureus Antigen MntC. PLoS pathogens. 2016;12(9):e1005908.
16. Malito E, Faleri A, Lo Surdo P, Veggi D, Maruggi G, Grassi E, et al. Defining a protective epitope on factor H binding protein, a key meningococcal virulence factor and vaccine antigen. Proceedings of the National Academy of Sciences of the United States of America. 2013;110(9):3304-9.
17. Vance DJ, Tremblay JM, Rong Y, Angalakurthi SK, Volkin DB, Middaugh CR, et al. High-Resolution Epitope Positioning of a Large Collection of Neutralizing and Non-Neutralizing Single Domain Antibodies on Ricin Toxin's Enzymatic and Binding Subunits. Clinical and vaccine immunology : CVI. 2017.

18. Rudolph MJ, Vance DJ, Cassidy MS, Rong Y, Shoemaker CB, Mantis NJ. Structural analysis of nested neutralizing and non-neutralizing B cell epitopes on ricin toxin's enzymatic subunit. Proteins. 2016;84(8):1162-72.
19. Bazzoli A, Vance DJ, Rudolph MJ, Rong Y, Angalakurthi SK, Toth RTt, et al. Using homology modeling to interrogate binding affinity in neutralization of ricin toxin by a family of single domain antibodies. Proteins. 2017.
20. Vance DJ, Mantis NJ. Resolution of two overlapping neutralizing B cell epitopes within a solvent exposed, immunodominant alpha-helix in ricin toxin's enzymatic subunit. Toxicon : official journal of the International Society on Toxinology. 2012;60(5):874-7.
21. Zhu Y, Dai J, Zhang T, Li X, Fang P, Wang H, et al. Structural insights into the neutralization mechanism of monoclonal antibody 6C2 against ricin. The Journal of biological chemistry. 2013;288(35):25165-72.
22. Vance DJ, Tremblay JM, Mantis NJ, Shoemaker CB. Stepwise engineering of heterodimeric single domain camelid VHH antibodies that passively protect mice from ricin toxin. The Journal of biological chemistry. 2013;288(51):36538-47.
23. Thomas JC, O'Hara JM, Hu L, Gao FP, Joshi SB, Volkin DB, et al. Effect of single-point mutations on the stability and immunogenicity of a recombinant ricin A chain subunit vaccine antigen. Human vaccines & immunotherapeutics. 2013;9(4):744-52.
24. Toth RTt, Angalakurthi SK, Van Slyke G, Vance DJ, Hickey JM, Joshi SB, et al. High-Definition Mapping of Four Spatially Distinct Neutralizing Epitope Clusters on RiVax, a Candidate Ricin Toxin Subunit Vaccine. Clinical and vaccine immunology : CVI. 2017;24(12).
25. Bai Y, Milne JS, Mayne L, Englander SW. Primary structure effects on peptide group hydrogen exchange. Proteins. 1993;17(1):75-86.
26. Bazzoli A, Vance DJ, Rudolph MJ, Rong Y, Angalakurthi SK, Toth RTt, et al. Using homology modeling to interrogate binding affinity in neutralization of ricin toxin by a family of single domain antibodies. Proteins. 2017;85(11):1994-2008.

SUPPLEMENTARY TABLES

Supplementary Table 1. Summary of HX-MS analysis of fourteen V_HHs bound to RiVax

Table 3. RiVax peptides, residues, and secondary structures protected by Cluster 3 V_HHs.				
		Strong and Intermediate Protected Elements [a]		
V_HH	**Subcluster**	**Peptides**	**Residues**	**Secondary Structure(s)**
V1B11	3.1	49-54	123-135	α-helix C
		94-102	205-217	α-helix G
		132-134	249-255	
JNM-D1		55	130-135	α-helix C
		50-54	123-135	α-helix C
		91	205-210	α-helix G
V2A11		49	123-126	α-helix C
		50-53	123-135	α-helix C
		92-103	205-217	α-helix G
		106-116	218-243	β-strands i, j
		132-134	249-255	
V6H8		48-52, 54	119-135	α-helix C
		94,95,97,98,100,102	205-217	α-helix G
		132-134	249-254	
V6A6		48-52, 54	119-135	α-helix C
		91-102	205-217	α-helix G
		130-134	247-255	
V6A7		49	123-126	N-term α-helix C
		48, 50-52, 54	119-135	α-helix C
		92-100	205-217	α-helix G
		132-134	247-255	
V6G10		49	123-136	N-term α-helix C
		48,50-52,54	119-135	α-helix C
		92-100	205-217	α-helix G
		132-134	247-255	

V8C7		49	123-126	N-term α-helix C
		48, 50-54	119-135	α -helix C
		91-102	205-217	α-helix G
		132-134	249-255	
V8E6		49	123-126	α-helix C
		47, 50-55	119-135	α -helix C
		92-103	205-217	α-helix G
		129-134	247-255	
V1G6		50-54	123-135	α-helix C
		94,97-98,100,102	205-217	α-helix G
		109-111	218-232	β-strand i
		112-113, 115	226-240	β-strands i, j
		132-134	249-255	
V2G10		47, 50-54	118-135	α-helix C
		55	130-135	C-term α-helix C
		92-103	205-217	α-helix G
		111-113	221-240	β-strands i, j
		132-134	249-255	
V5A2		49-53	123-135	α-helix C
		54,55	127-135	α-helix C
		91	205-210	α-helix G
		114	227-240	β-strands i, j
		112-113,115-116,119	226-243	β-strands i, j
		132-134	249-255	
JIV-F6		54	127-135	α-helix C
		51-53	123-133	α-helix C
		91	205-210	α-helix G
		113-115	226-240	β-strands i, j
		129-131	249-255	
V1B10		54	127-135	α-helix C
		51-53	123-133	α -helix C
		91	205-210	α-helix G
		113,115,116	226-243	β-strands i, j
		132-134	249-255	
[a], Peptides and corresponding residues on RiVax are indicated in supplementary Table S2				

Supplementary Table 2. RTA* peptic peptides

	Amino acid residue #			Amino acid residue #			Amino acid residue #			Amino acid residue #	
Pep #	start	end	Pep #	start	end	Pep #	start	end	Pep #	start	end
1	0	11	**36**	92	103	**71**	162	168	**106**	217	232
2	12	20	**37**	92	107	**72**	165	168	**107**	217	240
3	12	24	**38**	93	99	**73**	165	171	**108**	218	225
4	21	24	**39**	93	107	**74**	168	171	**109**	218	232
5	25	32	**40**	102	107	**75**	169	173	**110**	220	232
6	25	37	**41**	103	107	**76**	172	181	**111**	221	232
7	28	37	**42**	104	107	**77**	175	181	**112**	226	232
8	33	59	**43**	104	109	**78**	178	181	**113**	226	240
9	37	59	**44**	108	117	**79**	182	186	**114**	227	240
10	38	45	**45**	108	118	**80**	182	187	**115**	232	240
11	38	55	**46**	108	122	**81**	182	188	**116**	232	243
12	38	57	**47**	118	122	**82**	182	190	**117**	232	248
13	38	59	**48**	119	126	**83**	182	204	**118**	233	243
14	56	59	**49**	123	126	**84**	187	204	**119**	233	244
15	58	61	**50**	123	129	**85**	188	204	**120**	233	246
16	58	68	**51**	123	133	**86**	189	204	**121**	233	248
17	60	68	**52**	123	135	**87**	189	206	**122**	240	243
18	60	69	**53**	127	133	**88**	191	204	**123**	241	244
19	62	68	**54**	127	135	**89**	191	207	**124**	241	246
20	69	72	**55**	130	135	**90**	195	204	**125**	241	248
21	69	73	**56**	130	151	**91**	205	210	**126**	243	248
22	69	74	**57**	133	144	**92**	205	214	**127**	244	248
23	70	74	**58**	134	146	**93**	205	216	**128**	245	248
24	72	79	**59**	134	151	**94**	205	217	**129**	247	253
25	72	91	**60**	136	146	**95**	207	214	**130**	247	254
26	73	79	**61**	136	147	**96**	207	216	**131**	247	255
27	73	91	**62**	136	151	**97**	207	217	**132**	249	253
28	75	79	**63**	146	150	**98**	208	214	**133**	249	254
29	75	91	**64**	147	150	**99**	208	216	**134**	249	255
30	80	91	**65**	147	151	**100**	208	217	**135**	255	267
31	80	92	**66**	148	151	**101**	211	216	**136**	256	267
32	84	91	**67**	152	161	**102**	211	217	**137**	257	267
33	92	99	**68**	152	164	**103**	212	216	**138**	258	267
34	92	101	**69**	153	164	**104**	217	220			
35	92	102	**70**	162	167	**105**	217	225			

SUPPLEMENTARY FIGURES

Family Alignments

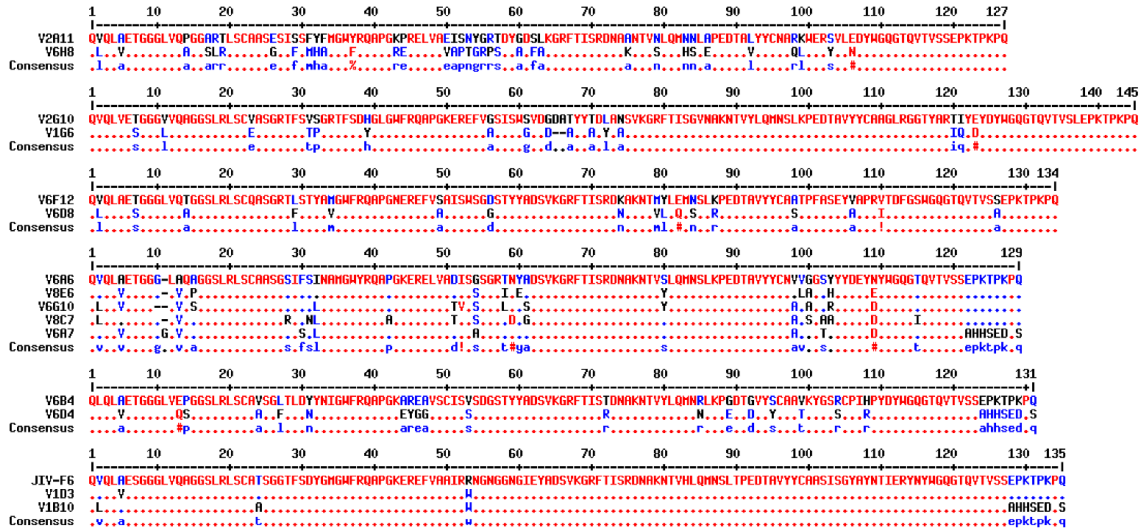

Supplementary figure 1.

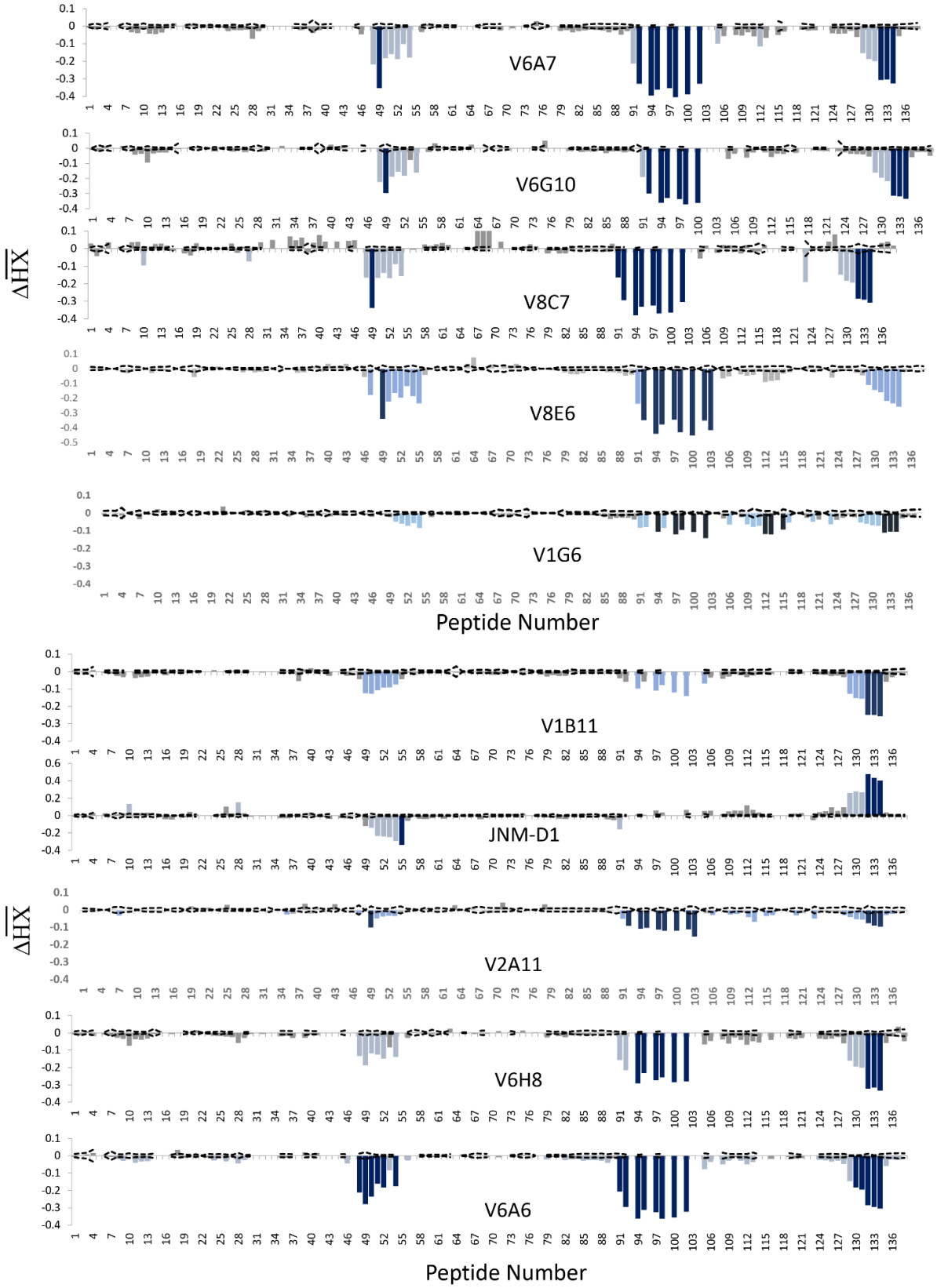
V6A7
V6G10
V8C7
V8E6
V1G6
V1B11
JNM-D1
V2A11
V6H8
V6A6
ΔHX
Peptide Number

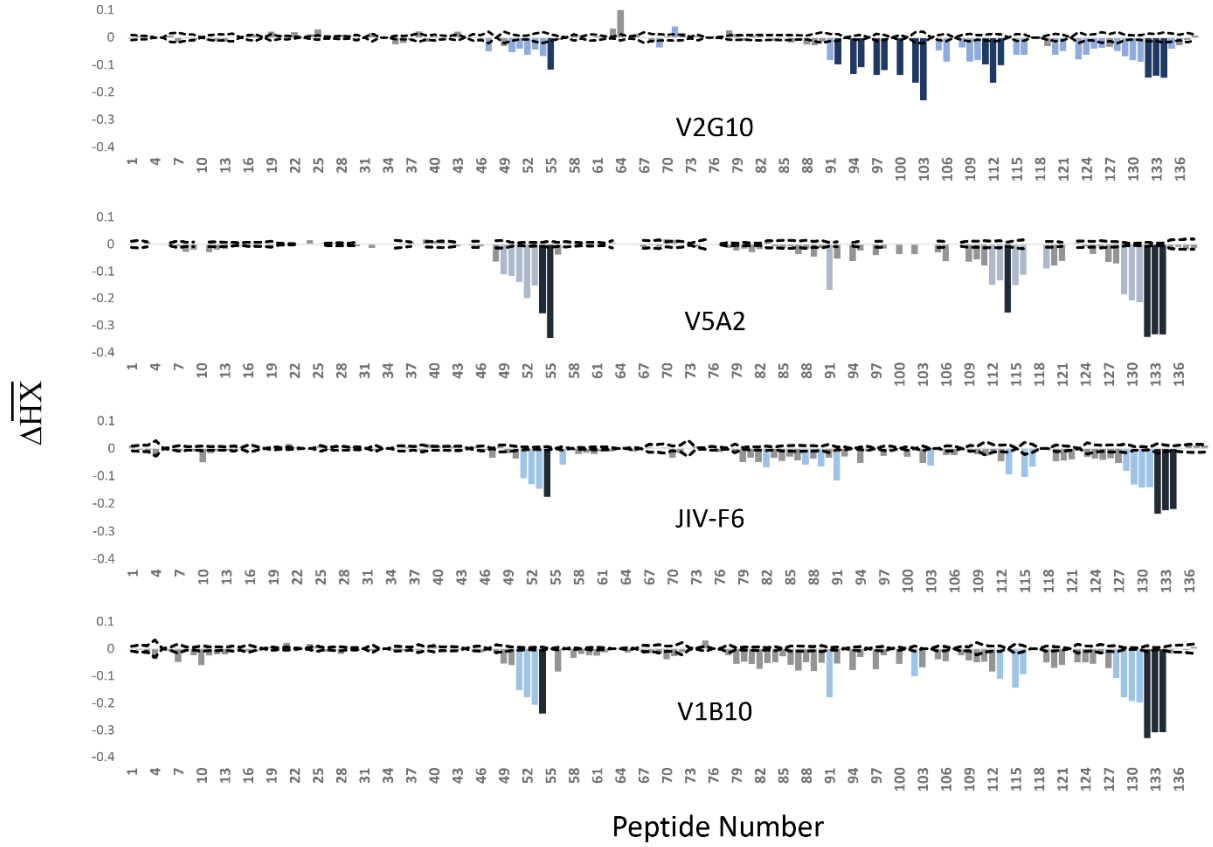

Supplementary figure 2. Relative levels of protection of RiVax peptides by Subcluster 3.1 V_HHs as defined by HX-MS

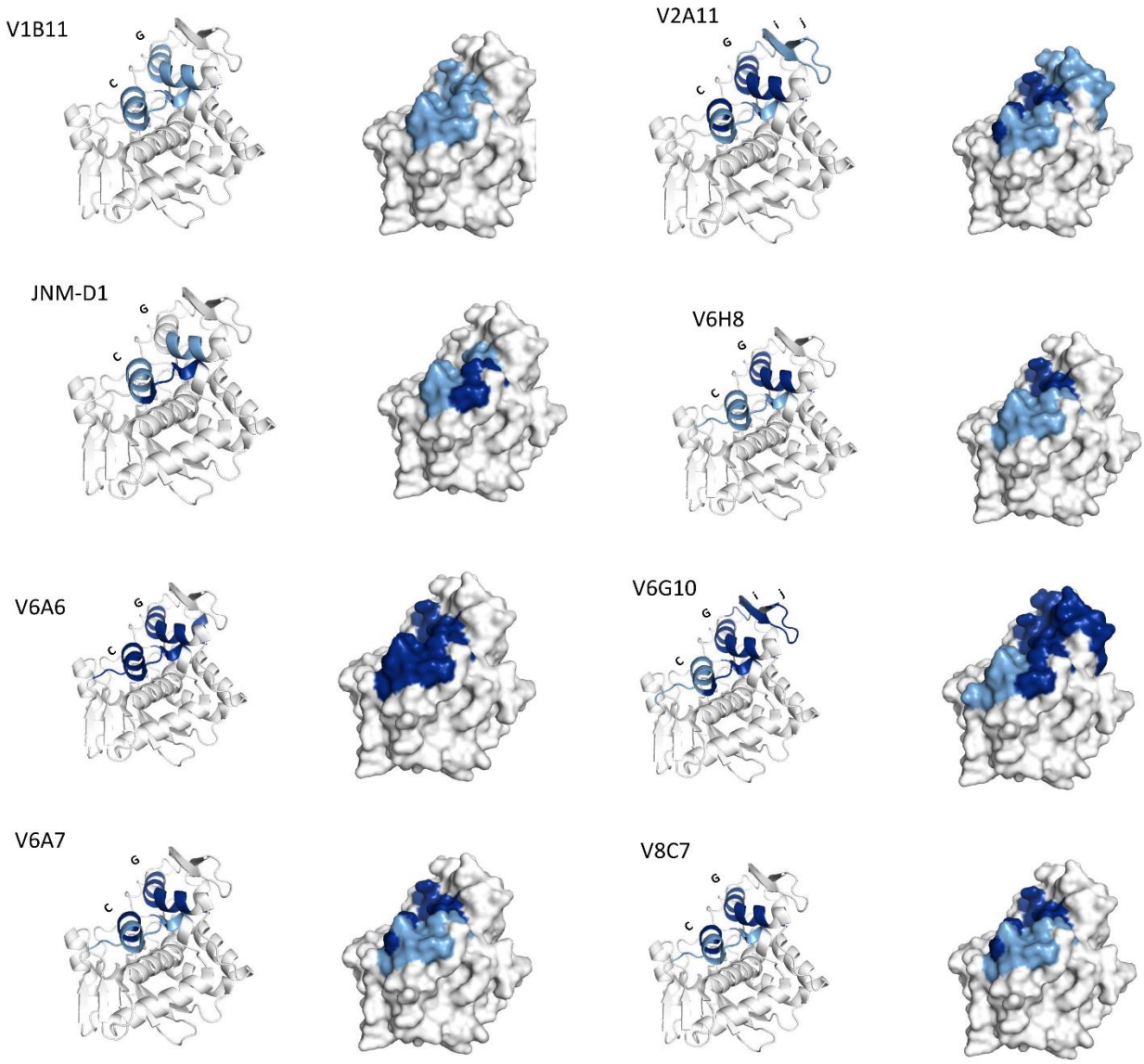
V1B11
V2A11
JNM-D1
V6H8
V6A6
V6G10
V6A7
V8C7

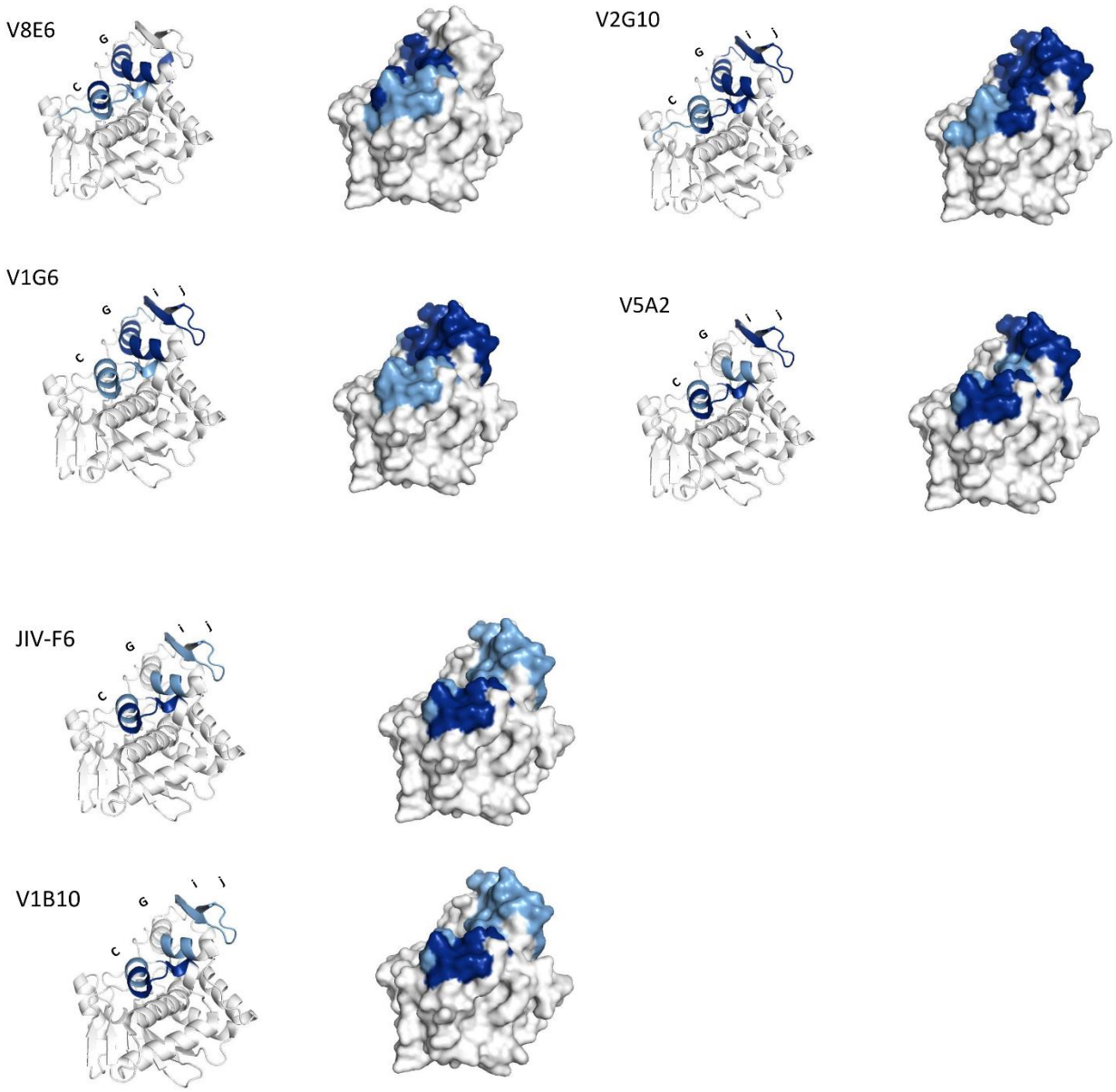

Supplementary figure 3. Visual representation of epitopes of subcluster 3.1 V_HHs on RiVax

CHAPTER 3

Investigating the Dynamics and Polyanion Binding Sites of Fibroblast Growth Factor-1 Using Hydrogen-Deuterium Exchange Mass Spectrometry

Introduction:

The fibroblast growth factors (FGFs) are a family of structurally and functionally conserved protein ligands that regulate a plethora of developmental processes including mitogenesis, angiogenesis, homeostasis and metabolism (1). These growth factors signal by associating with a specific tyrosine kinase receptor (FGFR) and heparin sulfate proteoglycans (HSPG) to form a ternary complex on the cell surface (2). HSPG aids in the formation of the ternary signal transduction complex by linking FGF-1 ligands into a dimer/oligomer that bridges two FGFR chains (3, 4). Among the FGF family, FGF-1 is unique in that it can stimulate all FGFRs and is consequently a broad specificity human mitogen (5, 6). For the same reason, FGF-1 is termed the "universal FGFR ligand" and the molecular basis for its broad specificity is attributed to its plasticity in the N terminus region (7).

FGF-1 is a member of the β-trefoil family of proteins, characterized by pseudo-threefold rotational (i.e. C_3) symmetry (8, 9) (Figure 1). The overall structure is described by three repeating "trefoil-fold" structural motifs. These motifs are each approximately 42 amino acids in length (with some variation in length between the three motifs). Each motif contains four β-strands: two β-strands of each motif contribute to the overall six-stranded β-barrel architecture, and two β-strands of each motif comprise a β-hairpin. These latter three β-hairpins form a triangular arrangement that pack against the bottom of the β-barrel. The general organization of the primary and secondary structure is shown in (Figure 2**)**. The x-ray crystal structure of FGF-1 has been reported and includes a 2.0Å resolution structure of the mature 140 amino acid form (crystallizing in space group $P2_1$; PDB accession 2AFG)(10), as well as 1.65Å and 1.10Å resolution structures of an N-

terminal 6xHis-tagged form (both crystallizing in space group $C222_1$; PDB accession 1JQZ and 1RG8, respectively) (11, 12). In the non-His-tagged form, the initial N-terminal nine amino acids are not visible in the electron density; whereas, in the His-tagged form there are crystal packing interactions between molecules that structure the N-terminus. In neither crystal form are C-terminal residues 138-140 visible in the electron density. The binding sites of heparin sulfate (HS) on FGF-1 as indicated by crystallographic studies reveals that a high negative charge density HS interacts with positively charged amino acids in the N-terminus (residue 18) and C- terminus region (residues 112-128) of FGF-1 (3, 13). The binding affinity of FGF-1 for HS diminishes significantly on deleting the residues at positions 120-122 on FGF-1 while simultaneously increasing its thermal stability, leading to a function\stability trade off (14).

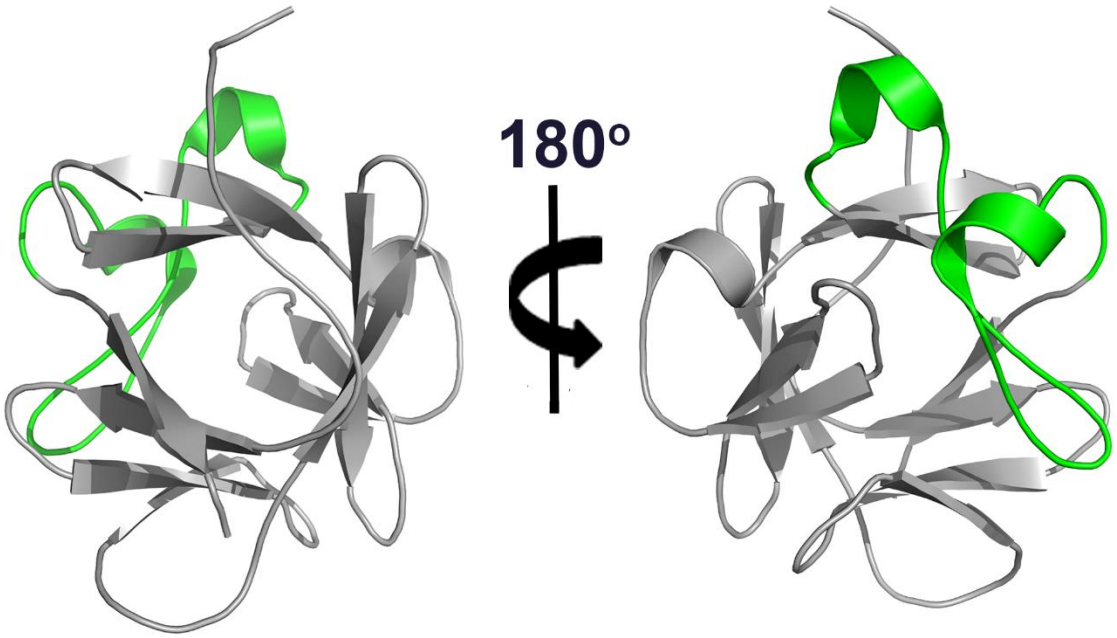

Figure 1. Ribbon diagram view of FGF-1 (PDB ID: 1JQZ) oriented parallel to the C_3 axis of the rotational symmetry. The green shaded portion indicates the region that is rich in basic amino acids. Right panel is rotated 180° along the y-axis

Studies have also suggested that FGF-1 exhibits a *foldability-function trade off* (15). φ- value analysis has shown that, of the three repeated subdomains, the second half of the first trefoil fold subdomain and most of the second one participate in the folding transition state, essentially forming a core nucleus during protein folding. In contrast, the third trefoil fold subdomain contributes little to the folding transition state (i.e., it folds later in the folding pathway) while possessing a rich set of diverse functionalities including HS affinity.

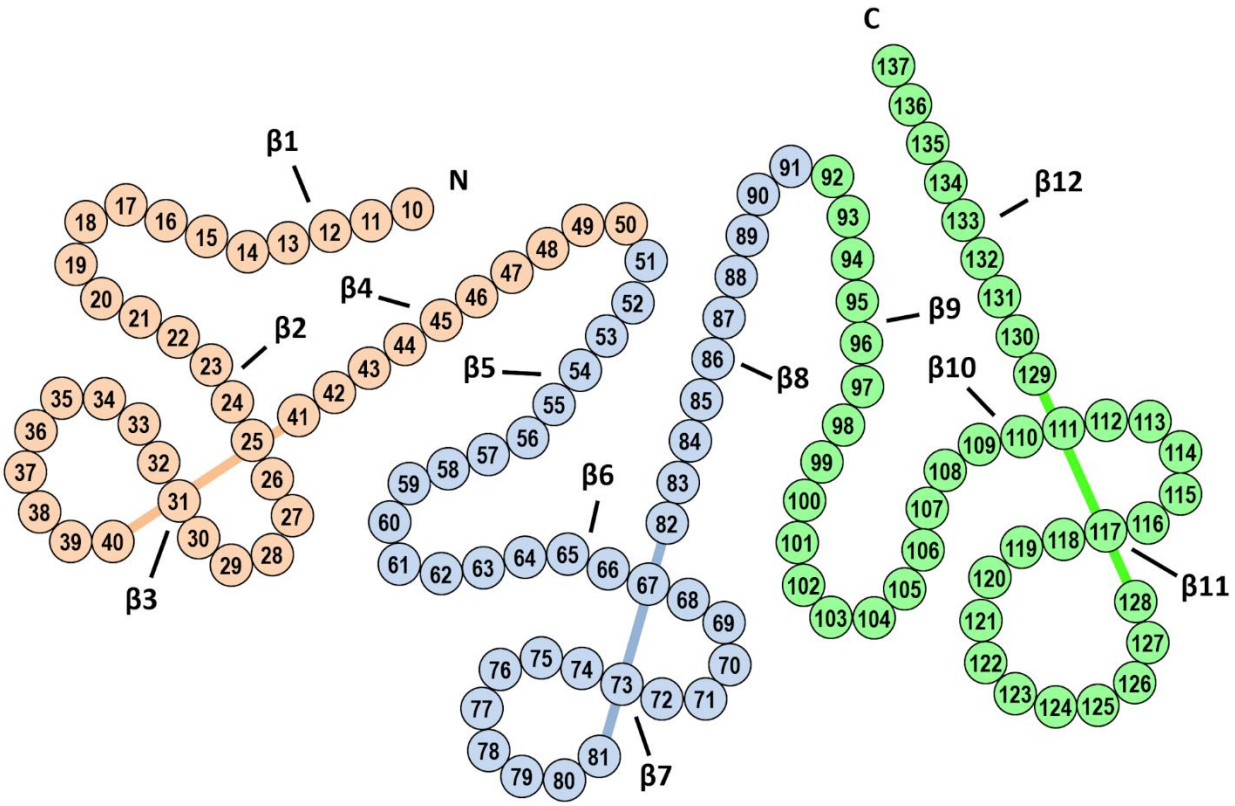

Figure 2. Organization of the primary structure of FGF-1 illustrating the three repeating "trefoil-fold" motifs. Mature FGF-1 is 140 amino acids; residue positions 10-137 are consistently structured in difference crystal forms of the protein. The 12 β-strands of the overall architecture are identified, as are the N- and C-termini. The coloring identifies the three repeating trefoil-fold motifs.

Although Crystal structures of FGF-1 in complex with heparin and other polyanions have been solved and clearly identify the binding regions of HS on FGF-1, this approach provides only limited information about the structural dynamics of FGF-1 in solution although crystal

temperature factors do provide some indirect information. NMR studies have shown that there is an overall decrease in flexibility of FGF-1 (with the exception of a few residues) upon binding by heparin analogues (16, 17).

Hydrogen-deuterium exchange coupled with mass spectrometry (HX-MS) has the capability of monitoring the back bone dynamics of a protein molecule. Proteins upon incubation in D_2O solvent exchange their labile hydrogens with deuterium. The hydroxyl, amine and carboxyl of the amino acid residue side chains exchange rapidly and revert back to hydrogen upon exposure to H_2O during an LC separation. Unlike the side chain hydrogens, many of the amide protons exchange slowly. The differential rates observed provide a measure of the dynamic exposure of different regions of the backbone except for proline which doesn't possess an amide hydrogen. Regions that are more flexible (e.g. loops, turns) exchange rapidly compared to regions that are more rigid (α-helix and β-sheets). A major strength of hydrogen exchange studies lies in its ability to compare two states of a protein (e.g. in the absence and presence of a ligand).

Several studies have been performed using HX-MS to investigate the effects of salts, particular compounds, antimicrobial agents and aggregation on the conformational dynamics of proteins including monoclonal antibodies (18-21). Using HX-MS, we have previously reported the location of the binding sites of numerous antibodies including monoclonal and single domain antibodies (V_HHs) on a ricin toxin subunit vaccine antigen RTA^*(22-24). Here, we use HX-MS to investigate the dynamics of FGF-1 as well as the binding sites of various polyanions including two different forms of heparin and phosphate-containing compounds including ATP and phytic acid.

Studies have shown that heparin consisting of at least four monosaccharide units is necessary to stabilize FGF-1 from thermal unfolding (25). In addition to this observation, a broad variety of anionic species including phosphorylated compounds have been found to bind and stabilize FGF-

1 in vitro (25, 26). It has been established by crystal structures (PDB accession 1E0O) that heparin binds primarily to the C-terminal region of FGF-1. It has also been shown that this heparin binding region folds after crossing the barrier during protein folding which provides a basis for a foldability and functional trade off in FGF-1 (15).

Using HX-MS, along with identifying the binding sites of various polyanions on FGF-1, we also examine the dynamics of FGF-1 alone at the peptide level which is in turn narrowed down to a residue level using redundant peptides that contains overlapping residues. This is compared to the B-factors of the main chain amides from solved FGF-1 crystal structures. Although crystallographic B–factors are derived from the protein in a solid state, they can be expected to reflect internal steric factors and have some relationship to solution protein dynamics. Approximately half of the main chain amides of FGF-1 are in solvent inaccessible environments. The location of solvent excluded main chain amides, and their associated hydrogen-bonding main chain carbonyl partner, are shown in Figure 3. In HX experiments, it is generally this set of solvent excluded main chain amides that can potentially be protected from rapid exchange. Rapid HX among this set of solvent excluded main chain amides indicates unimpeded solvent penetration which should be afforded by comparatively high structural flexibility at such positions.

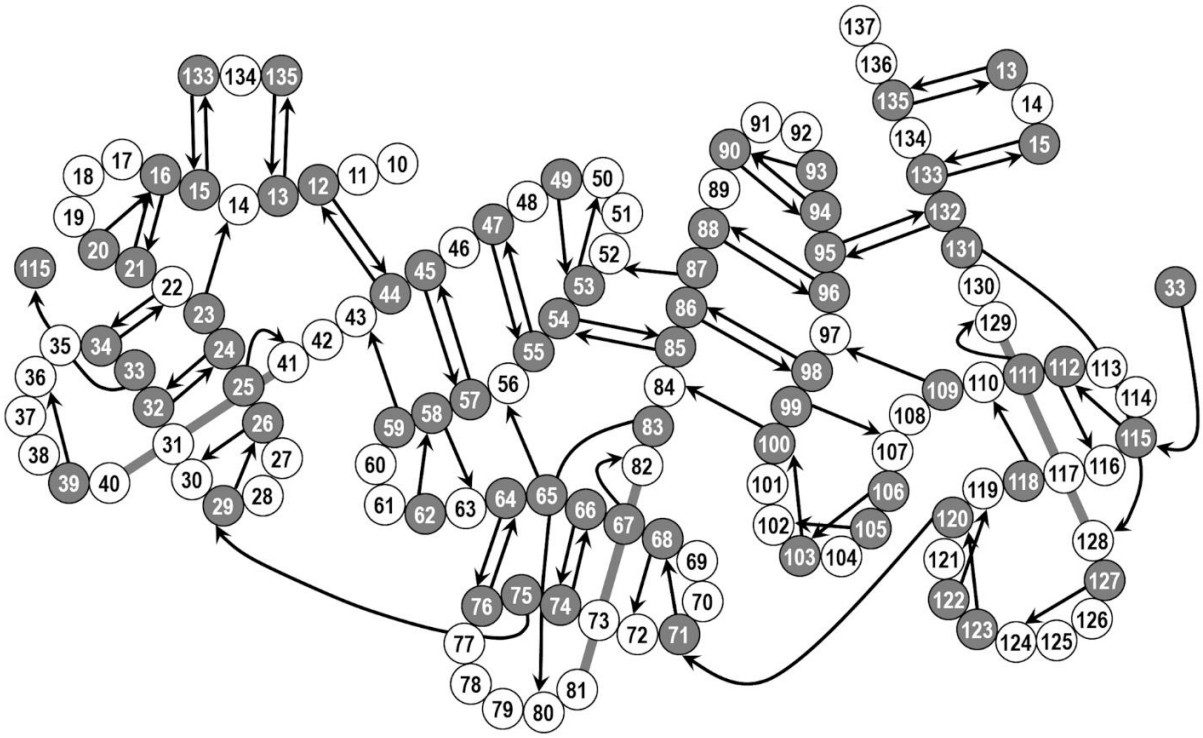

Figure 3. Solvent-excluded main chain amides (Gray) in FGF-1 as determined from the X-ray crystal structure (gray background, white font). The arrows indicate the hydrogen-bonding partner (with arrow head indicating a main chain carbonyl acceptor).

Materials and Methods:

Materials: LC-MS grade water, acetonitrile and 0.1% formic acid in water were obtained from Fisher Scientific (Fair Lawn, NJ). Deuterium oxide (99+%D) was purchased from Aldrich. The anhydrous form of sodium phosphate dibasic and sodium phosphate monobasic monohydrate were obtained from Research Products International (Mt Prospect, IL). Heparin (Average MW: 13.5kDa - 15kDa) was purchased from Calbiochem. Low MW heparin (Average MW: 5.5kDa - 6.5kDa) and ATP were obtained from Sigma-Aldrich. Phytic acid sodium salt hydrate was purchased from Sigma.

Expression and purification of His-tag FGF: N-terminus His tag FGF-1 was expressed and purified as previously described in (11). An extinction coefficient of E_{280nm} (0.1%, 1 cm) = 1.26 was used for concentration determination.

Hydrogen exchange mass spectrometry: For the unliganded state, the stock solution of FGF-1 was diluted to 0.58mg/mL using 6mM phosphate buffer containing 150mM NaCl at pH 7.4. For the polyanion bound state, the stock solutions of FGF-1 and polyanion (Heparin and Low MW heparin) are diluted to 0.58 mg/L and 0.116 mg/mL (1:0.2 by weight of FGF-1) respectively. In the case of phytic acid and ATP, the FGF-1 and ligand were diluted to 0.58mg/L and 1.16mg/mL (1:2 by weight) respectively. In terms of molar ratios, for phytic acid and ATP bound states the protein was at a [FGF-1]/polyanion molar ratio of 0.02 and 0.015, respectively. For heparin and low MW heparin bound states, the [FGF-1]/polyanion molar ratio are 4 and 2 respectively since increased concentration of those polymers inhibited FGF-1 ionization confounding mass spectrometry analysis. HX-MS experiments were performed using a QTOF mass analyzer (Agilent 6530, Santa Clara, CA) with a three pump LC system (Agilent 1260, Santa Clara, CA). An H/DX PAL robot (LEAP Technologies, Carrboro, North Carolina) was used for sample handling, preparation and injection. To initiate the HX process, 4µL of protein stock was diluted at a 1:10 ratio with 36 µL of labeling buffer (6 mM sodium phosphate containing 150 mM NaCl at pD 7.3) containing either no polyanion (free state) or with polyanion (bound state) prepared in deuterium oxide. The reaction mixture was then incubated at 15^{o}C for six time periods of 13, 100, 1000, 10000, 30000 and 86400 s prepared in triplicate. Thirty µL of the labeled reaction mixture was then transferred and mixed with 30µL of quench buffer (4 M Gdn-HCl, 0.2 M sodium phosphate, pH 2.5) at 0 °C for 60 s to stop the exchange process. Fifty five uL of the quenched sample was then injected into the 100 µL sample loop of a refrigerated column compartment connected to an

Agilent 1260 infinity series LC, in-house built immobilized pepsin column, a peptide desalting trap, and a C18 column (Zorbax 300SB-C18 2.1 × 50 mm, 1.8 μm particle diameter, Agilent, Santa Clara, CA). The temperature of the column compartment was maintained at 1°C to minimize the extent of back exchange. Peptides were eluted using an LC method that was described previously (22). To minimize the peptide carry over in the immobilized pepsin column from previous runs, the pepsin column was washed between each HX run using a procedure described previously (27). The extent of deuteration in each peptide was measured using a Q-TOF mass spectrometer, equipped with a standard electrospray ionization source operated in positive mode. Collision induced dissociation and MS/MS analysis were used to generate a peptide map of FGF that covered 100% of the FGF sequence with 90 peptides. The peptides are numbered sequentially from the N-terminus to the C-terminus (see Supplementary Table S1).

Data analysis: HD Examiner 2.1 software (Sierra Analytics, Modesto, CA) was used to analyze the HX data. For backbone flexibility, we quantified the fraction of exchange after 13s (the shortest time point possible with our system) as described previously (18). For mapping the binding site, the deuterium uptake of the peptides at each time point was exported from HD Examiner. For each peptide, information from all time points was combined into a single $\Delta\overline{\mathrm{HX}}$ value representing the average difference in deuterium uptake between bound and free states, normalized for peptide length as indicated in equation 1(24),

$$\Delta\overline{\mathrm{HX}} = \frac{\sum_{i=1}^{n_{\mathrm{HX}}}(\bar{m}_{a,i}-\bar{m}_{b,i})}{n_{\mathrm{HX}}D_{\max}} \qquad (1)$$

where n_{HX} is the number of HX labeling times, D_{max} is the theoretical maximum deuteration, $\bar{m}_{a,i}$ is the average mass of the peptide in the bound state at the ith HX timepoint, and $\bar{m}_{b,i}$ is the average mass of the peptide in the free state at the ith HX timepoint. For each peptide, D_{max} was considered to be the total number of residues in the peptide minus the number of proline residues and the first

two N-terminal residues. The absolute $\Delta\overline{HX}$ values of all the peptides were then pooled and an algorithm employing K means clustering was run to classify the data set into two clusters. We then used the following classification system to define protection sites on FGF-1. Cluster one peptides that have strong negative $\Delta\overline{HX}$ values are defined as strongly protected sites on FGF, while cluster two as weak and non-significant. The strong protection category reflects polyanion binding, while intermediate/insignificant protection is considered to reflect allosteric effects and structural changes. Overlapping residues that fall in both strong and weak protection classifications were considered strongly protected. The standard error in $\Delta\overline{HX}$ was then considered to be as indicated in equation 2 below, an analysis based on propagation of the standard error in triplicate measurements through the $\Delta\overline{HX}$ calculations. To set the confidence interval, we have taken a "3σ" confidence interval ($\pm 3 \times \varepsilon_{\Delta\overline{HX}}$).We used the following coloring system with the crystal structure of FGF-1. Strong protection is colored dark blue and weak/non-significant as gray.

$$\varepsilon_{\Delta HX} = \frac{\sqrt{\sum_{i=1}^{n_{HX}} \left[\left(\frac{s_{a,i}}{\sqrt{n_{rep}}} \right)^2 + \left(\frac{s_{b,i}}{\sqrt{n_{rep}}} \right)^2 \right]}}{n_{HX} D_{max}} \qquad (2)$$

where ($n_{rep} = 3$) triplicate data, $s_{a,i}$ *and* $s_{b,i}$ *are* standard deviation of replicates, *s in* state *a* and state *b* respectively at the ith time point, n_{HX} is the number of HX labeling times and D_{max} is the theoretical maximum deuteration.

Heat map for the change in HX of FGF-1 alone for buried amide positions: This study characterizes a series of 90 peptides generated by a pepsin digest of FGF-1 after HX. The set of 90 peptides spans the entire FGF-1 primary structure; however, assigning HX protection to specific amino acid positions is not straightforward since individual peptides span multiple amino acid positions, and individual amino acid positions can be included in more than one peptide. It should be possible, however, to generate position-specific data by alignment of the 90 peptides to the

primary structure and then averaging the values for the set of peptides that span specific amino acid positions. Supplementary Fig 1 shows how this calculation is performed for the data in Fig. 4A. The peptides are color coded by a "heat map" that indicates their experimentally-derived %HX. This heat map is calculated so that BLUE indicates the lowest observed HX and RED the greatest. As an example of the residue position calculation, peptides 11-16 overlap the position of Thr34; thus, the %HX for this position is the average value for this set of peptides (or 19.0%). For FGF-1 the resulting average %HX values for each buried amide position span a low of 4% (e.g. Phe132) and a high of 55.8% (Ser47). For heat map coloring purposes to communicate these results, this range of values is normalized to span a Blue (4%) to Red (55.8%) scale. Due to the primary amine conversion at the first position of a peptide, and a corresponding influence upon HX for the second position (28), the first two positions of each peptide are "greyed-out" in supplementary Figure 1 - indicating that no HX information is available at these positions. Thus, the %HX cannot be assigned for a small number (e.g. positions 23, 24, 74, 75, and 118) of the total set of buried amides; however, for all other buried amide positions an average %HX can be assigned (along with a corresponding heat map color).

Heat map for the change in hydrogen exchange of FGF-1 for buried amide positions in the presence of heparin: Figure 10 shows how this calculation is performed for the data in Figure 8A. This heat map is calculated such that BLUE indicates an increase in HX protection and RED no change. As an example of the residue position calculation, peptides 11-16 overlap the position of Thr34; thus, the $\Delta\overline{HX}$ for this position is the average value for this set of peptides (or -0.109). For FGF-1 in the bound state with heparin, the resulting average $\Delta\overline{HX}$ values for each buried amide position span a low of -0.242 (e.g. Lys112) and a high of -0.015 (Cys83). For heat map coloring purposes this range of values is normalized to span a Blue (-0.242) to Red (-0.015) scale. The heat

map for buried amide positions in the presence of other polyanions including Phytic acid, ATP and Low MW heparin was calculated similarly (supplementary Figure 3, 4 and 5 respectively).

B-Factor Analysis: A non-His-tagged form of FGF-1 crystallized in the $P2_1$ space group with four independent molecules in the asymmetric unit (2.0Å resolution)(10). An N-terminal 6xHis-tagged form of FGF-1 crystallized in the $C222_1$ space group with two independent molecules in the asymmetric unit (1.65Å resolution) (11). Isotropic B-factors were refined in both crystal forms and residue positions 10-137 were ordered in all structures. The average Cα B-factors for positions 10-137 for the six independent FGF-1 structures were calculated and are shown in supplementary Figure 2. Crystallographic B-factors are interpreted as indicating the motion or local mobility of the individual atoms (larger values indicating greater mobility). Isotropic B-factors reflect a model describing simple centrosymmetric vibrational motion (appropriate for 1.65-2.00Å resolution data).

Results:

Backbone flexibility of FGF-1 without polyanion ligation: With the aim of using HX-MS to locate the contact regions of various polyanions on FGF-1, we first established the backbone flexibility of FGF-1 itself. HX was performed on FGF-1 for 13s and quenched before being subjected to pepsin digestion and MS analysis as described in materials and methods. Using K-means clustering, backbone flexibility values are then classified into three categories: flexible, intermediate and rigid. Flexible and rigid regions of FGF-1 are shown in Figure 4A. The peptides are numbered sequentially from N to C terminus in all figures unless otherwise specified (Table 1). The flexible and rigid regions are spread throughout the protein sequence. Flexible regions are seen in strands 4, 5 and 7 as well as in turns 4, 5 and 7. These are all located on one side of the protein. Another substantial flexible region includes C-terminal strand 12. Rigid regions include

strands 2, 3 and 6 as well as turns 2, 3 and 6. Other significant rigid regions include C-terminus strands 8, 9 and 10 and turns 8 and 9 which are the putative binding sites for heparin. For better visualization and a more accurate representation, only overlapping peptide segments in the flexible category (Figure 4A) are colored yellow in the crystal structure of FGF-1 (Figure 4 B) and only rigid peptides (Figure 4A) that do not overlap with flexible category peptides are colored blue. In addition, the flexibility of buried amide positions was also investigated and compared with the B –factors as determined by crystallography. The %HX value for buried amides (heat map color) was calculated as described in the methods section and was assigned to a secondary structure representation of FGF-1 (Figure 5).

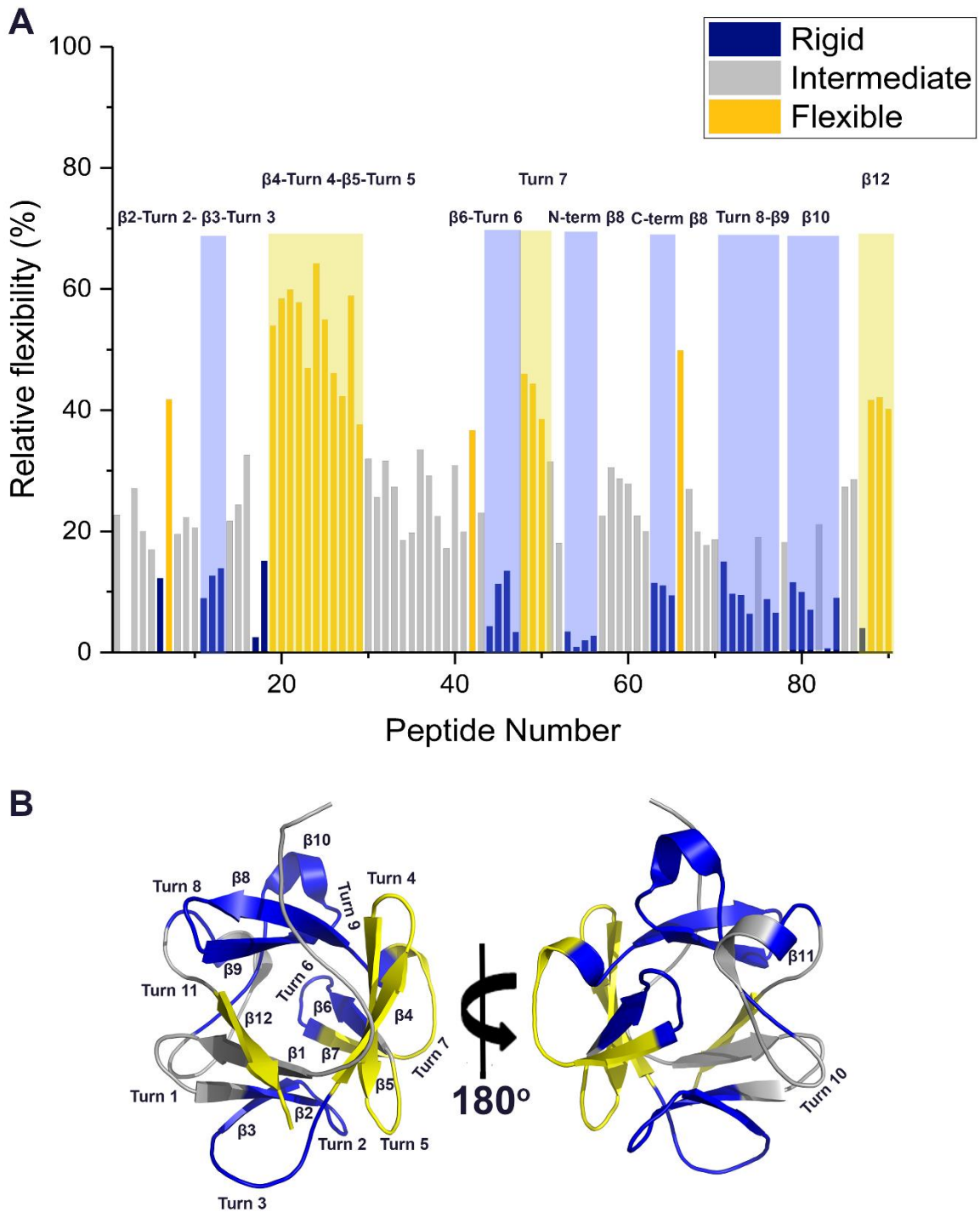

Figure 4. Relative flexibility of FGF-1, as measured by HX-MS; (A) Flexibility, as measured form the ratio of the extent of deuteration at 13s relative to theoretical maximal exchange without correction for back exchange. Dark blue indicate rigid, yellow indicates flexible and grey indicates intermediate dynamics. Flexible (top) and rigid (bottom) regions are assigned (B) The flexibility categories are mapped onto the structure of FGF-1. All the strands (noted as β) and turns of FGF-1 are assigned.

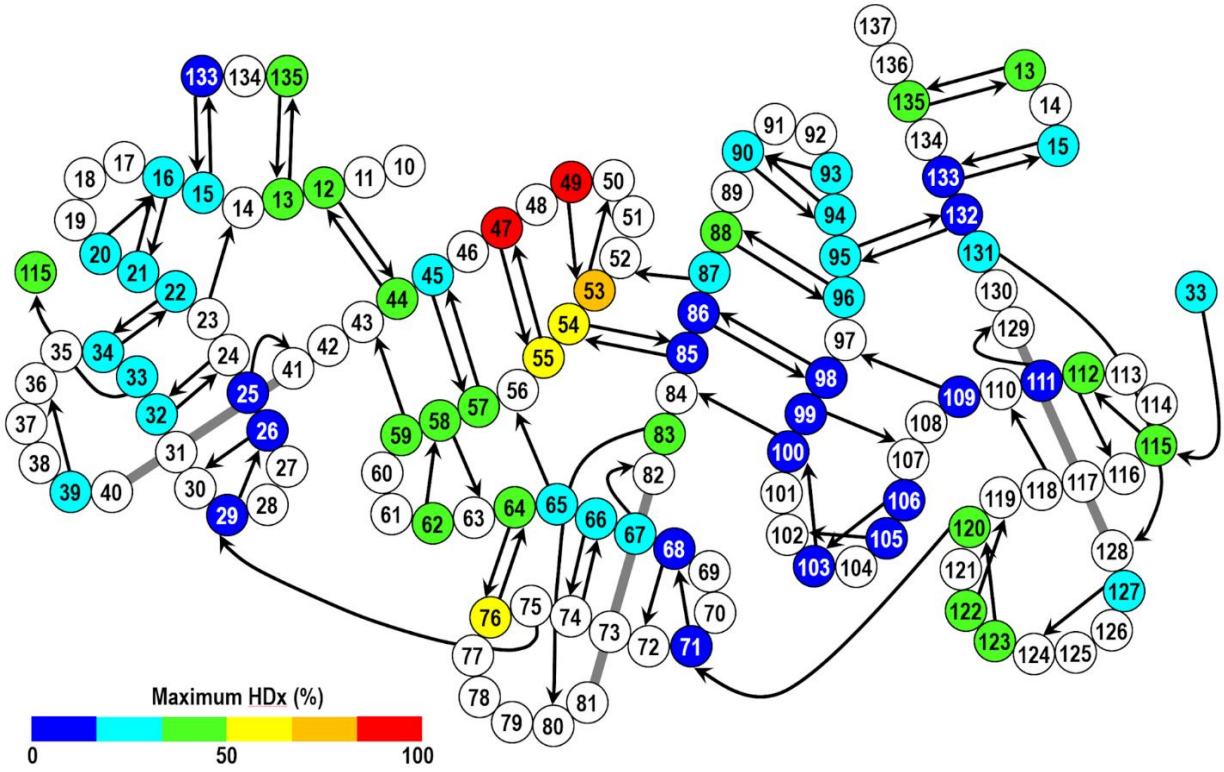

Figure 5. Secondary structure representation of FGF-1 with %HX values for buried amide positions. In the heat map, red indicates maximum HX while blue indicates minimum HX.

The effects of polyanions on the local backbone flexibility of FGF-1: Deuterium uptake changes for a peptide segment in the presence of a polyanion can be compared with unliganded FGF-1 to infer alterations in the local backbone flexibility of FGF-1 induced by ligation. In the presence of polyanions, there was either a decrease or no change in HX exchange at various time points. Representative deuterium uptake curves in Figure 6 show the effect of polyanions on the HX kinetics from different regions of FGF-1. For example, all four polyanions produced no change in hydrogen exchange in peptides 74-83 and 47-63. All of the polyanions induce a decrease in hydrogen exchange in the N –terminus region (peptide segment 8-15) and in peptide segments 98-110 as well as 107-110 of the C-terminus portion of FGF-1.

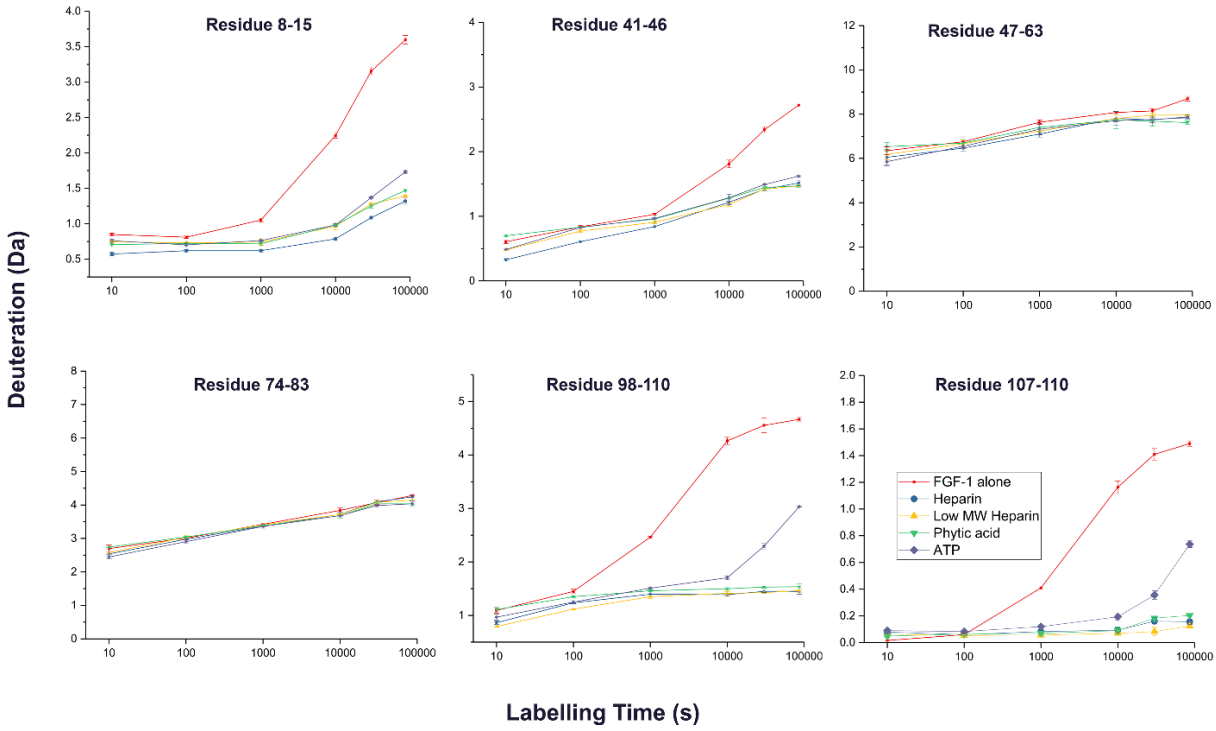

Figure 6. Examples of the effects of different polyanions on the deuterium uptake in six representative segments from different regions of FGF.

HX-MS analysis of FGF-1 with bound heparin: HX-MS analysis was performed at six labelling times ranging from 13s to 24 hr as shown in Figure 7B. Heparin at 0.2x by weight of FGF-1 was used since higher concentrations of heparin suppresses the ionization of FGF-1 peptides. Distinct changes in the rate of HX are seen in the presence of heparin. Shown in Figure 7A are two FGF-1 peptides in which the peptide covering residues from 74-84 did not show any changes in the presence of heparin while peptides spanning residues 98-111 show a significant lowering in the exchange rate. Polyanions upon binding to FGF-1 decreases the rate of exchange in the areas of contact and thus represent potential binding sites of that ligand. Exchange rate differences between bound and unbound states were quantified as described previously (24). The magnitude of protection (ΔHX) for various time points is shown in Figure 7B.

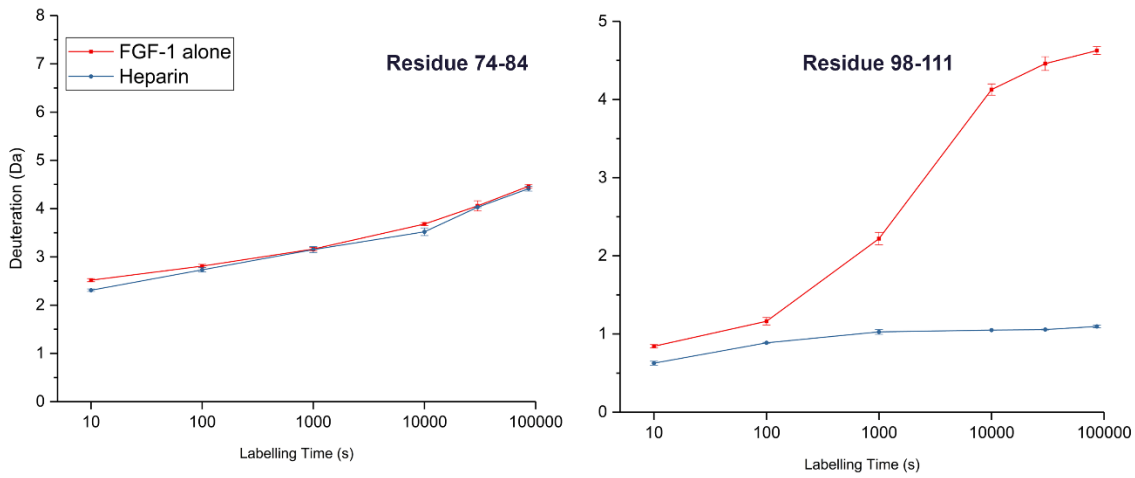

Figure 7A. Deuterium exchange kinetics of two representative FGF-1 peptides. Panel A shows peptide 51 (residues 74-84) where the rate of HX is not affected by heparin. Panel B shows peptide 81 (residues 98-111) where the rate of HX was slowed significantly by heparin.

The ΔHX values for heparin are then time averaged to create $\Delta\overline{HX}$ plots as shown in Figure 8A. The results are analyzed in all cases based on these $\Delta\overline{HX}$ plots unless otherwise specified. Heparin protection of FGF-1 peptides is shown in a $\Delta\overline{HX}$ plot (Figure 8A) and the results are mapped onto the crystal structure of FGF-1 (Figure 9A). Heparin binding to FGF-1 caused a substantial slowing of HX in the N-terminus of FGF in four overlapping peptides (3, 4, 5 and 7) that span residues 8-15. Strong protection is observed in four overlapping peptides (16, 17, 18 and 19) that span residues from 32-44. Heparin also caused strong protection in the C-terminus of FGF-1 in nine peptides (74, 76, 77, 80, 81, 83, 84, 85 and 86) that span residues 95-131. A heat map of buried amides of FGF-1 in the presence of heparin was calculated and mapped to the secondary structure of FGF-1 (Figure 10).

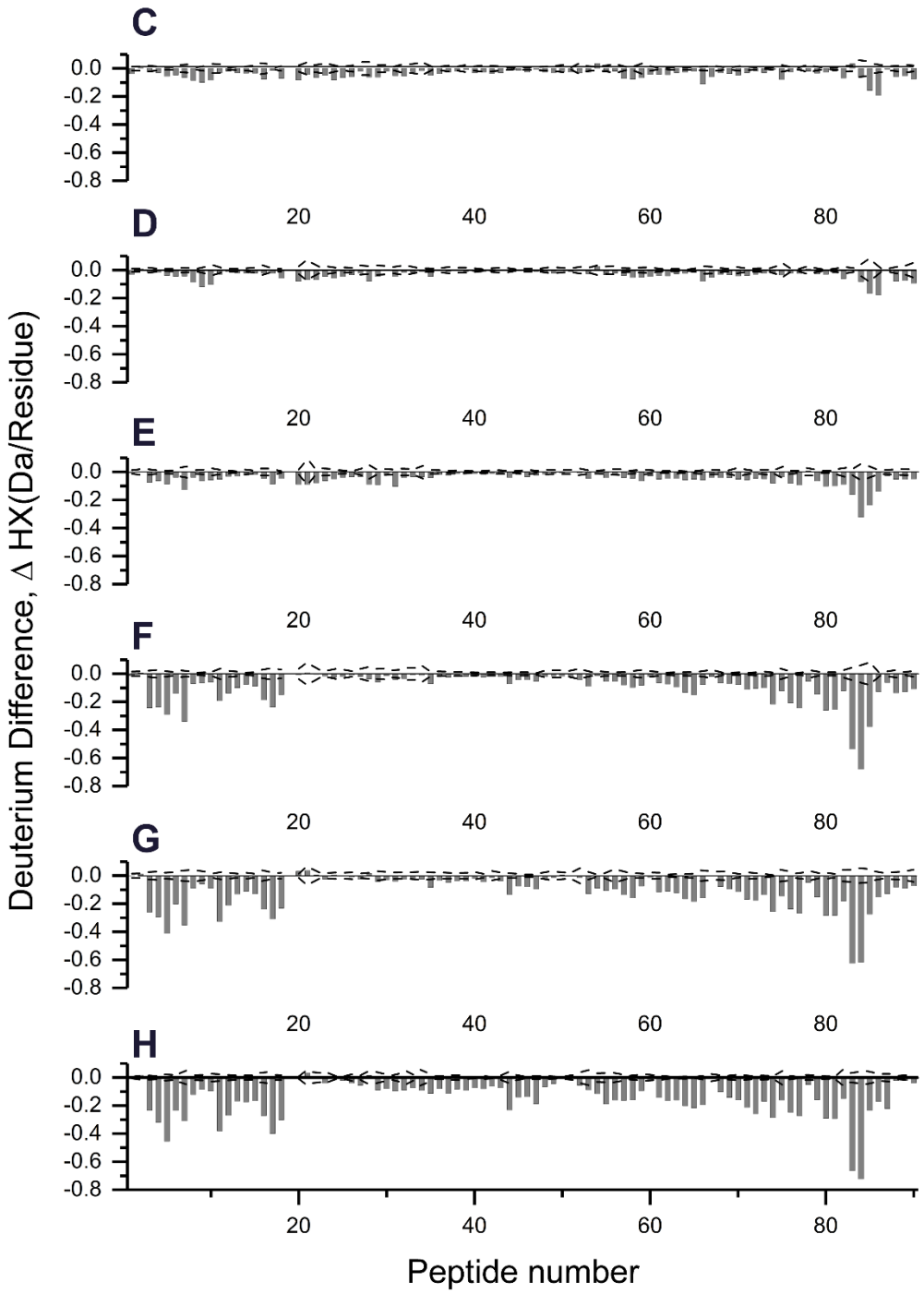

Figure 7B. HX-MS analysis of FGF-1 in the presence of heparin. Uptake at each HX time for FGF-1 labeled alone was subtracted from uptake when labelled in the presence of heparin, resulting in mass differences that are plotted at (C) 13 s, (D) 100 s, (E) 1,000 s, (F) 10,000 s, (G) 30,000 s and (H) 86,000 s (24 hr) of labeling. Error bars represent the standard deviation of triplicate measurements propagated through the difference.

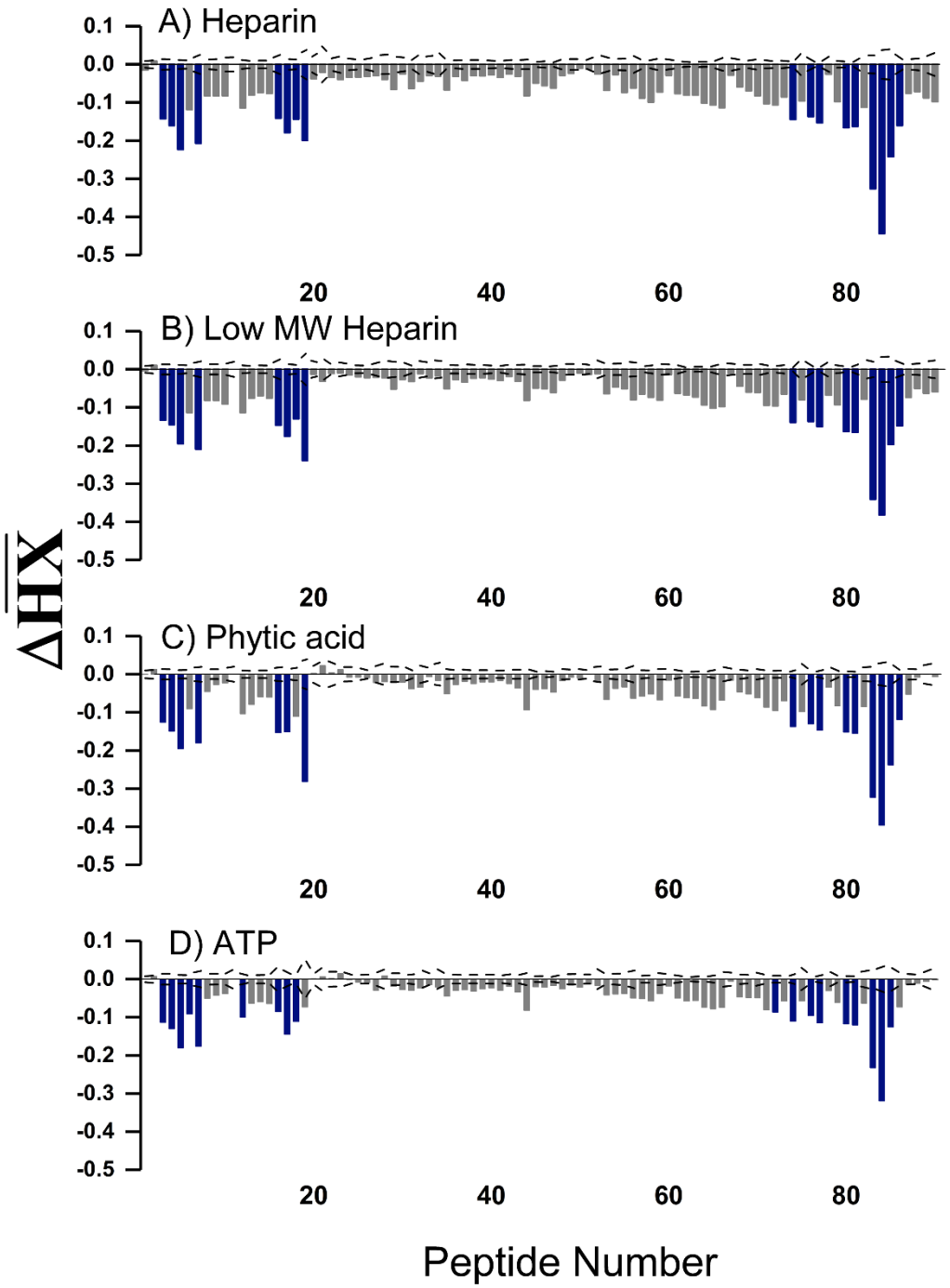

Figure 8. Relative protection of FGF-1 peptides by heparin, low MW heparin, phytic acid and ATP: HX-MS was performed with FGF-1 in the presence of (A) Heparin, (B) Low MW heparin, (C)Phytic acid and (D) ATP. The $\Delta\overline{HX}$ values for each FGF-1 peptide are shown and colored according to their *k*-means categorization: strong protection (deep blue) and intermediate protection/ insignificant (gray).

HX-MS analysis of FGF-1 with bound low MW heparin, phytic acid and ATP: Based on HX-MS analysis, low MW heparin produces strong protection in the same peptide segments seen with heparin (Figure 8B and 9B). The magnitude of protection in the strongly protected peptides, however, is slightly less than heparin except in the case of peptide 19 (residues 42-44) where low MW heparin manifests slightly higher protection. Phytic acid also causes a substantial decrease in deuterium uptake in FGF-1 as seen in a $\Delta\overline{HX}$ plot (Figure 8C). Phytic acid addition again produces strong protection in peptides similar to heparin and low MW heparin. The magnitude of protection seen in the strongly protected regions is similar to heparin and low MW heparin, although the amount of phytic acid used is 2x by weight of FGF-1. Upon binding, ATP induced strong protection in the N –terminus of FGF-1 in five overlapping peptides (3, 4, 5, 6 and 7) that span residues 8-22. Strong protection is also seen in four overlapping peptides (12, 16, 17 and 18) that span residues 23-46. ATP also causes strong protection in the C-terminus of FGF-1 in four overlapping peptides (72, 74, 76, and 77) that span residues 90-111 as well as five overlapping peptides (80, 81, 83, 84 and 85) that span residues 98-117 (Figure 8D and 9D). The magnitude of protection observed in the strongly protected peptides was less than that seen with heparin, low MW heparin and phytic acid. It should be noted that ATP is significantly less polyanionic than the other three agents. Heat maps of buried amides of FGF-1 in the presence of low MW heparin, phytic acid and ATP were calculated and mapped to the secondary structure of FGF-1 (Supplementary Figure 3, 4 and 5 respectively).

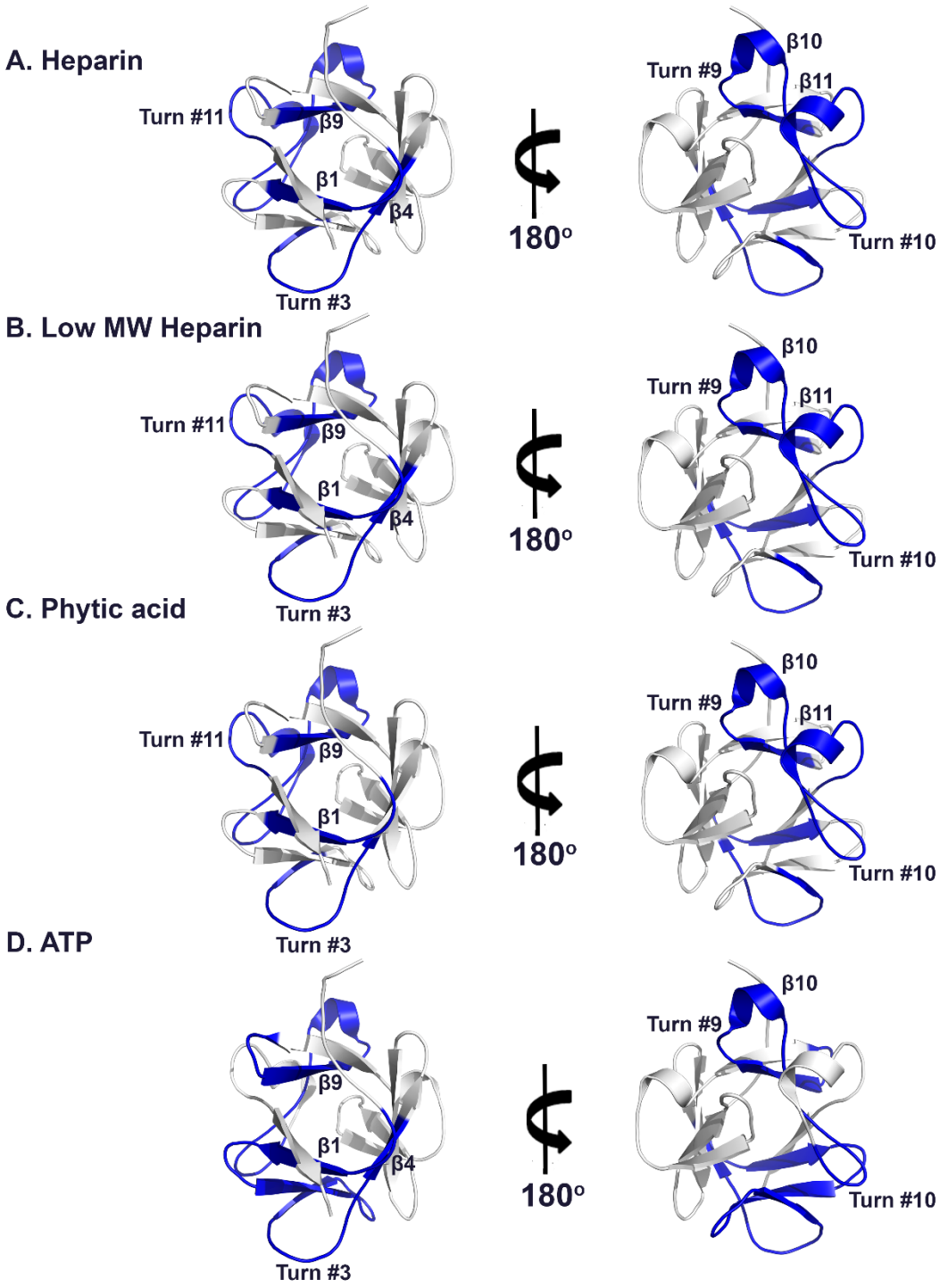

Figure 9. Visual presentation of heparin, low MW heparin, phytic acid and ATP contact regions on FGF-1. The binding sites are mapped on to the structure of FGF-1 for (A) Heparin, (B) Low MW heparin, and (C) Phytic acid and (D) ATP. The image is color coded as in Fig 8.

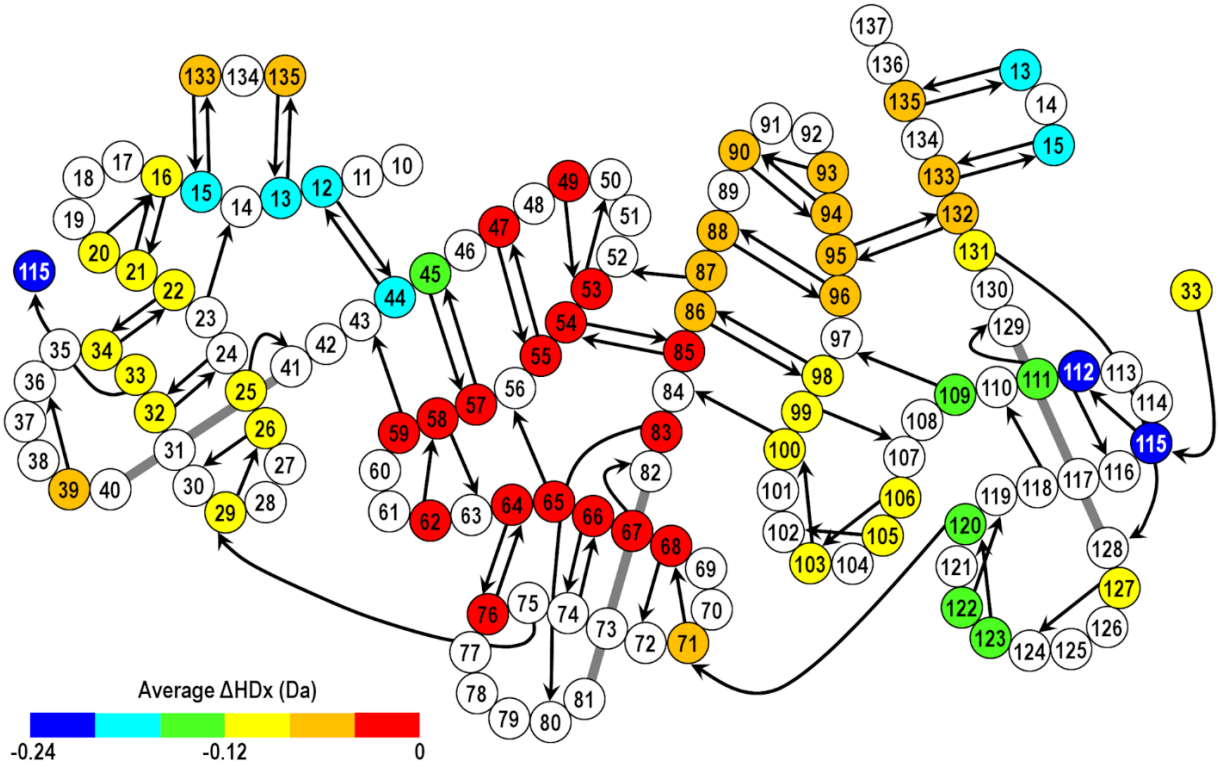

Figure 10. Heat map for FGF-1 upon addition of heparin. Red color in the heat map indicates no change in HX values upon binding of HS to FGF-1; blue color indicates an increase in HX protection.

Discussion:

At the peptide level, the HX determined flexibility of FGF-1 has shown that peptides that span strands 4 and 5 which form a hairpin-like structure along with turn 4 are rapidly exchanging with more than 60% of the theoretical exchangeable amides (Figure 4A). NMR studies have shown that the region which spans turn 4 has higher flexibility (17). Interleukin 1β which exhibits strong structural homology to FGF-1 has also been shown to have relatively higher flexibility in turn 4 (17). Additionally, we have also seen peptides that span strand 7 and turn 7 possess greater flexibility. NMR studies find that the glycine at position 75 (proximal end of strand 7) exhibits the most rapid motion of all residues in FGF-1 (17). We see that C-terminal strand 12 has higher

flexibility. This can be explained since other β-strands are involved in strand pairing (forming a hairpin -like structure) while the C-terminal strand 12 is a separate strand (not involved in strand pairing) making it more flexible. The heparin bound form did not substantially alter the flexibility of FGF-1 in strand 12 (see figure 8A; peptides 87, 88 and 89) i.e. the plasticity still exists in strand 12. This might be biologically relevant, since it includes residues Leu133 and Leu135 which define the regions of FGF-1 that are responsible for receptor binding. Other interaction sites that are critical for receptor binding include residues Tyr15, Ser17 (see figure 4A; peptides 8, 9 and 10); Arg35, Arg37 (see figure 4A; peptides 14 and 15); Glu87, Arg88, Leu89, Glu91, His93, Tyr94 and Asn95 (see figure 4A; peptides 58-62). All are observed to be primarily in intermediate flexibility regions. The flexibility of those regions does not appear to be altered substantially by heparin binding (see figure 8A). Many molecular recognition processes involve induced fitting in which dynamic properties play an important role. Heparin binds and dimerizes FGF-1 and presents the growth factor to the receptor to form a ternary complex. The fact that the amino acid residues of FGF-1 that are involved in receptor binding remain flexible in the presence of heparin may reflect the ability of FGF-1 to have a broad–specificity for FGFRs. For the rigid regions, we observed peptides that span strands 2 and 3 which are involved in a strand pair are exchanging slowly as well as turns 2 and 3. In addition, we found peptides that span strand 6 and turn 6 are more rigid. This region appears to be a part of a core folding nucleus. Strands 8, 9 and 10 in the C-terminus region are also seen to be rigid. This is confirmed by NMR in which it is observed that the strands in the C-terminal region are more rigid than other strands that form the β-barrel (17).

Upon analyzing HX-MS data at the residue level, residues with the lowest %HX values include a number of hydrophobic amino acids that contribute to the cooperative central hydrophobic core packing group, including Ile25, Phe85, Val109, Leu111 and Phe132 (11). The

14 residue region of positions 98-111 includes eight positions identified as being among the lowest %HX values (Figure 5**)**. This region comprises an extended structural loop in the third trefoil fold domain. Several of these positions have no direct structural equivalent in terms of the C_3 structural symmetry. In the crystal structure of FGF-1 bound to the FGFR-1 ectodomain (1EVT), this region of FGF-1 makes no contact with the receptor(29). In the crystal structure of FGF-1 with FGFR2 and heparin (PDB accession 1E0O) (3), this region makes contact with the heparin fragment (Lys105, Trp107). In the crystal structure of FGF-1, FGFR1c and HS (PDB accession 3OJV) this loop makes no contact with the receptor or HS (7). In the crystal structure of the FGF-1, FGFR2D2 and sucrose octasulphate (SOS) complex (PDB accession 3CU1), this portion of the molecule makes no contact with either receptor or SOS. Leu44 is related to Phe85 and Phe132 by the pseudo-threefold symmetry of the FGF-1 β-trefoil architecture. Unlike Phe85 and Phe132, however, Leu44 exhibits a distinctly larger %HX value. The crystal structure of FGF-1 identifies a cavity adjacent to Leu44 - large enough to accommodate the aromatic ring of a Phe mutation with no structural distortion (11). Thus, the increased %HX at position Leu44 is most consistent with a core-packing defect (e.g. a cavity) that permits structural flexibility. The HX data for FGF-1 exhibits as expected a general trend of low HX for residues located in β-strands, and higher HX for residues in turn regions.

From the crystal structures, the lowest average Cα B-factors are found in a generally contiguous region spanning residue positions 56-132 (i.e. approximately the C-terminal two-thirds of the protein). The majority of Cα positions exhibiting the lowest average B-factors in this C-terminal region are hydrophobic amino acids that contribute to the core packing group of the protein (including Ile56, Met67, Cys83, Phe85, Tyr97, Phe108, Val109 and Phe132). Residue positions exhibiting the lowest HX values include Phe85, Val109, Ile111, Phe132 and Leu133.

Residue positions in this group also identified as buried hydrophobic amino acids exhibit the lowest B-factor values in the X-ray structure. Residue positions 44 - 55 (i.e. β-strands 4 and 5) are distinctive in exhibiting the highest HX values in the protein overall. The core-packing defects in the region of position 44 (i.e. at the interface of the first trefoil fold with the rest of the protein) thus not only increase the general atomic motion, but also the apparent solvent penetration of the N-terminal region described by β-strands 1-5. In this regard, β-strands 4-5 appear extremely sensitive to solvent penetration. The HX data are therefore consistent with the X-ray structure data - including isotropic B-factors and packing defects (i.e. cavities) within the core of the structure. The HX data identify increased solvent penetration for the β-4/β-5 strand region in comparison to B-factors for this region, which appear consistent with the presence of internal cavities.

A remarkable fact seen with all four polyanions is that the relative intensities of the $\Delta\overline{HX}$ values among the individual peptides is in most cases highly similar. This suggests a high degree of specificity in the location of the polyanion binding sites using this method. FGF-1 is known to have high affinity for large negatively charged molecules like heparin, membrane bound HSPG as well as smaller polyanions (30, 31). Studies show that various polyanions in FGF-1 solutions dramatically increase its stability and potency (32). HSPGs also play a key role in the distribution of FGF-1 at the tissue level. Thus, polyanion binding appears to be playing a crucial role in the biological function as well as in the stability of FGF-1. A large number of crystallographic as well as NMR studies have revealed the amino acid positions associated with heparin binding in FGF-1. A specific cluster of basic amino acids with significant positive charge density in the N-terminus (first β-hairpin) and C-terminus (last two-thirds of the third trefoil domain) are seen to be responsible for heparin binding. The above structural data has been complimented by a variety of function studies involving chemical modification, point mutations, deletions, homologous

substitution mutations, and peptide-binding competition studies in combination with analytical ultracentrifugation, surface plasmon resonance and affinity chromatography (14, 33-36). In addition to sulfated heparin and similar molecules, it has also been found that phosphate and carboxyl containing compounds stabilize FGF-1 against thermal unfolding. The common feature in such compounds is the presence of one or more large negatively charged regions. As the number of sulfates, carboxylates and phosphates increase, the ability of such polyanions to stabilize FGF-1 also generally increases. In addition to electrostatic interactions, the trigonal pyramidal geometry of sulfates and phosphates makes it possible to form hydrogen bonds between charged groups (37). Here we tested four polyanions, two sulfate containing polymers including heparin and low MW heparin and two phosphate containing compounds, Phytic acid and ATP.

Using HX-MS, we were able to see strong protection in the C-terminal domain region as well as in the N-terminus regions which are rich in positively charged amino acids. At a residue level, heparin binding provides increased protection for amides within the first trefoil fold - especially positions 12, 13, 15, 44 and 45. Conversely, heparin binding does not alter the HX protection of residues within the second trefoil fold. In the third trefoil fold, heparin binding increases HX protection for residue positions 109-123, with the greatest decrease in HX rates observed for position 112 and 115. In the crystal structure of the ternary complex of FGF-1/FGFR2/heparin (PDB accession 1E0O) bound heparin interacts (via salt bridges, H-bonds or van der Waals interactions) with Asn18, Lys105, Tryp107, Lys112, Lys113, Arg119, Pro121, Arg122, Gln127, Lys128 (38). Thus, the increased HX protection upon heparin binding observed for residue positions 12, 13 and 15 in the first trefoil fold domain appear due to the interaction between heparin and adjacent Asn18. In this regard, local structural effects due to heparin binding seem to be communicated to adjacent position Leu44 (which also increases protection of Gln45). The

increased HX protection of residue positions 109-123 in the C-terminus trefoil fold domain is consistent with extensive heparin interactions with residues in this region. In this regard, this part of FGF-1 is rich in basic amino acids which provide a charge partner to heparin sulfonate groups. In this region, Lys112 exhibits one of the major increases in HX protection, potentially identifying Lys112 as one of the more significant salt bridge interactions between FGF-1 and heparin.

Similar regions of increased HX protection are observed for all polyanions. This involves primarily N-terminal residue positions 12, 13, 15, 44 and 45, and C-terminal positions 109, 111, 112, 115, 120, 122, and 123 (See supplementary Figure 3, 4 and 5). The magnitude of $\Delta\overline{HX}$ protection is, however, a function of the size/charge (charge density) of the polyanion. Thus, ATP exhibits the weakest overall $\Delta\overline{HX}$ protective effect, while heparin exhibits the greatest (Fig 8). Low MW heparin exerts essentially identical $\Delta\overline{HX}$ values as seen with heparin; the main distinction is a slight reduction of HX protection at residue positions 12, 13, 15, 112 and 115. Interestingly, the amount of heparin used was the lowest in terms of molar ratio with FGF-1 while ATP was the highest, yet the protection with heparin is more than ATP indicating the importance of a polyanion carrying more negative charges for strong affinity. It was also reported that heparin favors 2:1 and 3:1 FGF/heparin sulfate complexes as the protein concentration increased (39). Binding of the comparatively small ATP polyanion exerts $\Delta\overline{HX}$ effects that involve a characteristic distribution of N and C-terminus positions also associated with larger polyanion binding. This suggests a generalized induced-fit structural response associated with anion binding, which involves specific positions in the N- and C-termini trefoil-fold motifs. As discussed above, binding of anions at position Asn18 appears to communicate HX changes to adjacent positions 12, 13, 15, 44 and 45. Position 45 is associated with core-packing defects that may permit induced fit changes.

In all cases of polyanion binding the central trefoil fold appears devoid of any large $\Delta\overline{HX}$ effects; thus, the central trefoil fold region is not directly associated with anion-binding. This central region has been identified as a major part of the FGF-1 folding nucleus (15). A "folding/function" tradeoff has been proposed for the general organization of the FGF-1 primary structure (potentially a general theme in protein evolution) (15, 40), and the HX data supports this hypothesis, in which heparin strongly interacted with the functional C-terminus while no substantial interaction is seen in the core folding region of FGF-1 .

References

1. Beenken A, Mohammadi M. The FGF family: biology, pathophysiology and therapy. Nature reviews Drug discovery. 2009;8(3):235-53.

2. Johnson DE, Williams LT. Structural and functional diversity in the FGF receptor multigene family. Advances in cancer research. 1993;60:1-41.

3. Pellegrini L, Burke DF, von Delft F, Mulloy B, Blundell TL. Crystal structure of fibroblast growth factor receptor ectodomain bound to ligand and heparin. Nature. 2000;407(6807):1029-34.

4. Spivak-Kroizman T, Lemmon MA, Dikic I, Ladbury JE, Pinchasi D, Huang J, et al. Heparin-induced oligomerization of FGF molecules is responsible for FGF receptor dimerization, activation, and cell proliferation. Cell. 1994;79(6):1015-24.

5. Ornitz DM, Xu J, Colvin JS, McEwen DG, MacArthur CA, Coulier F, et al. Receptor specificity of the fibroblast growth factor family. The Journal of biological chemistry. 1996;271(25):15292-7.

6. Zhang X, Ibrahimi OA, Olsen SK, Umemori H, Mohammadi M, Ornitz DM. Receptor specificity of the fibroblast growth factor family. The complete mammalian FGF family. The Journal of biological chemistry. 2006;281(23):15694-700.

7. Beenken A, Eliseenkova AV, Ibrahimi OA, Olsen SK, Mohammadi M. Plasticity in interactions of fibroblast growth factor 1 (FGF1) N terminus with FGF receptors underlies promiscuity of FGF1. The Journal of biological chemistry. 2012;287(5):3067-78.

8. Murzin AG, Lesk AM, Chothia C. beta-Trefoil fold. Patterns of structure and sequence in the Kunitz inhibitors interleukins-1 beta and 1 alpha and fibroblast growth factors. Journal of molecular biology. 1992;223(2):531-43.

9. McLachlan AD. Three-fold structural pattern in the soybean trypsin inhibitor (Kunitz). Journal of molecular biology. 1979;133(4):557-63.

10. Blaber M, DiSalvo J, Thomas KA. X-ray crystal structure of human acidic fibroblast growth factor. Biochemistry. 1996;35(7):2086-94.

11. Brych SR, Blaber SI, Logan TM, Blaber M. Structure and stability effects of mutations designed to increase the primary sequence symmetry within the core region of a beta-trefoil. Protein science : a publication of the Protein Society. 2001;10(12):2587-99.

12. Bernett MJ, Somasundaram T, Blaber M. An atomic resolution structure for human fibroblast growth factor 1. Proteins. 2004;57(3):626-34.

13. DiGabriele AD, Lax I, Chen DI, Svahn CM, Jaye M, Schlessinger J, et al. Structure of a heparin-linked biologically active dimer of fibroblast growth factor. Nature. 1998;393(6687):812-7.

14. Brych SR, Dubey VK, Bienkiewicz E, Lee J, Logan TM, Blaber M. Symmetric primary and tertiary structure mutations within a symmetric superfold: a solution, not a constraint, to achieve a foldable polypeptide. Journal of molecular biology. 2004;344(3):769-80.

15. Longo L, Lee J, Blaber M. Experimental support for the foldability-function tradeoff hypothesis: segregation of the folding nucleus and functional regions in fibroblast growth factor-1. Protein science : a publication of the Protein Society. 2012;21(12):1911-20.

16. Canales-Mayordomo A, Fayos R, Angulo J, Ojeda R, Martin-Pastor M, Nieto PM, et al. Backbone dynamics of a biologically active human FGF-1 monomer, complexed to a hexasaccharide heparin-analogue, by 15N NMR relaxation methods. Journal of biomolecular NMR. 2006;35(4):225-39.

17. Chi Y, Kumar TK, Chiu IM, Yu C. 15N NMR relaxation studies of free and ligand-bound human acidic fibroblast growth factor. The Journal of biological chemistry. 2000;275(50):39444-50.

18. Majumdar R, Manikwar P, Hickey JM, Samra HS, Sathish HA, Bishop SM, et al. Effects of salts from the Hofmeister series on the conformational stability, aggregation propensity, and local flexibility of an IgG1 monoclonal antibody. Biochemistry. 2013;52(19):3376-89.

19. Manikwar P, Majumdar R, Hickey JM, Thakkar SV, Samra HS, Sathish HA, et al. Correlating excipient effects on conformational and storage stability of an IgG1 monoclonal antibody with local dynamics as measured by hydrogen/deuterium-exchange mass spectrometry. Journal of pharmaceutical sciences. 2013;102(7):2136-51.

20. Arora J, Joshi SB, Middaugh CR, Weis DD, Volkin DB. Correlating the Effects of Antimicrobial Preservatives on Conformational Stability, Aggregation Propensity, and Backbone Flexibility of an IgG1 mAb. Journal of pharmaceutical sciences. 2017;106(6):1508-18.

21. Bommana R, Chai Q, Schoneich C, Weiss WFt, Majumdar R. Understanding the increased aggregation propensity of a light exposed IgG1 mAb using hydrogen exchange mass spectrometry, biophysical characterization, and structural analysis. Journal of pharmaceutical sciences. 2018.

22. Bazzoli A, Vance DJ, Rudolph MJ, Rong Y, Angalakurthi SK, Toth RTt, et al. Using homology modeling to interrogate binding affinity in neutralization of ricin toxin by a family of single domain antibodies. Proteins. 2017.

23. Vance DJ, Tremblay JM, Rong Y, Angalakurthi SK, Volkin DB, Middaugh CR, et al. High-Resolution Epitope Positioning of a Large Collection of Neutralizing and Non-Neutralizing Single Domain Antibodies on Ricin Toxin's Enzymatic and Binding Subunits. Clinical and vaccine immunology : CVI. 2017.

24. Toth Rt, Angalakurthi SK, Van Slyke G, Vance DJ, Hickey JM, Joshi SB, et al. High-Definition Mapping of Four Spatially Distinct Neutralizing Epitope Clusters on RiVax, a Candidate Ricin Toxin Subunit Vaccine. Clinical and vaccine immunology : CVI. 2017.

25. Volkin DB, Tsai PK, Dabora JM, Gress JO, Burke CJ, Linhardt RJ, et al. Physical stabilization of acidic fibroblast growth factor by polyanions. Archives of biochemistry and biophysics. 1993;300(1):30-41.

26. Dabora JM, Sanyal G, Middaugh CR. Effect of polyanions on the refolding of human acidic fibroblast growth factor. The Journal of biological chemistry. 1991;266(35):23637-40.

27. Majumdar R, Manikwar P, Hickey JM, Arora J, Middaugh CR, Volkin DB, et al. Minimizing carry-over in an online pepsin digestion system used for the H/D exchange mass spectrometric analysis of an IgG1 monoclonal antibody. Journal of the American Society for Mass Spectrometry. 2012;23(12):2140-8.

28. Bai Y, Milne JS, Mayne L, Englander SW. Primary structure effects on peptide group hydrogen exchange. Proteins. 1993;17(1):75-86.

29. Plotnikov AN, Hubbard SR, Schlessinger J, Mohammadi M. Crystal structures of two FGF-FGFR complexes reveal the determinants of ligand-receptor specificity. Cell. 2000;101(4):413-24.

30. Gospodarowicz D, Cheng J, Lui GM, Baird A, Bohlent P. Isolation of brain fibroblast growth factor by heparin-Sepharose affinity chromatography: identity with pituitary fibroblast growth factor. Proceedings of the National Academy of Sciences of the United States of America. 1984;81(22):6963-7.

31. Lobb RR, Fett JW. Purification of two distinct growth factors from bovine neural tissue by heparin affinity chromatography. Biochemistry. 1984;23(26):6295-9.

32. Copeland RA, Ji H, Halfpenny AJ, Williams RW, Thompson KC, Herber WK, et al. The structure of human acidic fibroblast growth factor and its interaction with heparin. Archives of biochemistry and biophysics. 1991;289(1):53-61.

33. Harper JW, Lobb RR. Reductive methylation of lysine residues in acidic fibroblast growth factor: effect on mitogenic activity and heparin affinity. Biochemistry. 1988;27(2):671-8.

34. Springer BA, Pantoliano MW, Barbera FA, Gunyuzlu PL, Thompson LD, Herblin WF, et al. Identification and concerted function of two receptor binding surfaces on basic fibroblast growth factor required for mitogenesis. The Journal of biological chemistry. 1994;269(43):26879-84.

35. Seddon AP, Aviezer D, Li LY, Bohlen P, Yayon A. Engineering of fibroblast growth factor: alteration of receptor binding specificity. Biochemistry. 1995;34(3):731-6.

36. Patrie KM, Botelho MJ, Franklin K, Chiu IM. Site-directed mutagenesis and molecular modeling identify a crucial amino acid in specifying the heparin affinity of FGF-1. Biochemistry. 1999;38(29):9264-72.

37. Kanyo ZF, Christianson DW. Biological recognition of phosphate and sulfate. The Journal of biological chemistry. 1991;266(7):4264-8.

38. Pellegrini L, Burke DF, von Delft F, Mulloy B, Blundell TL. Crystal structure of fibroblast growth factor receptor ectodomain bound to ligand and heparin. Nature. 2000;407(6807):1029-34.

39. Minsky BB, Dubin PL, Kaltashov IA. Electrostatic Forces as Dominant Interactions Between Proteins and Polyanions: an ESI MS Study of Fibroblast Growth Factor Binding to Heparin Oligomers. Journal of the American Society for Mass Spectrometry. 2017;28(4):758-67.

40. Xia X, Longo LM, Sutherland MA, Blaber M. Evolution of a protein folding nucleus. Protein science : a publication of the Protein Society. 2016;25(7):1227-40.

Supplementary Figures

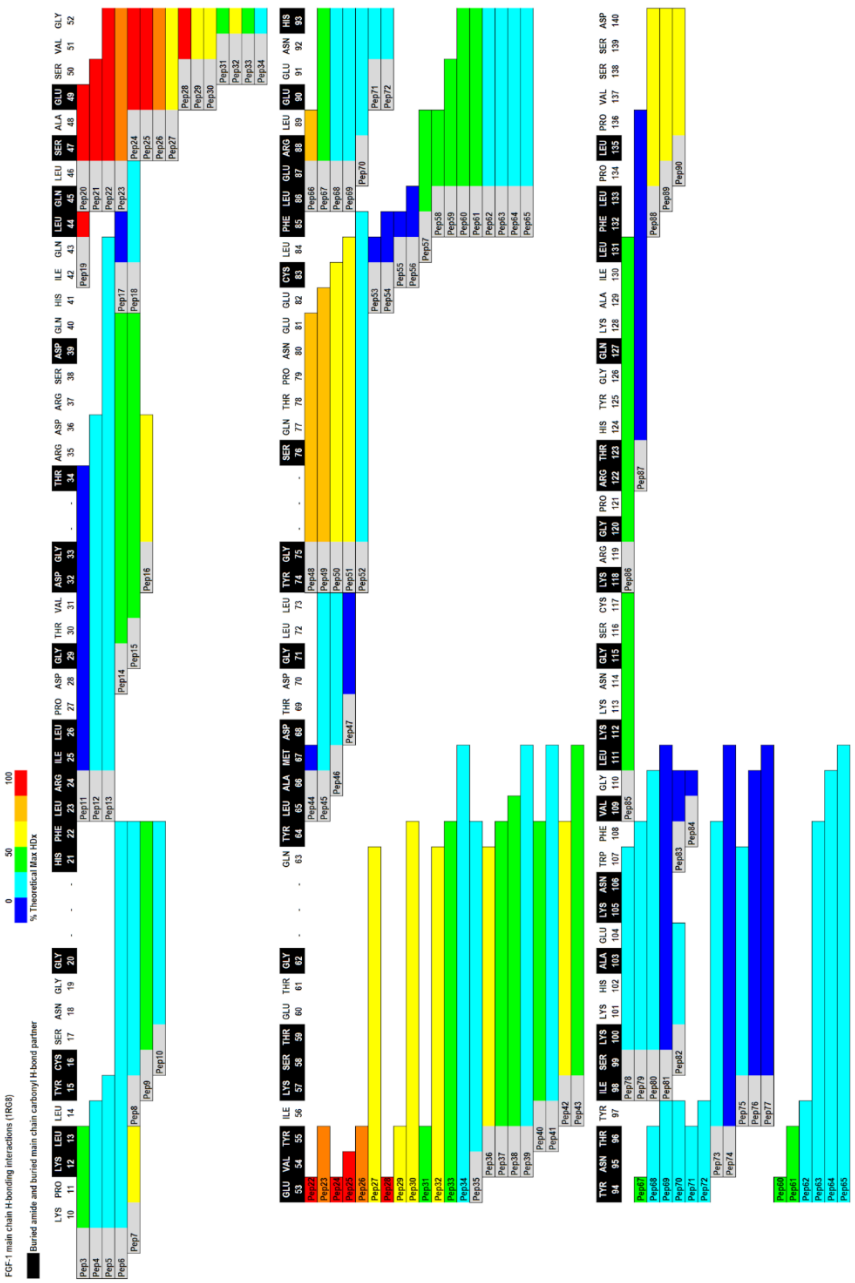

Supplementary Figure 1 shows the alignment of the 90 peptides with the FGF-1 sequence

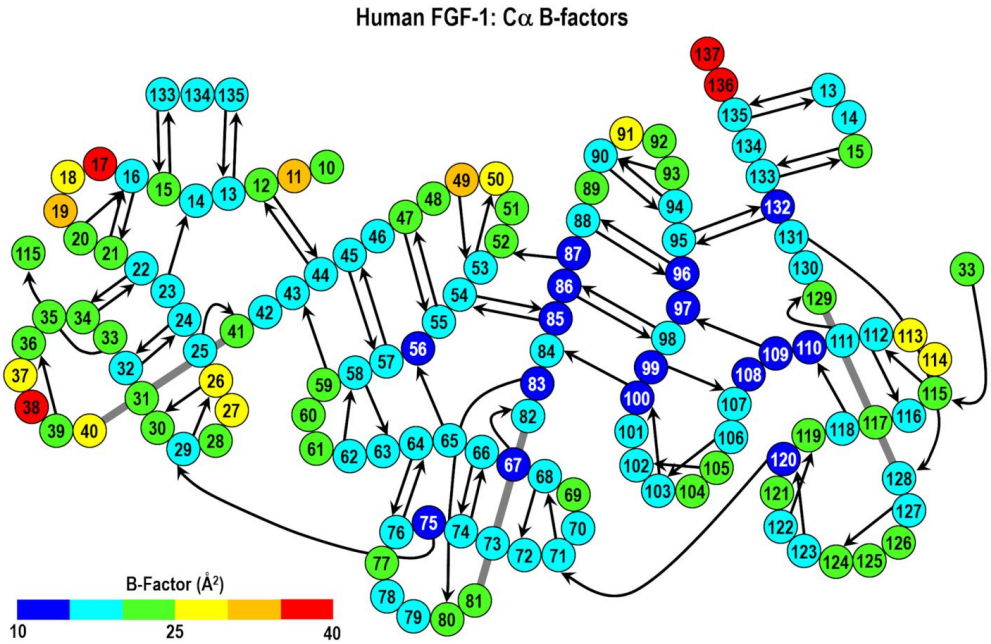

Supplementary Figure 2. Cα isotropic B-factors of FGF-1. Values are the average from six independent molecules crystallized in two different space groups. Residue positions 10-137 are consistently structured in all crystal forms (thus, residue positions 1-9 and 138-140 can be considered as having the equivalent of a red color in this figure).

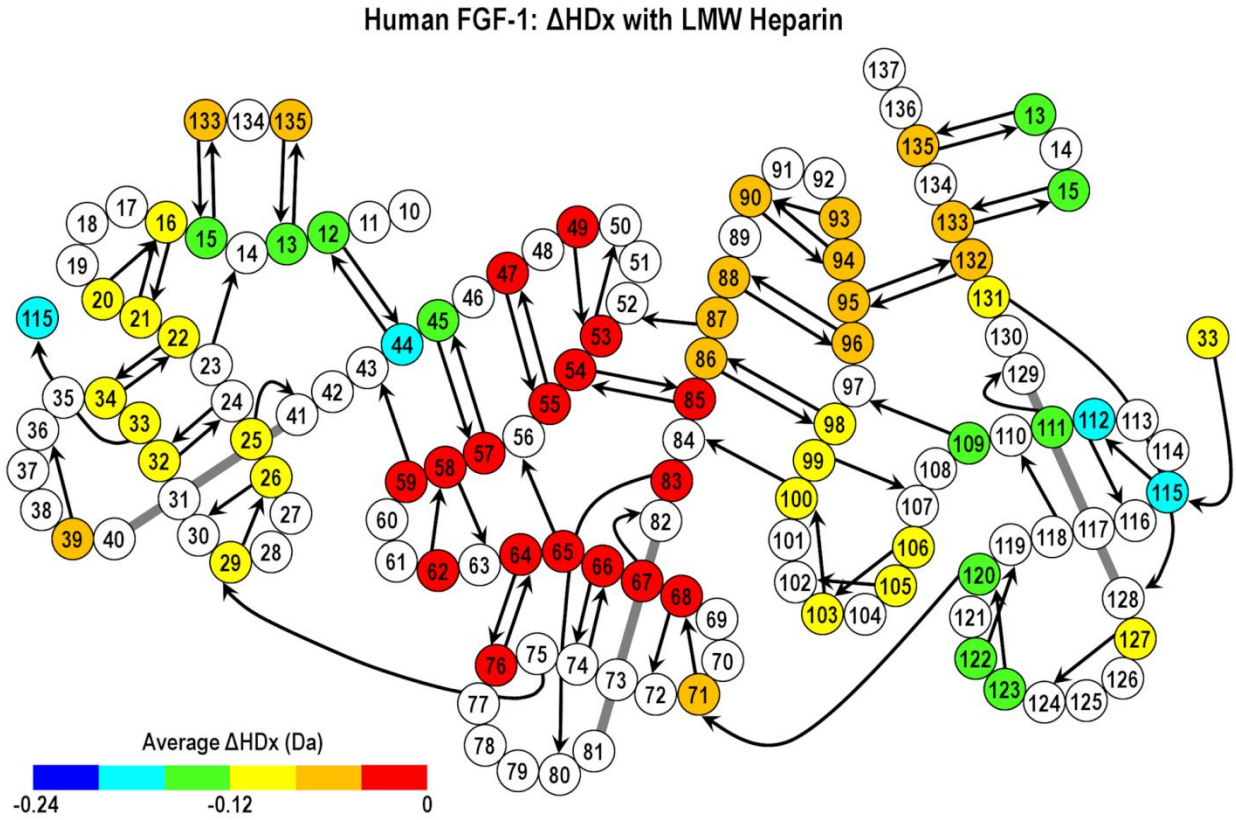

Supplementary Figure 3. ΔHX heat map for FGF-1 upon addition of low MW HS. Red color in the heat map indicates no change in HX values upon binding of low MW HS to FGF-1; blue color indicates an increase in HX protection. The heat map scale is the same as FGF-1+HS (Fig. 10).

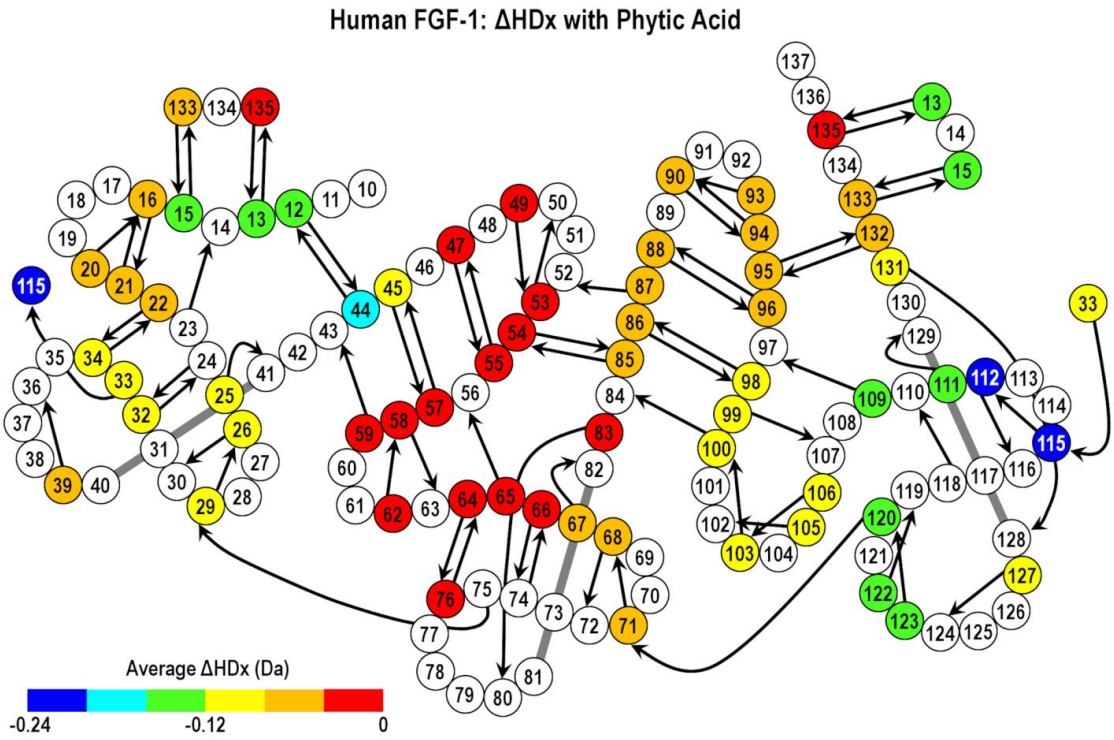

Supplementary Figure 4. ΔHX heat map for FGF-1 upon addition of phytic acid. Red color in the heat map indicates no change in HX values upon binding of HS to FGF-1; blue color indicates an increase in HX protection. The heat map scale is the same as FGF-1+HS (Fig. 10).

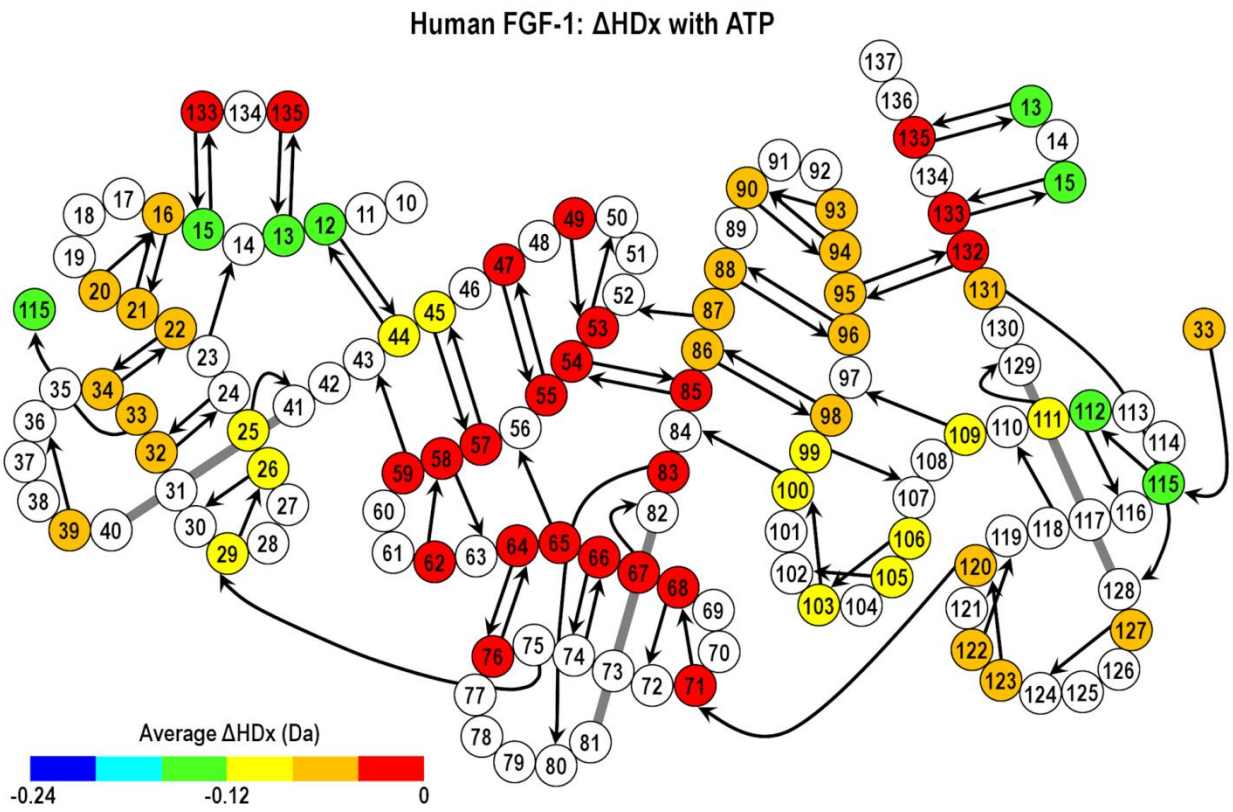

Supplementary Figure 5. ΔHX heat map for FGF-1 upon addition of ATP. Red color in the heat map indicates no change in HX values upon binding of ATP to FGF-1; blue color indicates an increase in HX protection. The heat map scale is the same as FGF-1+HS (Fig. 10).

Supplimentary Table 1. FGF-1 peptic peptides

Pep #	start	end	Pep #	start	end	Pep #	start	end
1	1	7	**36**	54	63	**71**	90	96
2	1	9	**37**	54	64	**72**	90	97
3	8	13	**38**	54	65	**73**	95	108
4	8	14	**39**	54	67	**74**	95	111
5	8	15	**40**	55	64	**75**	97	107
6	8	22	**41**	55	67	**76**	97	110
7	9	13	**42**	56	64	**77**	97	111
8	14	22	**43**	56	67	**78**	98	107
9	15	22	**44**	65	67	**79**	98	108
10	16	22	**45**	65	73	**80**	98	110
11	23	34	**46**	66	73	**81**	98	111
12	23	36	**47**	68	73	**82**	99	104
13	23	43	**48**	74	81	**83**	107	110
14	28	40	**49**	74	82	**84**	108	110
15	29	40	**50**	74	83	**85**	109	117
16	32	36	**51**	74	84	**86**	118	131
17	41	44	**52**	74	85	**87**	122	136
18	41	46	**53**	82	84	**88**	132	140
19	42	44	**54**	82	85	**89**	133	140
20	45	49	**55**	83	85	**90**	134	140
21	45	50	**56**	83	86			
22	45	53	**57**	84	89			
23	45	55	**58**	85	89			
24	47	53	**59**	85	91			
25	47	54	**60**	85	94			
26	47	55	**61**	85	96			
27	47	63	**62**	85	97			
28	49	53	**63**	85	108			
29	49	55	**64**	85	110			
30	49	64	**65**	85	111			
31	50	55	**66**	86	89			
32	50	63	**67**	86	94			
33	50	64	**68**	86	96			
34	50	67	**69**	86	97			
35	53	64	**70**	87	97			

CHAPTER 4. Conclusions and future directions

Conclusions

Ricin is a fast acting protein toxin that is classified as a potential agent of bioterrorism (1, 2). Currently, two leading subunit vaccine candidates centered on ricin toxin chain A (RTA) namely RiVax and RVEc are under development for ricin toxin. RiVax is a full length derivative of RTA with two point mutations, while, RVEc is a truncated version of RTA which is relatively more stable than RiVax. Phase 1 clinical trials have been performed for both vaccine candidates (3, 4). Both RiVax and RVEc are deemed to be safe in humans, however, neither of them were particularly effective in eliciting toxin neutralizing activity (TNA), which is a key measure of vaccine efficacy. Hence, there is a need to develop more potent vaccine candidates for ricin. To date, the rationale for designing subunit vaccine candidates for ricin has been focused on developing safer and stable derivatives of RTA. The results of RiVax and RVEc phase 1 clinical trials made it clear that in order to redesign a potent vaccine candidate based on RTA, an immunological rationale has to be elucidated and implemented. Immunity against ricin is antibody mediated. Understanding immune responses to RTA and ricin toxoid has been challenging as immunization elicited a complex mixture of antibodies (Abs) including toxin neutralizing, non-neutralizing and toxin-enhancing Abs (5, 6). It was also reported that neutralizing antibodies constitute only a minor portion of the total antibodies elicited against RTA (7). Therefore, having a comprehensive B-cell epitope map on the surface of ricin would aid in the development and evaluation of effective ricin vaccines. In fact, efforts to develop an effective ricin subunit vaccine are obstructed by lack of B cell epitope information on ricin's enzymatic (RTA) and binding (RTB) subunits which are important in eliciting protective immunity.

To this end, a great deal of work has been done to performed structural epitopes on RTA. *O'Hara's et al.* work has found that serum antibodies of RiVax-immunized mice and rabbits reacted with six

immune dominant liner regions on RTA(7). The work in that report was limited to linear epitopes, in which the majority of antibodies elicited (>85%) target conformation dependent epitopes. Hence, it is important to map conformational dependent epitopes on RTA. In a later report, conformational epitopes were located on RTA using competitive binding assays (8). It was also reported that toxin neutralizing antibodies are limited to four spatially distinct regions on the surface of RTA, which we refer to as epitope clusters I-IV.

This dissertation sought to construct a B cell epitope map on the surface of ricin toxin chain A, RTA. For safety reasons, we have worked on a safer version of RTA, namely RiVax. Structurally both RiVax and RTA are virtually identical to each other. Therefore, we used RiVax in this dissertation to identify structural epitopes. To facilitate this, we have purified this recombinant version of RTA (RiVax) using E.coli as an expression vector. Once RiVax was purified, we have characterized the protein for its structural integrity and conformational stability (see appendix) as our interest lies in identifying conformational epitopes. In all, we have purified six batches of RiVax, of which, lot 3 was used for epitope mapping studies. RiVax was extensively characterized using various bio-physical techniques including intrinsic tryptophan fluorescence, circular dichroism, differential scanning calorimetry, static light scattering and size exclusion chromatography. Bio-physical analysis confirmed that RiVax structure is in a conformationally folded state which is essential for identifying conformational/ discontinuous epitopes. The melting temperature (Tm) values obtained using various analytical techniques were in good agreement with that of previous RiVax characterization work conducted in our lab (9). RiVax was also tested for the presence of disulfide bond induced aggregates using SDS-PAGE. Intact mass revealed that there are no significant modifications associated with RiVax.

In chapter 2, RiVax was subjected to epitope mapping using hydrogen exchange mass spectrometry (HX-MS). Of the four epitope clusters (I-IV) that were identified on the surface of RTA, cluster III is recognized by only one mAb, namely IB2. Cluster III attains importance in that the toxin's active site is surrounded by it. In an effort to gain a greater understanding of this region, we used a large collection of single domain antibodies (V_HHs) that are directed towards cluster III. We previously reported the binding site of cluster III defining mAb, IB2 using HX-MS (10). IB2 engaged with secondary structural elements including helices C and G on the surface of RiVax. In this chapter, we described twenty one V_HHs directed against an immunodominant region, designated as epitope cluster III (Siva Angalakurthi et.al. *manuscript in preparation*). HX-MS analysis revealed that all twenty one antibodies that were studied have overlapping epitopes i.e. they share at least one common secondary structural element in their epitope. Based on their contact with secondary structural elements on the surface of RiVax, we found there are four subclusters (3.1-3.4) within cluster III region. Subcluster 3.1 includes helices C and G. Subcluster 3.2 encompasses helices B, C and G. subcluster 3.3 consists of helices B and G. Lastly, subcluster 3.4 includes strand h and helices C and E. Of the 21 antibodies, only two, namely V1D3 and V6D4 have shown TNA. V1D3 and V6D4 have shown strong affinity (sub nanomolar range) for the toxin. V1D3 fell into subcluster 3.1 i.e. it engaged helices C and G. While, V6D4 was categorized into subcluster 3.3 i.e. its epitope included helices B and G. Both neutralizing antibodies shared a common secondary structural element in the form of helix G in their epitopes. V1D3 which falls into subcluster 3.1 include a collection of 16 antibodies, whose HX-MS protection profiles look similar to V1D3. Interestingly, none of the antibodies except V1D3 has shown TNA. It should be mentioned V1D3 is one of the strong binders we found in this cluster. We speculate that V1D3's strong binding affinity (< 200pM) to the toxin could be one of the reasons for its TNA. Another

neutralizer, V6D4 falls into subcluster 3.4 which engages with helices B and G. Also, we observed V1D3 and V6D4 (the only neutralizing antibodies in this study) epitopes have helix G in common. We believe that binding affinity and epitope specificity (in this case, helix G) plays critical role in neutralizing activity. It is clear that further studies will be necessary to clarify the origins of neutralizing activity.

In chapter 3, we studied protein-small molecule interactions i.e. we sought to identify the binding sites of polyanions on the surface of FGF-1. FGF-1, which is unstable at room temperature is known to exhibit high conformational stability in the presence of heparin (polysulfate anion). Volkin and Middaugh's work have shown that FGF-1 exhibited increased thermal stability not only in the presence of heparin but also in the presence of a number of other sulfated and phosphorylated molecules (11). Based on those studies, we have selected and studied two sulfated molecules including heparin and low MW heparin and two phosphorylated molecules, namely phytic acid and adenosine triphosphate (ATP). All molecules have been shown to enhance the thermal stability of FGF-1 and the trend followed as: Heparin > low MW heparin > Phytic acid > ATP. We have used HX-MS to identify the binding sites of these polyanions on the surface of FGF-1. Based on HX-MS results, all four polyanions were shown to have similar protection profiles i.e. they bind to similar regions on FGF-1. Analysis revealed that the dense negatively charged polyanions interacted primarily with a positively charged patch in the C-terminus as well as with the positively charged amino acids in the N-terminus.

Future directions:

As a part of long standing efforts to generate a complete antigenic map of ricin toxin and to better define the epitopes associated with neutralizing activity, we have extensively studied cluster III using a collection of single domain antibodies. Although it is difficult to predict what makes an antibody neutralizing based on our studies in chapter 2, we speculate that helix G contact on RTA plays a crucial role in neutralizing activity. The fact that a number of antibodies (in subcluster 3.1) having similar epitopes to V1D3 (neutralizing antibody), yet none of them show any toxin neutralizing activity indicates that a deeper understanding of these antigen-antibody interactions at the single residue level is required. Some of the non–neutralizing antibodies have shown stronger binding affinity values than neutralizing antibodies. This further substantiate the need to identify those critical residue contacts. In addition, the manner by which these antibodies bind to the toxin i.e. the angle of contact, could also provide some insight into toxin neutralizing activity. To this end, studies have been initiated to solve crystal structures of toxin-antibody complexes. It is not the first time we see antibodies having similar/ overlapping epitopes yet showing different toxin neutralizing activity. Our collaborators have already showed how a single residue contact can effect the binding affinity and toxin neutralizing activity (12). Once the co-crystals are solved, it would be interesting to verify/ validate to what extent helix G plays a crucial role in neutralizing activity by engineering the CDR region of antibodies that interacts with helix G as well as by performing point mutations in helix G. It would also be interesting to see how these antibodies might interact with helix G in the context of ricin holotoxin (i.e. in the presence of both A and B subunits).

As a part of generating a complete antigenic map of ricin toxin, extensive epitope mapping studies have been conducted on the RTA subunit. As a reminder, four epitope clusters have been identified on RTA. Cluster I and II have been studied previously. In this study, we reported results for cluster III. The cluster IV region is located in the more disordered C –terminus region of RTA. Although, studies in mice have shown that this cluster elicits mainly non-neutralizers, it is worth pursuing studies to gain a better understanding of the cluster IV region using V_HHs. The fact that V_HHs are often able to see cryptic regions could help in defining neutralizing and non-neutralizing epitopes in cluster IV since it is this region that binds to the RTB subunit by a disulfide bond. This region is crucial due to the fact that ricin in the endoplasmic reticulum (ER) undergoes disulfide reduction to get A chain free from its B chain counterpart which allows RTA to enter into the cytosol and eventually target ribosomes.

Thus far, much attention has been directed to the RTA subunit since it contains the active site. In the future, we will start mapping epitopes on the RTB subunit. It would be interesting to see if there are any toxin neutralizing antibodies that are directed towards this subunit. In this case, solving crystal structures of toxin neutralizing antibody- RTB complexes would not only help in identifying the CDR region that is interacting with RTB but also in rationale engineering of CDR regions for developing therapeutics against ricin. Since RTB helps the toxin entry into the host cell, developing therapeutics that target RTB subunit might block ricin from entering into cell.

Once a complete antigenic map is constructed on both subunits using a collection of murine mAbs and V_HHs, the next step would be validating B cell epitopes identified on RTA in humans. As said previously, two leading subunit vaccine candidates based on RTA (RiVax and RVEc) have undergone phase 1 clinical trials. Identifying B cell epitopes on RTA recognized by human

vaccines by evaluating clinical sera would have important ramifications for the advanced development of an RTA based subunit vaccine.

REFERENCES:

1. Griffiths GD. Understanding ricin from a defensive viewpoint. Toxins. 2011;3(11):1373-92.
2. Reisler RB, Smith LA. The need for continued development of ricin countermeasures. Advances in preventive medicine. 2012;2012:149737.
3. Vitetta ES, Smallshaw JE, Schindler J. Pilot phase IB clinical trial of an alhydrogel-adsorbed recombinant ricin vaccine. Clinical and vaccine immunology : CVI. 2012;19(10):1697-9.
4. Pittman PR, Reisler RB, Lindsey CY, Guerena F, Rivard R, Clizbe DP, et al. Safety and immunogenicity of ricin vaccine, RVEc, in a Phase 1 clinical trial. Vaccine. 2015;33(51):7299-306.
5. Colombatti M, Pezzini A, Colombatti A. Monoclonal antibodies against ricin: effects on toxin function. Hybridoma. 1986;5(1):9-19.
6. Maddaloni M, Cooke C, Wilkinson R, Stout AV, Eng L, Pincus SH. Immunological characteristics associated with the protective efficacy of antibodies to ricin. Journal of immunology (Baltimore, Md : 1950). 2004;172(10):6221-8.
7. O'Hara JM, Neal LM, McCarthy EA, Kasten-Jolly JA, Brey RN, 3rd, Mantis NJ. Folding domains within the ricin toxin A subunit as targets of protective antibodies. Vaccine. 2010;28(43):7035-46.
8. O'Hara JM, Kasten-Jolly JC, Reynolds CE, Mantis NJ. Localization of non-linear neutralizing B cell epitopes on ricin toxin's enzymatic subunit (RTA). Immunology letters. 2014;158(1-2):7-13.
9. Peek LJ, Brey RN, Middaugh CR. A rapid, three-step process for the preformulation of a recombinant ricin toxin A-chain vaccine. Journal of pharmaceutical sciences. 2007;96(1):44-60.
10. Toth Rt, Angalakurthi SK, Van Slyke G, Vance DJ, Hickey JM, Joshi SB, et al. High-Definition Mapping of Four Spatially Distinct Neutralizing Epitope Clusters on RiVax, a Candidate Ricin Toxin Subunit Vaccine. Clinical and vaccine immunology : CVI. 2017.
11. Volkin DB, Tsai PK, Dabora JM, Gress JO, Burke CJ, Linhardt RJ, et al. Physical stabilization of acidic fibroblast growth factor by polyanions. Archives of biochemistry and biophysics. 1993;300(1):30-41.
12. Rudolph MJ, Vance DJ, Cheung J, Franklin MC, Burshteyn F, Cassidy MS, et al. Crystal structures of ricin toxin's enzymatic subunit (RTA) in complex with neutralizing and non-neutralizing single-chain antibodies. Journal of molecular biology. 2014;426(17):3057-68.

Appendix A. Purification and biophysical characterization of RiVax

For an epitope mapping study, an antigen and its cognate antibody is required. In this case, the protein antigen was a recombinant ricin toxin chain A, RiVax. The monoclonal antibodies that are specific to ricin are produced in mice by hybridoma cell technology in which mice are immunized by ricin toxoid/ RTA/RTB or a mixture of subunits. Along with murine monoclonal antibodies, we have also worked with single domain antibodies. These are produced by immunizing alpacas with ricin toxoid and non-toxic mixtures of RTA and RTB. One of the main goals in this dissertation is identifying discontinuous (conformational) epitopes on the surface of RiVax. Hence, it is necessary to characterize the structure of RiVax for its structural integrity as discontinuous epitopes cannot be identified if the protein antigen structure is unfolded. We have purified 6 batches of RiVax, of which, lot 3 was used to conduct epitope mapping studies. RiVax was characterized in the same buffer conditions (25mM sodium phosphate, 150 mM NaCl, pH 7.4) as those used in epitope mapping studies.

Materials and methods:

Sample preparation: 25 mM phosphate buffer containing 150mM NaCl at pH 7.4 was prepared using an appropriate amounts of monobasic and dibasic sodium phosphate (Fisher). RiVax stock was stored in histidine buffer with 10%w/v sucrose at -80^{o}C. Prior to experiments, RiVax was thawed and then dialyzed into 25mM phosphate buffer (pH: 7.4) at 4^{o}C using Slide-A-Lyzer Dialysis cassettes of 10 kDa MWCO (Pierce, Rockford, IL). The concentration of RiVax was determined by UV spectroscopy employing an extinction coefficient of 0.83 mL/mg.cm.

Intrinsic tryptophan fluorescence: Intrinsic fluorescence spectra was measured using a Photon Technology International (PTI) spectrofluorometer equipped with a turreted 4-position peltier

temperature controller. RiVax has a single tryptophan and an excitation wavelength of 295 nm (>95% Trp emission) was used. Emission spectra were collected from 305-405 nm by a photomultiplier with a slit width of 3nm and an integration time of 1s. Fluorescence spectra were collected at 2.5^{o}C intervals with an equilibration time of 3 min at each temperature from 10-87.5^{o}C. A 1- cm path length quartz cuvette was used for all experiments. Data analysis was performed using Felix™ (Photon Technology International) software. Prior to data analysis, a buffer spectrum was subtracted from each protein sample spectrum. Using a mean spectral center of mass method (msm) executed in Middaugh Suite, the emission wavelength maximum was determined. This method although increases the signal to noise ratio for more accurate determination of λ_{max} values, it shifts the apparent peak by 5-10 nm from their actual value. Tm values were determined using a first derivative method on origin 7.0 software.

The PTI fluorometer has a second detector that is located at 180^{o} to the fluorescence detector which is used to study the aggregation behavior of RiVax. Light scattering data was obtained simultaneously during the florescence experiments. The scattering intensities were collected at 295 nm (the fluorometer excitation wavelength) with slit width of 0.5-nm slit width as a function of temperature ranging from 10^{o}C- 87.5^{o}C.

Circular Dichroism: Far-UV CD spectroscopy was conducted using a Chirascan-plus circular dichroism spectrometer (Applied Photophysics Ltd) furnished with a peltier temperature controller and a 4 position cuvette holder. The CD spectra were collected from 195 – 260 nm using a 0.1 cm path length cuvette. Thermal melt experiments were performed from 10-90^{o}C at 2.5^{o}C interval and a heating rate of 10^{o}C/min. The CD signal at 208nm was monitored to follow the changes in secondary structure as a function of temperature. Prior to data analysis, buffer subtraction was

performed and an average of triplicate sample measurements were employed. Thermal melting temperature (T_m) values were obtained by a first derivative method using Origin software.

Differential scanning calorimetry: Differential scanning calorimetry (DSC) was performed using a Microcal VP-DSC capillary cell microcalorimeter (Microcal, Northampton, MA). Thermograms were collected over a temperature range of 10-90C with a scan rate of 1^{o}C /min. A concentration of 1.5 mg/ml of RiVax was used and measurements were made in triplicate. Prior to analysis, a buffer thermogram was subtracted from each protein measurement and the data were normalized to molar heat capacity. Data were processed using Microcal DSC software in origin 7.0 (Origin Lab, Northampton, MA). The data were fit using a mathematical model in origin 7.0. The onset temperature (T_{onset}) was taken as the temperature at which the heat capacity exceeded 500 cal mol^{-1} $^{o}C^{-1}$.

SDS-Gel studies: SDS-PAGE was conducted on RiVax samples under both reducing and non-reducing conditions. Samples were prepared by mixing protein with 4X NuPAGE-LDS sample buffer (Life technologies, Grand Island, NY) to a final concentration of 1X. For reduced samples, 50Mm dithiothreitol (DTT) was added. Samples were then heated for 5 min at 95^{o}C. Twenty µg of RiVax protein was analyzed by SDS-PAGE using 1X MES running buffer and a 4-12% Bis-Tris gradient gel. Gels were stained using coomassie blue R250 to visualize protein bands and ultrapure water was used for destaining.

Size exclusion chromatography (SEC): A Shimadzu Prominence UFLC HPLC system equipped with a photodiode array detector was used. To remove insoluble aggregates, RiVax samples were centrifuged at 13000rpm for 5 min. SEC was performed by injecting 20 µg of RiVax onto a 7.8 cm X 30 cm TSK-GEL BioAssist $G3SW_{XL}$ column (TOSOH Biosciences, King of Prussia, PA). The mobile phase was 20 mM sodium phosphate buffer (pH 7.4) and a flow rate of 0.7 ml/min

was maintained with a 30 min run time. To ensure the column and HPLC system integrity, a gel filtration standard (Bio-Rad, Hercules, CA) was run before and after the RiVax runs. Data analysis was conducted using LC-solution software (Shimadzu). The chromatograms were analyzed by integrating the peak area of monomer, dimer/trimer and higher order aggregates at 280nm.The relative area of the monomeric peak to the total peak area was used to calculate the monomer percentage in the sample.

Protein purification: The gene encoding RiVax with an N-terminal his tag which can be cleaved by tobacco etch virus (TEV) protease was subcloned into a ligation independent vector. Plasmid DNA was transformed into chemically competent BL21-RARE *E.coli* cells via heat shock (~42^{o}C). Using an LB/agar plate, positive colonies containing gene of interest were identified. Cells were grown in a 4L flask (containing 2L of culture media) at 37^{o}C with shaking at ~250rpm until an optical density of 0.5 was obtained. Cells were then induced by isopropyl β-D-1-thiogalactopyranoside (IPTG). A concentration of 0.2 mM IPTG was used. Before inducing with IPTG, the cells were pre-cooled to 15^{o}C. Cells were expressed overnight (~16hr) at 15^{o}C with shaking at ~250 rpm. Cells were harvested in a centrifuge (Beckman coulter 25R) at 4^{o}C for 10 min at 4000rpm. After centrifugation, the supernatant media was drained and cell pellets were recovered and resuspended thoroughly with 50mM Tris (pH 8). Cells were then stored at -80^{o}C for a few days and later thawed at room temperature in a water bath. Using a sonicator (Fisher scientific sonic dismembranator model 500), cells were lysed. During sonication, the cells were kept at 4^{o}C by placing in an ice bath to minimize protein denaturation. The lysed cells were then centrifuged and the supernatant was collected and filtered through 0.2 µm filter. The supernatant, which contains the protein of interest, RiVax, is then injected using an AKTA prime system onto a His Trap (5ml) Ni^{+2} affinity column (GE health care, Piscataway, NJ). The His tag protein which

binds to the Ni^{+2} column is eluted using a 50mM imidazole solution. The purified 6X his-tag RiVax was then subjected to TEV protease for his-tag cleavage. TEV protease and RiVax were mixed at a ratio of 1:20 respectively and dialyzed (cleaved his-tag dialyzed out) overnight in 50mM Tris buffer (pH 8). The protein solution, which contains RiVax and his tag TEV protease, was later purified using a Ni^{+2} column by gravity flow. RiVax was collected into a 96 well plate. Using a Nanodrop spectrometer the wells corresponding to RiVax were identified and pooled. RiVax was then dialyzed into 10mM histidine buffer, 150mM NaCl containing 10% w/v sucrose. Protein samples were then diluted to 1mg/ml and aliquots of 1ml were stored at -80^{o}C for long term storage.

Intact mass: RiVax's intact mass was analyzed on a model 6530 quadrupole time of flight (QTOF) mass spectrometer. Protein sample was injected into a liquid chromatography (LC) system, bound to a C8 column trap, desalted and then subjected to electron spray ionization and finally into the TOF analyzer for mass determination. RiVax's intact mass was determined by deconvoluting the protein mass spectrometry (MS) spectra using MassHunter quantitative analysis software.

Result and Discussion:

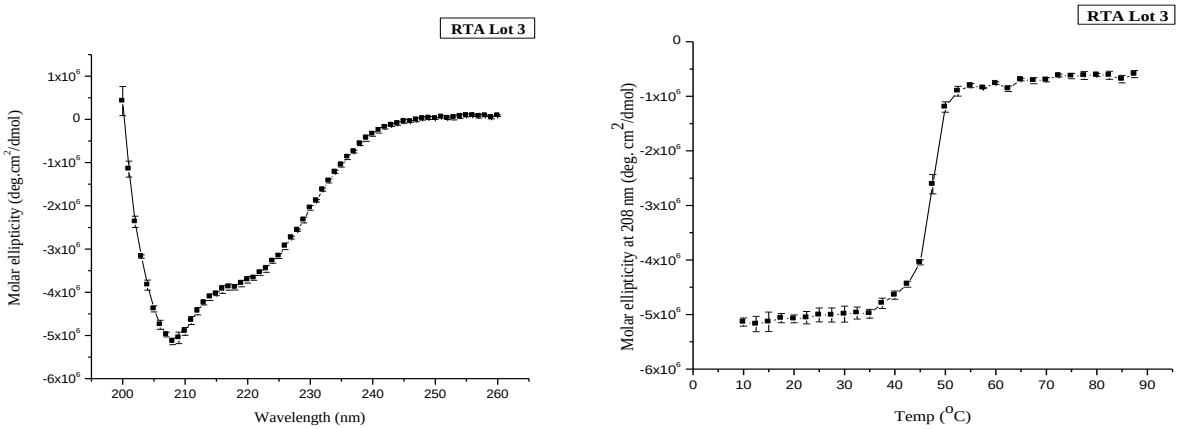

Figure 1: Left panel indicates the circular dichroism spectra of RiVax at 10ºC. Right panel indicates the thermal melting curve of RiVax obtained by following the molar elliptically at 208 nm as a function of temperature.

The secondary structure content of RiVax was characterized by Far-UV CD. A concentration of 0.2mg/ml of RiVax was used for the experiment. The left panel (Figure 1) represents the CD spectrum collected at 10ºC. At 10ºC, two minima were observed at 208 and 222 nm suggesting that the secondary structure content of RiVax is primarily of α-helical. This is consistent with the crystal structure of RiVax (PDB: 3SRP) where it is reported that nearly 40% of the protein is α-helices. Since the minimum at 208 nm is intense than the one at 222nm, we monitored the 208nm minimum to evaluate the loss of secondary structure. As observed from Figure 1 (right panel), RiVax tends to lose its secondary structure since the molar ellipticity increased as a function of temperature. Upon analyzing the CD thermal melt curves of RiVax, a T_m value of ~47.5ºC was

determined. The T_m value determined here (sodium phosphate buffer, pH 7.4) is similar to Peek and co-workers results (T_m ~ 44-52, citrate phosphate buffer, pH 7.0) that was previously published from our lab (1).

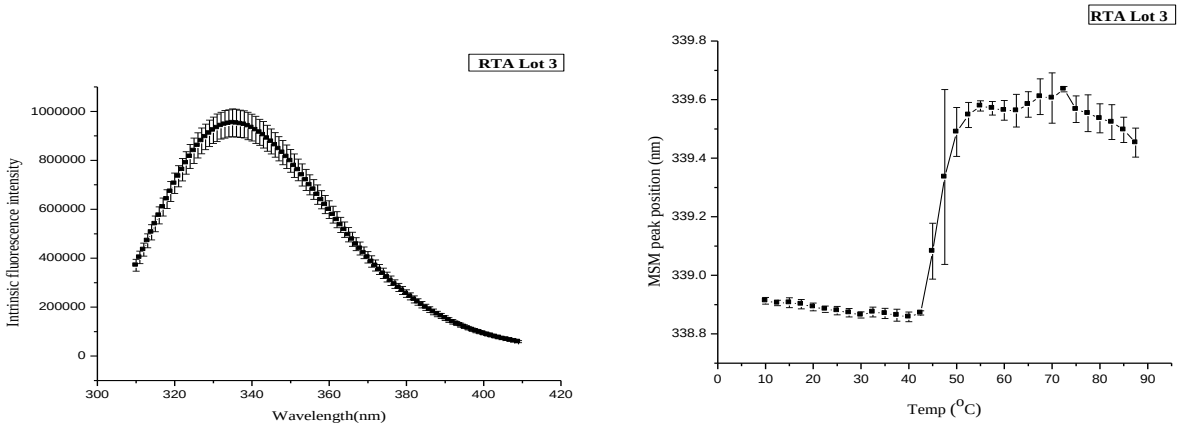

Figure 2: Fluorescence emission spectra of RiVax at 10ºC (left panel). Thermal melt curve of RiVax obtained by following changes in the wavelength emission maximum as a function of temperature (right panel).

RiVax (267 amino acid residues) has one tryptophan at position 211 in its primary sequence. Tryptophan is sensitive to the polarity of its environment. The excitation wavelength of 295 nm produces almost exclusively Trp emission. The fluorescence spectrum of RiVax at 10ºC showed an emission maxima (λ_{max}) at 330 nm (Figure 2, left panel), indicating that the lone tryptophan residue is located in a relatively hydrophobic environment. The effect of temperature on the MSM fluorescence peak position of RiVax was shown in Figure 2 (right panel). With increased temperature, λ_{max} red shifted indicating the Trp residue to be in a relatively more polar environment, implying structural alterations in RiVax's tertiary structure upon heating. Upon analyzing the fluorescence thermal melt curve, a thermal transition T_m value of ~ 46ºC was found.

RiVax's aggregation behavior was studied by monitoring the light scattering at 295 nm (i.e. the excitation wavelength used for fluorescence) simultaneously during intrinsic fluorescence spectroscopy. Light scattering from RiVax was monitored as a function of temperature ranging from 10-87.5^{o}C. Light scattering started to increase around 35^{o}C presumably due to aggregation of RiVax. The scattering intensity started to drop after 45^{o}C, a result due to precipitation of the protein (Figure 3).

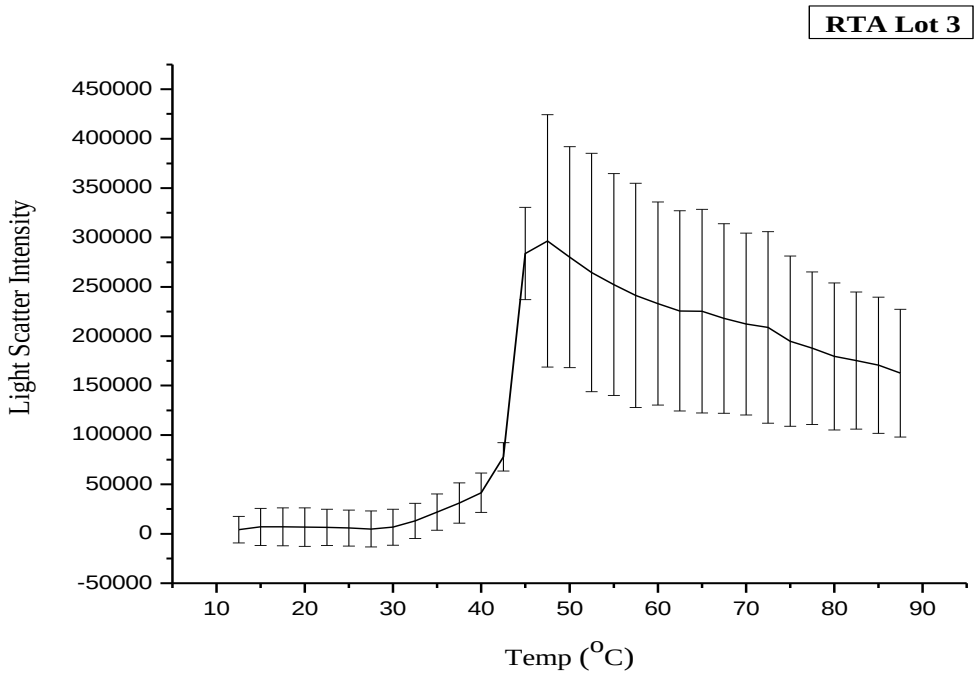

Figure 3: Aggregation propensity analysis of RiVax as analyzed by static light scattering as a function of temperature.

RiVax purity and size were assessed by SDS-PAGE. RiVax is unfolded by the SDS and was run under both reduced and non-reduced conditions. RiVax manifests the expected single band under reducing conditions where the apparent MW of the band (~ 28kDa) corresponds to that of RiVax

(theoretical MW: 29.9 kDa). Under non-reducing conditions, two protein bands were observed (~ 28kDa and ~ 51kDa) corresponding to RiVax's monomer and dimer respectively. RiVax has a cysteine on the surface and the small amount of dimer formation in the non-reduced condition is attributed to intermolecular disulfide bond formation. This was supported by the disappearance of the dimer band under reducing conditions.

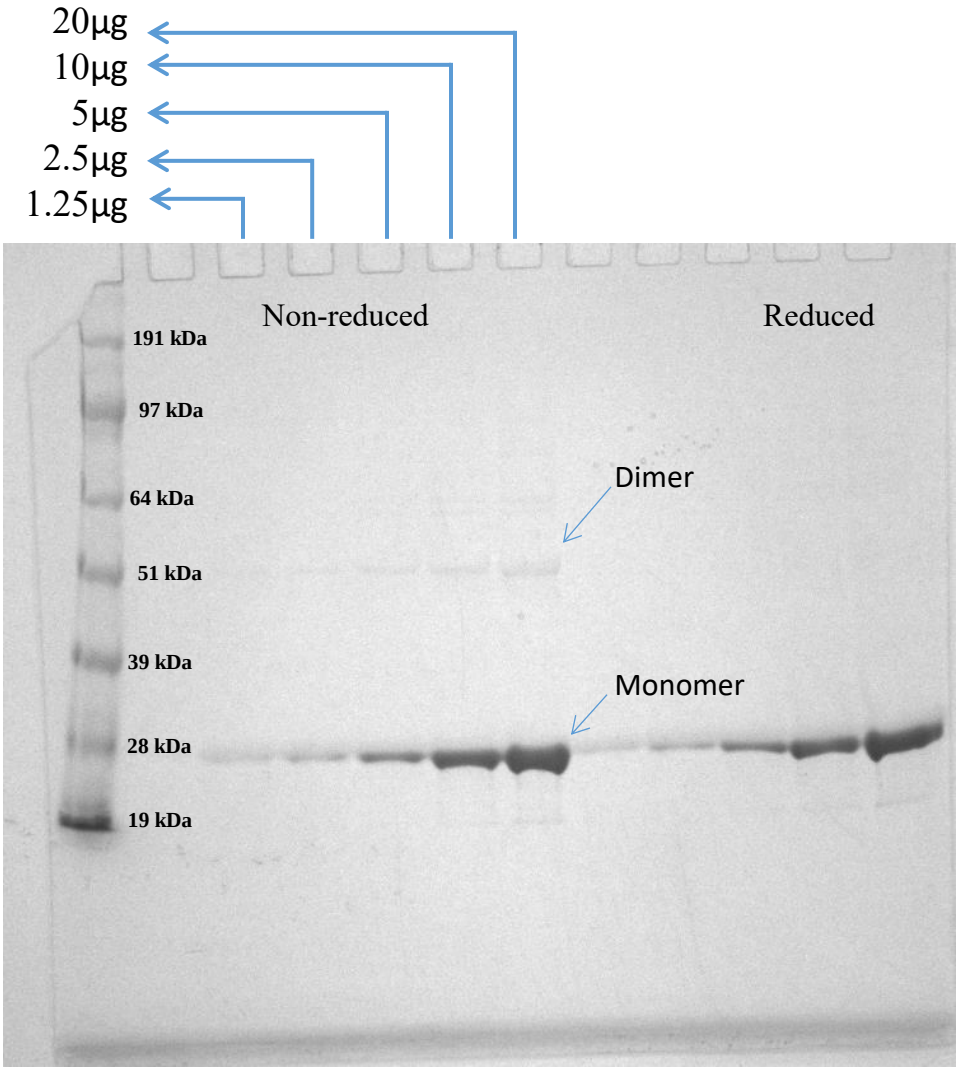

Figure 4: SDS-PAGE gel of RiVax in nonreduced and reduced state. Lane 1 indicate markers.

Samples	T_{onset}	T_m
RiVax Lot 3	39.8 ± 1.1 °C	46.3 ± 0.3 °C

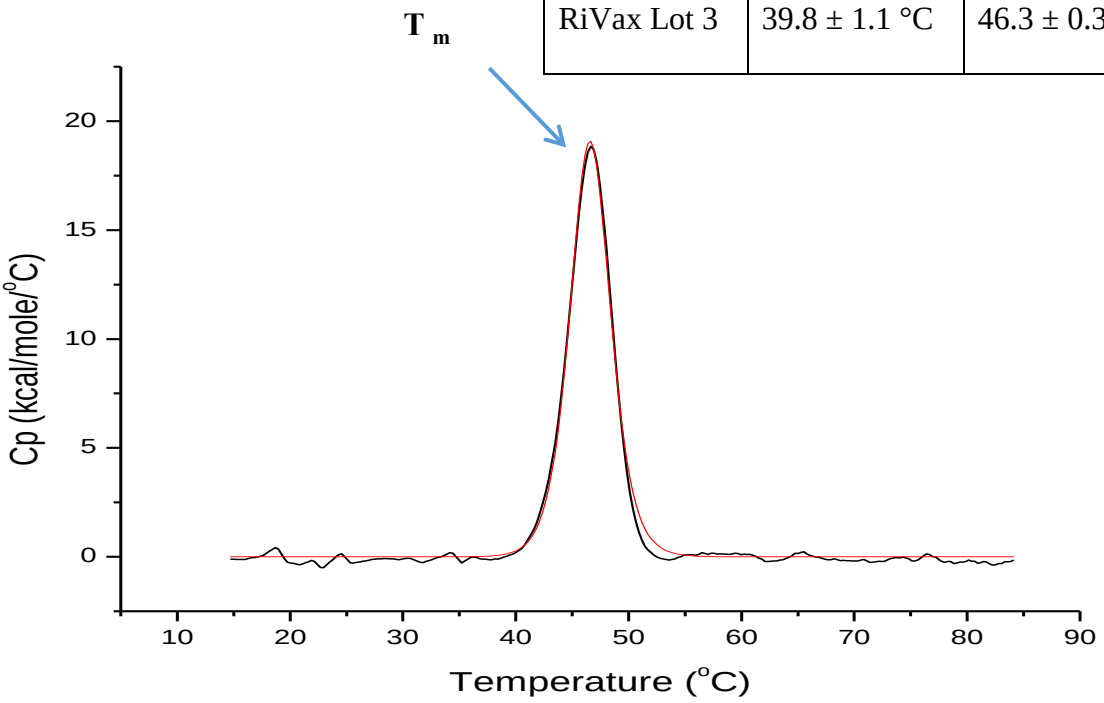

Figure 5: Representative DSC thermogram of RiVax. Conformational stability of RiVax was monitored as a function of temperature by DSC.

The overall conformational stability of the RiVax was followed by DSC. A concentration of 1.5 mg/ml of RiVax was used for the experiment. As shown in Figure 5, one major endothermic peak was observed at approximately 46°C with an onset temperature (T_{onset}) at nearly 40°C. It should be mentioned that the conformational stability of RiVax (20mM citrate phosphate, pH 7.0) was determined by DSC previously from our lab where RiVax has shown a broad endothermic peak at approximately 43°C and is subsequently fitted to 2 transitions (T_{m1} ~ 42°C and T_{m2} ~48°C) with the best mathematical model (2).

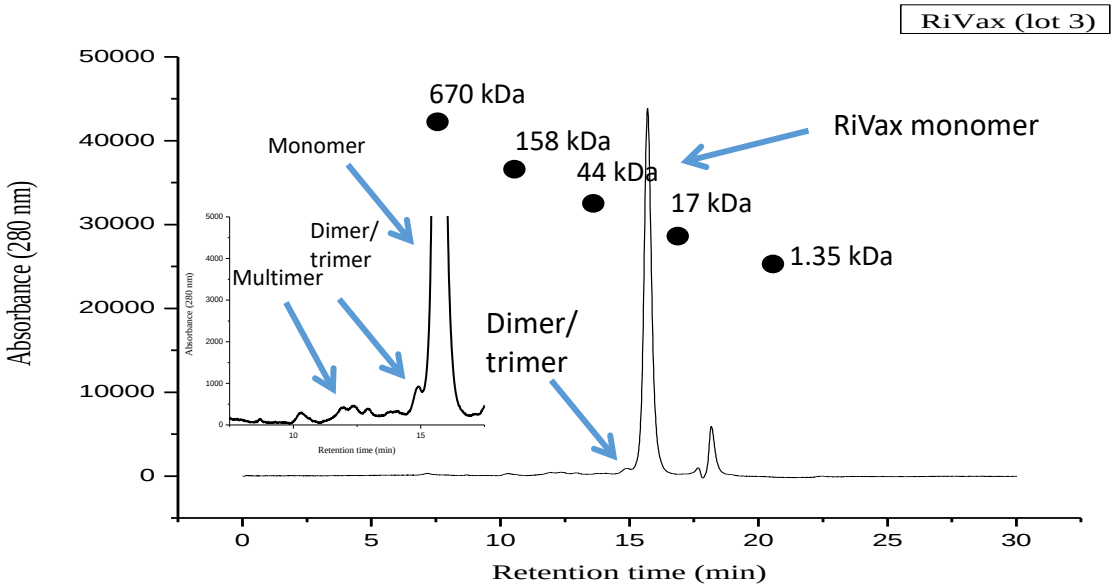

Figure 6: Size analysis of RiVax. The size and distribution of monomer and aggregate species in RiVax as evaluated by SEC. The molecular weight (MW) values of gel filtration standard proteins are shown in the SE chromatogram.

RiVax was also analyzed for the presence of monomer and aggregate species by SEC. Analysis of the SEC chromatogram (Figure 6) showed that RiVax eluted primarily as a monomer (~94%). A small amounts of dimer/timer and higher aggregate species were also observed. It is essential to characterize RiVax samples for the presence of aggregate species since having significant aggregates can lead to misinterpretation of results during epitope mapping studies.

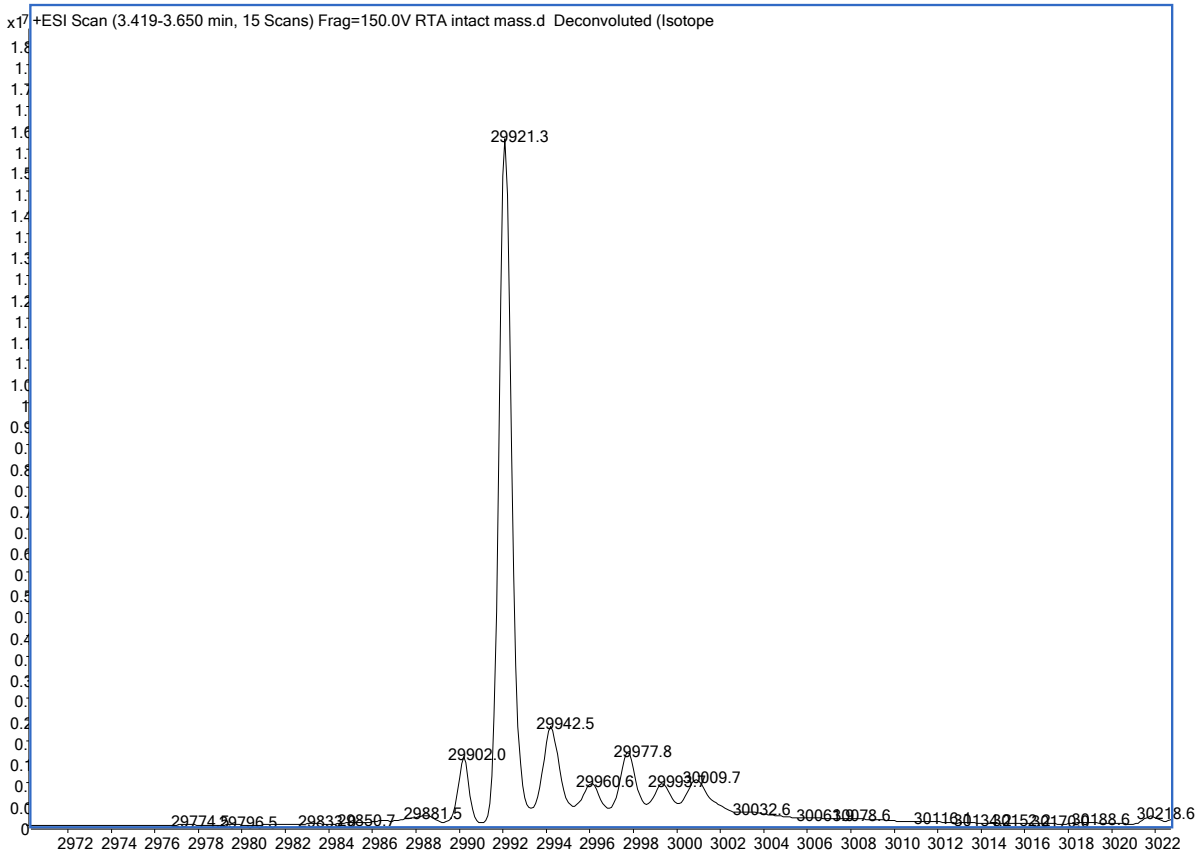

Figure 7: Primary structure analysis of RiVax. Intact mass spectrum of nonreduced RiVax. Theoretical intact mass of RiVax is 29920.66 (nonreduced).

Intact mass was analyzed to elucidate the molecular composition of RiVax. As shown in Figure 7, a single species was observed in the deconvoluted spectrum of RiVax. The observed mass of RiVax matches with that of theoretical mass (29920.66 Da) implying that the species is an unmodified RiVax monomer. Other minor species observed are presumably salt adducts of RiVax.

In conclusion, RiVax was characterized for its structural integrity and conformational stability. RiVax's conformational stability was evaluated as a function of temperature and found to be consistent with that of previous work performed by Peek et.al (1). RiVax was shown to exist in a folded state as revealed by various biophysical techniques including spectroscopy, DSC and light scattering which is critical for identifying discontinuous/ conformational epitopes on the surface of RiVax. The other aspects including aggregation and chemical modifications of RiVax were also tested. It is essential to ensure that RiVax is not in its aggregated form since the aggregation hotspot/ interface could obstruct/slower deuterium uptake and could lead to misinterpretation of HX-MS analysis. Using Size exclusion and SDS-PAGE we did not observe any significant aggregates in RiVax. Intact mass results ensured that there aren't any significant post translational modifications on the surface of RiVax. It is possible that any significant post translational modification on RiVax could hamper antibody binding, if the antibody targets a region close to any modifications.

REFERENCES:

1. Peek LJ, Brey RN, Middaugh CR. A rapid, three-step process for the preformulation of a recombinant ricin toxin A-chain vaccine. Journal of pharmaceutical sciences. 2007;96(1):44-60.

2. Thomas JC, O'Hara JM, Hu L, Gao FP, Joshi SB, Volkin DB, et al. Effect of single-point mutations on the stability and immunogenicity of a recombinant ricin A chain subunit vaccine antigen. Human vaccines & immunotherapeutics. 2013;9(4):744-52.